
Politecnico di Torino

# POLITECNICO DI TORINO

**Master's Degree in Biomedical Engineering**
**A.Y 2020-2021**
**Graduation session December 2021**

# Three-dimensional model to predict cell-mediated nanoparticles drug delivery for Glioblastoma treatment

**Supervisors**

**Prof. Gianluca Ciardelli**

**Prof. Clara Mattu**

**Prof. Gabriele Candiani**

**Candidate**

**Andrea Bezze**

# Summary

Glioblastoma (GBM) is the most frequent and most malignant brain tumour, with a dismal five-year survival rate lower than 5%. treatment is complex due to the presence of the Blood Brain Barrier (BBB), the high genomic variability, and the heterogeneity of the tumour microenvironment (TME). Moreover, the presence of a cancer stem cell (CSCs) niche drives the development of treatment resistance. Identifying appropriate therapeutic agents and delivery mechanisms to grant effective targeting with reduced side effects is key in improving GBM management. Unfortunately, drug screening mainly relies on ethically debated animal models or on *in vitro* models, which do not fully replicate the TME and other relevant phenomena such as angiogenesis or immune response.

To fill this gap, this study aims to develop a more reliable three-dimensional GBM model to investigate the transport and efficacy of nanoparticles (NPs)-based drug delivery systems. To achieve this, multicellular tumour spheroids (MTSs) modelling GBM histological heterogeneity were prepared. Different ratios of primary tumour cells (U87), microglia (HMC-3) and CSCs (GBM8) were used to prepare the MTSs and test the antitumor effect of a proteasome inhibitor, Bortezomib (BTZ), at different concentrations. BTZ is an extremely potent drug against GBM and GBM-CSC, as our *in vitro* results confirmed, but cannot be delivered to the brain due to its inability to cross the BBB. Hence, polymeric nanocarriers for BTZ encapsulation were developed and characterized to enhance drug accumulation at the target site. BTZ was successfully encapsulated in NPs with high efficiency (11±2%), achieving a sustained release over 5-7 days. The efficacy of BTZ-NPs against GBM MTSs was compared with that of free BTZ, showing a slightly delayed response, compatible with the slower drug release rate from the NPs. To further extend NPs uptake by tumour cells in the MTSs, we exploited microglia as cellular transporters for NPs by virtue of their capacity to penetrate the tumour mass. The efficacy of BTZ-NPs delivered through microglia was also assessed.

To explore NPs transport, we increased the GBM model complexity, by including angiogenesis through a microfluidic platform (OrganoPlate® Graft, MIMETAS). The device has a central chamber to house the MTS within an extracellular matrix (ECM) gel and two lateral perfusion channels, which were seeded with human

cerebral microvascular endothelial cells (HBEC-5i) to mimic blood vessels. The administration of angiogenic signals induces vessel sprouting towards the ECM gel and the MTS. Once the vascularization procedure was optimized, the morphology and integrity of the microvasculature was assessed through immunostaining and perfusion assays. Extravasation of free NPs and microglia was monitored in the vascularized model with fluorescent markers and cellular tracers to identify the most effective carrier. CD31-staining confirmed the homogeneous presence of endothelial cells forming tight junctions (observed by ZO-1 staining). The microvasculature replicates the retention of 120 nm-diameter NPs observed in previous *in vivo* studies. These promising results point to the possibility of updating the model to a higher level of complexity, for instance by including other TME components, like pericytes and astrocytes. Moreover, the model can be used to investigate nanocarrier- and cell-mediated transport through the BBB to ensure targeted, effective drug accumulation with minimal adverse effects.

# Table of Contents

# List of Tables

# List of Figures

# Acronyms and abbreviations

**ACN** Acetonitrile

**ATP** Adenosine triphosphate

**BBB** Blood-Brain Barrier

**BTZ** Bortezomib

**BTZ-NPs** BTZ-loaded Nanoparticles

**CNS** Central Nervous System

**CSC** Cancer Stem Cell

**dd$H_2O$** Double-distilled Water

**DiD** 1,1-Dioctadecyl-3,3,3-tetramethylindodicarbocyanine

**DLS** Dynamic Light Scattering

**DSPE-PEG** 2-Distearoyl-sn-glycero-3-phosphoethanolamine-Poly (ethylene glycol)

**ECM** Extra-cellular matrix

**EGF** Epidermal Growth Factor

**EGG-PG** L-$\alpha$- phosphatidylglycerol (Egg, Chicken) (sodium salt)

**EMT** Epithelial-Mesenchymal Transition

**FBS** Fetal Bovine Serum

**FGF** Fibroblast Growth Factor

**GBM** Glioblastoma

**GFP** Green Flurescent Protein

**GSC** Glioblastoma-associated Stem Cell

**HBSS** Hanks' Balanced Salt Solution

**HEPES** -2-hydroxyethylpiperazine-N-2-ethanesulfonic acid

**MEM** Minimal Essential Medium

**MGMT** O-6-methylguanine-DNA methyltransferase

**MTS** Multicellular Tumour Spheroid

**NPs** Nanoparticles

**OCT** Optimal Cutting Temperature

**PBS** Phosphate Buffer Saline

**PDI** Polydispersity Index

**PDGF** Platelet-derived Growth Factor

**PFA** Paraformaldehyde

**Rod-NPs** Rodhamine-labelled Nanoparticles

**RT** Room Temperature

**SRS** Stereotactic Radiosurgery

**TAM** Tumour-associated macrophage

**TMZ** Temozolomide

**TME** Tumour Microenvironment

**WHO** World Health Organization

**VEGF** Vascular Endothelial Growth Factor

# Introduction

## Glioblastoma

Malignant tumours are a leading cause of mortality, responsible for about 10 million deaths worldwide (i.e. one-sixth of all deaths). Their incidence continues to rise due to increased life expectancy: according to the World Health Organization (WHO); cancer was the first or second leading cause of death before the age of 70 in 2019[1]. Although brain tumours account for only a small percentage of cancer-related deaths (2.5%), they are among the most problematic due to poor treatment outcomes. Gliomas, which arise from the glial cells in the brain, represent around 80% of all malignant central nervous system (CNS) tumours [2]. The 2016 WHO Classification of Tumors of the Central Nervous System categorized the different gliomas according to their histological nature, genetic characteristics, and hazard grade. Among them, glioblastoma (GBM) is the most frequent and most malignant form of brain tumours. This grade IV diffuse glioma is characterized by considerable cellularity, high mitotic activity, vascular proliferation, and necrosis [3]. This glioma was previously known as *Glioblastoma Multiforme* due to the presence of pleomorphic cells (i.e. differently shaped and sized).
In 61% of cases, GBMs occur in the four brain lobes, especially the frontal and temporal one. However, they can also be located in other areas of the CNS, such as the brain stem, the cerebellum or the spinal cord[4].
Currently, most glioblastomas have no clear cause. However, ionizing radiation has been identified as a risk factor [5]. Exposure may occur, for example, through repeated exposure in the workplace (e.g., in nuclear power plants), but potentially also as a consequence of radiation therapy on the brain. Moreover, approximately 5% of patients have a family history of gliomas. Although some of these cases are related to the presence of genetic syndromes such as neurofibromatosis, most familiar gliomas have no recognisable genetic basis [6].
The incidence of GBM is low compared to other cancers (less than 10 cases per $100{\cdot}000$ inhabitants) [7]. However, the median survival is only 14.6 months, and has not improved. Despite the development of combined current treatments, the five-year survival rate is still below 5% [7]. This dismal outcome has made the

study of GBM an attractive research area to develop new therapies and more reliable models [8] [9] [10]. The complexity of treatment lies in the anatomical location of the tumour and its peculiar heterogeneity. For instance, the high invasiveness in the CNS makes complete surgical resection practically impossible, while cancer-associated stem cells, difficult to eradicate, drive chemoresistance and radioresistance, promoting tumour recurrence.

## GBM Classification

Historically, GBM was defined as *primary* when it was diagnosed at the first biopsy, without any evidence of precursor lesions. On the contrary, *secondary glioblastomas* derive from the evolution of a preexisting low-grade astrocytoma [11]. The WHO proposed a classification based on the presence of IDH1 mutations in the first/second base of codon 132 [12]. These alterations appear in diffuse or anaplastic astrocytomas but persist during the progression to secondary glioblastoma. Since they emerge *de novo*, primary glioblastomas do not show IDH1 mutations (i.e. they are *IDH-wildtype*). The IDH1 mutation impairs isocitrate dehydrogenase 1 activity in the Krebs cycle, leading to an accumulation of 2-hydroxyglutarate [13]. This oncometabolite produces a defect in collagen maturation, influencing glioma progression by inducing basement-membrane aberrations. The genomic abnormality also favours the appearance of a hypermethylated phenotype, which is usually associated with the greater efficacy of clinical treatments. In fact, in secondary glioblastoma, the mean overall survival is about 31 months (compared to 15 months in IDH-wildtype tumours) after surgery, followed by a combination of chemotherapy and radiotherapy [12]. However, the clinical outcome may also be related to the characteristic age distribution. The average age of patients with primary glioblastoma is around 60, while secondary lesions are frequently diagnosed in younger patients (average 45 years) . The diverse origins of the two lesions also translate into different anatomical localizations. While primary tumours are widespread, IDH-mutant GBMs are mainly located in the frontal lobe (probable site of tumour precursors).
There are also alternative classifications based on the expression of characteristic gene markers that identify four subclasses of GBM with different phenotypes.

- The *classic subtype* is characterized by high-level epidermal growth factor receptor (EGFR) gene amplification. Although EGFR overexpression increases chemoresistance, molecular therapies may target the receptor and improve prognosis [14]. This subclass lacks TP53 mutations, although this genomic alteration is the most frequent in glioblastomas. Since the gene encoding the p53 protein is involved in maintaining genomic stability, mutant TP53 hinders tumour suppression activity. Hence, it may decrease overall survival [15]. Finally, the gene expression of cells belonging to this group is similar to

astrocyte patterns. This evidence suggests the possibility that both populations derive from common progenitor cells [16].

- The *mesenchymal subtype* shows neurofibromatosis type 1 gene (NF1) alterations. Base deletions or losses in the sequence of this gene can reduce the expression of Neurofibromin 1, an oncosuppressor protein. Although these mutations are associated with a worse prognosis in lower-grade gliomas, mesenchymal GBMs morbidity is similar to the classic subtype [17]. As the denomination suggests, the subclass expresses various mesenchymal markers like CHI3L1 and MET. Nevertheless, the cells manifest also increased activity related to astrocytic markers, which are possible evidence of epithelial-to-mesenchymal transitions within the tumour [18].

- The *proneural subtype* manifests various oligodendrocytic signature markers. However, changes in platelet-derived growth factor receptor alpha (PDGFRA) expression represent the foremost defining feature. This receptor promotes the proliferation and differentiation of progenitor cells into oligodendrocytes [19]. The overexpression of PDGFRA characterizes lower-grade gliomas, like diffuse or anaplastic astrocytomas and oligodendrogliomas. As secondary glioblastomas evolve from anaplastic astrocytomas, they also have this characteristic mutation. Thus, while there are primary tumours of all four subtypes, IDH-mutant tumours are all proneural lesions. Therefore, even though not all proneural GBMs share these alterations, point mutations in IDH1 represent a marker to identify this phenotype.

- According to the original classification suggested by Verhaak et al., the fourth cluster of lesions is the *neural subtype*. The class shows a strong expression of neuron genetic marker but also some similarity with oligodendrocytes and astrocytes [16]. However, Wang et al. observed that this subtype involves non-tumour cells in the GBM microenvironment [20]. Hence, more recent studies illustrated the existence of a single cluster for the proneural and neural subtypes.

## Tumor microenvironment

The clinical outcome of GBM is heavily limited by the histological heterogeneity of the tumour and its ability to alter the surrounding environment. The *tumour microenvironment* (TME) includes different (cancerous and non-cancerous) cells, growth factors, and enzymes that support the growth of the lesion and protect the tumour from the immune system and from pharmacological treatments. GBM actively modifies the TME and recruits cells by releasing cytokines, chemokines, growth factors and enzymes [21]. Knowing and studying this mutual interaction

between GBM and TME is indispensable for developing new supportive treatments and understanding which mechanisms hinder the efficacy of existing therapies.

### Histologic features of the bulk tumour

GBMs share many relevant features with other gliomas s uch as increased cellularity, nuclear atypia, and mitotic activity [6]. They also have necrotic zones due to the high proliferative capacity of the cells. The uncontrolled expansion causes the formation of local areas of hypoxia and subsequent cell death. However, hypoxia induces the release of vascular endothelial growth factor (VEGF) in primary GBM [22]. This factor promotes abnormal blood vessel sprouting, leading to the formation of new tumour microvasculature. In addition, increased VEGF secretion hinders the expression of tight junction proteins. The event facilitates fluid accumulation in the tumour mass, thus producing extensive peritumoral oedema, i.e. the major cause of neurological symptoms. Nevertheless, since secondary GBMs have a low growth rate, the necrotic core extension is usually modest. The formation of tumour microvessels is also less than in primary lesions because IDH-mutant cells do not overexpress genes associated with VEGF release.
GBMs histological heterogeneity is the principal source of outcome variability. Contrary to original assumptions, glial cells are not the only progenitors of GBM. Numerous cell populations with genetic characteristics of neural stem cells can give rise to the lesion. Hence, the wide range of cell sources produces a high variability in the subclasses phenotypes. Genomic differences also result in various responses to therapy. For instance, the classical GBM has the most favourable survival rate, whereas the proneural subtype has the worst prognosis [16]. At the same time, a single tumour may present a distinct combination of various subtypes. Additionaly, the 2016 WHO classification recognizes also three morphologic rare variants for IDH-wildtype glioblatoma:

1. *Gliosarcomas* (~2% of all GBMs) are biphasic tumour with both glial and mesenchymal components. Nevertheless, despite histopathological differences, the efficacy of standard treatment is similar to that of GBM [23].

2. *Giant cell glioblastomas* (~1% of all GBMs) consist of large cells with marked nuclear pleomorphism and atypia. Since this variant is more vulnerable to Deoxyribonucleic acid (DNA) damage, it is often associated with an increased survival rate [24].

3. *Epithelioid glioblastoma* features large epithelioid (or, occasionally, rhabdoid) cells with abundant eosinophilic cytoplasm and prominent nucleoli. The variant is more common in young patients, with an average age of around 26.3 years [25].

### GBM associated Cancer Stem Cells

GBMs include tumorigenic cells with undifferentiated neural cells markers (e.g., nestin). These *cancer stem cells* (CSCs) display self-renewal, proliferation, and differentiation. CSCs initiate the lesion but may also cause tumour recurrence. Furthermore, they are responsible for the resistance to conventional treatments (radiotherapy and chemotherapy). CSCs resides in the tumoral niches. Within GBMs, there are three functionally distinct niches to protect CSCs, as schematized in Figure 1.

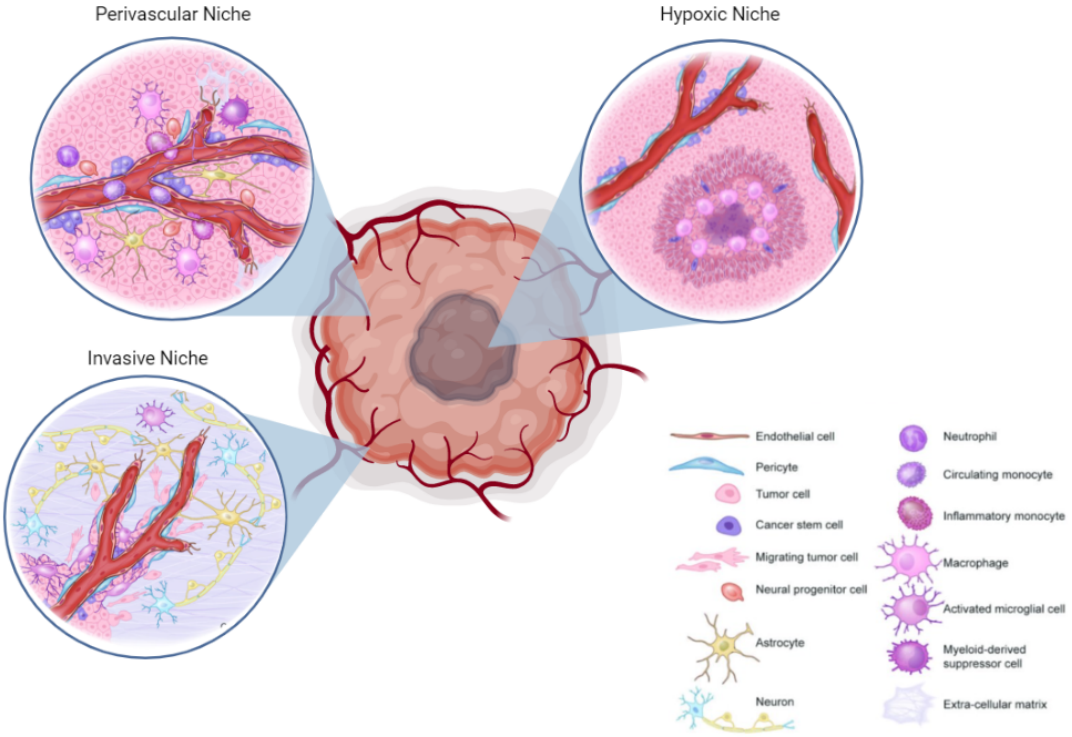


**Figure 1:** Schematic representation of tumour niches within the GMB. Image adapted from Hambardzumyan et al. [26] with Biorender.com.

The *perivascular GBM niche* is a multi-cellular structure located nearby the abnormal angiogenic vasculature. It includes both neoplastic (CSCs) and non-neoplastic cells. CD133-positive CSCs release VEGF to induce pericyte detachment and basement membrane degeneration [21]. These events produce abnormally enlarged vessels that grow in poorly organized and dysfunctional vascular structures (defined as glomeruloid microvascular proliferation). Vasculature dysfunctions may alter blood flow and hinder oxygen supply, inducing the formation of local necrotic regions. Poorly proliferative tumour cells with enlarged nuclei migrate from these

hypoxic areas forming *pseudopalisades* in the nearby tumour bulk. However, these phenomena do not slow down tumour growth, as they promote the formation of *hypoxic GBM niches*. These niches contain CSCs that have become resistant to chemotherapy and radiotherapy due to activation of self-renewal genes induced by hypoxia-inducible factors. These cells produce proinflammatory signals that reduce resident macrophages ability to engulf necrotic debris. Moreover, hypoxic CSCs may transdifferentiate to endothelial cells that promote microvasculature hyperplasia (combined with *tumour-associated macrophages*, TAMs, pro-angiogenic action)[26]. Finally, *invasive tumour niches* are located at the edge between the tumour and the normal brain parenchyma and are surrounded by functional vasculature. Here, displaced astrocytes, previously involved in tissue homeostasis, support CSCs and promote tumour infiltration. Indeed, cells in these niches undergo epithelial-mesenchymal transition (EMT) and migrate through the vessels, infiltrating other tissues and reducing the effectiveness of surgical resection.

### Non-neoplastic cells in GBM TME

The TME includes not only neoplastic populations but also stromal cells. GBMs release cytokines, chemokines, growth factors and enzymes to modify the surrounding microenvironment and recruit other cells to support its progression. In fact, tissue-resident cells such as neurons and astrocytes or immune cells can heavily influence GBM progression and prognosis [27].
For instance, TAMs are other relevant actors in the TME as their presence is inversely related to patient survival [26]. Different TAM populations such as bone marrow-derived macrophages (BMDMs) and tissue-resident microglia play different roles in tumour progression. Overall, these cells represent about one-third of the tumoral tissue. In particular, microglia promotes axon development and removes apoptotic cells to maintain homeostasis. However, they also play a pivotal function in cancer progression. Microglial cells switch from pro-inflammatory (M1) to anti-inflammatory (M2) phenotypes when exposed to immunogenic antigens or interleukins (IL), respectively. GBM cells produce IL10, transforming growth factors $\beta$ (TGF-$\beta$) and glucocorticoids to promote the proliferation of M2 microglia. M2 polarized macrophages enhance tumour expansion. Since TAMs reside predominantly, although not exclusively, in the perivascular tumour niche, they are likely to be recruited mainly by CSCs. Moreover, TAMs increase matrix metalloproteinase 9 (MMP 9) expression, promoting extracellular matrix (ECM) degradation and enhancing CSCs invasion [21].
GBM tumour cells recruit thymus-derived natural regulatory T-cells (nTregs). An increased presence of nTregs is related to an increase in immune escape ability due to the downregulation of the type I interferon (IFN)-based antitumour response.
Finally, microvasculature endothelial cells, pericytes, and astrocytes constitute

the *blood-brain barrier* (BBB). The BBB is a CNS neurovascular unit that provides highly selective permeability by tightly controlling the transfer of ions and molecules to the brain [28]. However, GBM cells displace non-neoplastic astrocytes and release factors that alter vessel integrity. These abnormalities hinder the barrier effect, increasing the accumulation of circulating immune cells, which may interact with CSCs and tumour cells supporting GBM progression. However, despite these abnormalities, many anticancer drugs are unable to cross the BBB. Hence, it represents is the main obstacle to chemotherapy unless appropriate transporter are used to promote accumulation at the target.

## Treatment strategies

GBMs are ordinarily diagnosed through magnetic resonance imaging or computed tomography. Common symptoms include headaches, seizures, peritumoral oedema, venous thromboembolism, and fatigue. Furthermore, patients can suffer from different cognitive dysfunctions, such as confusion, memory loss, or personality changes [6]. There are several treatments used to alleviate these symptoms. For example, corticosteroids can reduce peritumoral oedema, while antiepileptics are administered in cases of seizures [3]. However, these procedures are not suitable for all patients and may cause side effects. Moreover, they are not effective in limiting tumour growth and neurological dysfunction, so neurosurgery or other therapies that act directly on the tumour are required.

**Surgical resection.** Standard therapy involves maximal surgical resection. Moreover, tissue samples can be harvested during surgery for histological/molecular analysis or for use in customised *in vitro* models. In general, removal of large areas is associated with increased life expectancy [18]. Nevertheless, the extent of the resection must balance the desire to minimise the residual volume of the tumour with the need to preserve brain function. Although patients have a higher survival prospect if they undergo extensive resection, the infiltrative nature of GBMs limits the effectiveness of this treatment. In addition, some gliomas are inoperable due to their critical or deep location. Therefore, alternative or adjuvant therapies are needed to ensure complete removal of the residual tumour and reduce the risk of recurrence.

**Radiotherapy.** Radiation therapy applies high doses of radiation to induce DNA damages. This phenomenon may promote cancer cell apoptosis, necrosis, or senescence, thus reducing the tumour mass. The combination between surgery and radiotherapy may increase survival from 3-4 months to 7-12 months. Conventional radiotherapy consists of 25 to 35 treatments: partial-field external-beam irradiation (1.8 to 2.0 Gy) is delivered daily for 5–7 weeks (60 Gy in total) [29]. Clinical tests have shown that whole-brain exposure does not provide extra benefit compared to

partial irradiation. Instead, non-localised exposure increases the risk of side effects in healthy tissues adjacent to the tumour. However, delivering radiation to smaller surface areas requires innovative techniques to target infiltrating tumour cells. For instance, *stereotactic radiosurgery* (SRS) provides a focused treatment towards target regions while limiting toxicity to normal tissues. SRS may be employed to treat recurrent glioblastomas or as a complementary treatment after conventional external beam radiotherapy [30]. Nevertheless, since the radiation resistance of tumour cells may hinder the therapeutic efficacy, coadjuvant chemotherapy is often adopted to reduce the recurrence rate.

**Chemotherapy.** The use of drugs and target molecular agents has become increasingly important in recent years as an adjuvant treatment against GBM. In particular, chemotherapy involves the administration of different classes of drugs or hormones that induce the death or limit the proliferation of cancer cells.
For instance, the *Stupp protocol* employs temozolomide (TMZ) in combination with radiotherapy to improve the survival rate of patients with high-grade gliomas. During the six weeks of radiotherapy, TMZ is administered at a daily dose of 75 mg/m$^2$. After a 1-month rest period, TMZ treatment begins with a daily dose of 150 mg/m$^2$ for 5 days in the first month. If the patient can withstand the therapy, the daily dose is increased to 200 mg/m$^2$ for 5 consecutive days each month until the end of the six-month treatment period [31]. Although the treatment produced satisfactory results in phase III clinical trials, efficacy may be limited by the chemoresistance of some tumour cell populations, particularly glioblastoma stem cells. Moreover, TMZ side effects include increased risk of haematological complications, fatigue and infections [32].
Another antineoplastic agent for the treatment of glioblastoma is Carmustine (bis-chloroethylnitrosourea, BCNU). The alkylating agent can be supplied through intravenous injection or locally administered using biodegradable polymers wafer (Gliadel®). Gliadel® allowe local administration with reduced systemic toxicity, but the penetration capacity of the drug is limited and additional treatment may be required [29]

**Targeted Molecular Therapies.** Chemotherapeutic agents have a nonspecific action. Hence, side effects can arise due to the action on healthy cells in the surrounding tissues (e.g. hair loss). Therefore, researchers have developed new therapies to block tumour progression by targeting specific molecules involved in the growth and spread of cancer cells. Several studies have evaluated different molecules for targeted inhibition of receptor tyrosine kinases or signal transduction [6]. For example, preclinical phase I and II studies confirmed that Gefitinib, a reversible tyrosine kinase inhibitor that affects EGFR action, was effective in reducing the risk of GBM recurrence without significant side effects [33]. Similar studies have also been performed on VEGFR- [34] and PDGFR-associated inhibitors

[35]. However, the use of such agents has limited efficacy due to the redundancy of pathways exploited by cancer cell metabolism and the difficulty in identifying effective molecular targets. Other target therapies may act on factors contributing to chemoresistance. Chemoresistance may emerge due to the upregulation of multidrug resistance genes or the overexpression of repair enzymes. For instance, O-6-methylguanine-DNA methyltransferase (MGMT) is an enzyme involved in the resistance to TMZ, thanks to the production of a DNA damage repair protein that removes alkylating agents [36]. The use of inhibitors or the introduction of methylating agents that silence the MGMT gene promoter is a valuable adjuvant treatment against recurrent malignant gliomas [29]. Since gliomas are highly vascularized tumours, they may be susceptible to angiogenesis inhibitors. Specific monoclonal antibodies that bind to the VEGF limit the formation of new vessels and, consequently, the supply of substances and nutrients, reducing tumour growth. For instance, the combined delivery of bevacizumab (anti-VEGF) and irinotecan (a methylating agent) improves the survival rate among patients with recurrent glioblastomas [29]. Another example of target therapy is the use of proteasome inhibitors. These inhibitors, such as Bortezomib, interfere with the activity of the ubiquitin-proteasome complex, which is responsible for the degradation of misfolded, damaged, or redundant proteins. Inhibition of this pathway leads to the accumulation of misfolded proteins within the cytoplasm, compromising cellular homeostasis and survival (especially in cancer cells, which exhibit altered catabolism) [37]. Tests have confirmed that Bortezomib, which has already been employed to treat multiple myeloma, may hinder glioblastoma growth and enhance TMZ efficacy [38].

# Three-dimensional models for Glioblastoma

## Benefits of three-dimensional *in vitro* models

The histological complexity and genomic variability of tumours have hampered the study causes and factors involved in their progression [8]. Identifying and assessing new therapeutic agents is a long and expensive process, as it requires several preliminary studies performed mainly on animal models. However, these preclinical trials are costly and require a prolonged approval process and frequent controls by ethics committees, which must verify animal welfare at every step of the study [39]. Moreover, the European regulations, in addition to strictly disciplining *in vivo* studies, prescribe the fulfilment of the *"principles of the 3Rs"*, setting as the ultimate goal the gradual replacement of trials on animals [40]. These principles include reducing the number of animals involved in studies, refining experiment procedures to diminish subject suffering, and replacing animals with alternative models. Hence, there is a clear need to develop reliable *in vitro* models that replicate

the structure of healthy and pathological tissues. Several studies have focused on the design of more complex cellular models that replicate the three-dimensional structure and heterogeneity of tumour tissue [41]. These systems are of particular interest to the pharmaceutical industry, as high-throughput screening devices for the research and development of new chemotherapeutic drugs [42].
In the specific case of GBM, current knowledge does not allow the creation of reliable models that can completely replace animal studies. However, they can be used to select agents and delivery procedures to be tested on animals, reducing the number of trials and subject required [39]. Furthermore, gene and protein expression can not be easily analyzed *in vivo*, but these examinations can be performed *in vitro*. Moreover, *in vitro* models are suitable to isolate the contribution of single factors and investigate drug response [41]. However, models must replicate the histopathological structure and TME complexity to be truly predictive [8]. Therefore, the open challenge is to develop three-dimensional models with co-cultures of different cell populations (tumour, stem and non-neoplastic) that replicate intratumoral cell-cell and cell-ECM interactions. Recent studies proposed to include other elements that play a pivotal role in GBM progress but are tough to replicate *in vitro*, such as immune response and tumour angiogenesis. In the future, it is desirable to increase the complexity and heterogeneity of *in vitro* models while preserving their replicability and minimizing variability. The final aim is to provide meaningful yet usable tools for personalized studies concerning new treatments.

### Limitations of glioblastoma *in vivo* models

Nowadays, drug discovery requires numerous studies and optimization steps under diverse conditions, which are difficult to verify in animal models due to ethical and cost constraints [43].
The most commonly used *in vivo* models are based on human cells *xenograft* into mice. Early studies involved subcutaneous implantation of lineage cells, but the results were of little significance because of the different anatomical locations. In addition, in situ tumours developed from lineage cells also exhibit genotypic and phenotypic differences from the original GBM. As a result, there is now a greater focus on patient-derived xenografts with orthotopic implantation of biopsy-derived cells (eventually subjected to an *in vitro* culture step). The models thus obtained maintain the phenotype and histological complexity of native GBM [44]. However, they are characterized by a very high variability (due to both mouse and patient). In addition, since only immunodeficient mice can be used, the model does not replicate the effective immune response (which in any case is different between animal and human). To overcome these limitations and bypass the technical challenges associated with implanting biopsies in a critical area such as the brain, genetically engineered or syngeneic mouse models have also been adopted.

Nevertheless, there are still questions about how controllable these models are and how well they reflect the histopathology of human GBM [44]. In addition, all of the models described require long timescales and high costs to induce GBM formation and limit the type of phenotypic and gene analyses that can be performed.

### Limitations of glioblastoma two-dimensional *in vitro* models

Two-dimensional monolayer culture systems are the most commonly used to enable cell growth. However, their validity as predictive models is limited, especially for complex tumours such as GBM. For instance, 2D culture can not replicate oxygen, nutrients, and pH gradients that characterize GBM microenvironment and heavily influence cellular growth [45]. The cell surface is exposed to contact with the medium and with the drug dispersed in it. This non-physiological availability of the therapeutic agent does not allow consistent evaluations of its efficacy: many chemotherapeutics that showed promising results in these preliminary studies proved to be ineffective *in vivo*[8].
Coculture of neoplastic, non-neoplastic and stem cells can improve the model. However, 2D cultures do not reproduce the complex interactions between tumour cells and the microenvironment [41]. The non-biomimetic geometry, combined with the absence of ECM-like support and microvasculature, severely limits predictive efficacy [46]. Specifically, the deficiency of TME characteristic signals induces genetic and epigenetic alterations in GBM-associated CSCs, leading to loss of stemness and other chemoresistance associated markers [8]. Adding growth factors can promote CSCs expansion in 2D cultures *in vitro* but may also alter gene expression relative to the original lesion [47]. For this reason, it is advisable to replace two-dimensional models with other systems that replicate components, geometry, and interactions observed *in vivo*. In this way, it is possible to preserve the original genotype and obtain accurate predictions of GBM progression or treatment efficacy.

### Key features of three-dimensional *in vitro* models

A satisfactory model should mimic tumour geometry and composition. Specifically, it must contain several populations representative of the cell types present in the tumour. Therefore, coculture systems of differentiated tumour cells with CSCs, possibly supported by resident stromal(e.g, fibroblast) or immune (e.g., microglia or T-lymphocytes) cells, are preferred [8]. Moreover, in vitro models should simulate other factors that may influence drug efficacy, such as cell interactions with the ECM and the presence of tumour microvasculature [48].
Since mechanical stimuli directly influence cell differentiation, proliferation and migration, culture supporting materials should biomimetically replicate the mechanical and chemical properties of the tumour matrix. The interaction of cells

with the ECM (or with ECM-like structures) should promote the maintenance of the stemness of CSCs and induce the processes of EMT, increasing aggressiveness and invasiveness [8].
Tumor blood vessels can be reproduced *in vitro* using bioprinting techniques[46] or microfluidic devices[48]. Their presence also enables to mimic drug distribution in tissue and to replicate the barrier effects. In fact, the endothelium of brain capillaries is characterized by tight junctions that limit the penetration of drugs and pathogens[46]. Moreover, other resident cells, such as astrocytes and pericytes, surround blood vessels and selectively control substances exchange within the cerebrovascular system [28]. Models capable of replicating these phenomena can be used to test and optimize drugs and nanomedicines specifically developed to overcome such obstacles and selectively target cancer cells [41].

## Spherical GBM Models

The first three-dimensional models developed, which are still the most commonly used in research, were the *spherical GBM models*. These are spherical geometry structures made of tumour cells (alone or in coculture), initially obtained with scaffold-free techniques but currently integrated with gels and matrices that simulate the tumour ECM [8]. These culture methods reproduce cell-cell interactions and other characteristics observed *in vivo*, such as chemoresistance and invasion ability. However, necrotic areas may often arise, and long-term culture is very challenging. In addition, cell-TME interactions, characteristic of the tumour mass, are not present. Nevertheless, the last issue can be solved by embedding the spherical culture in biomaterials that mimic the mechanical and biochemical properties of the GBM matrix, such as Matrigel® or agarose gels. Spherical cancer model includes neurospheres, tumor spheroids and Organotypic spheroids.

### Neurospheres

Neurospheres can be considered the first three-dimensional model of GBM. These cultures are derived from the proliferation of single-cell suspension of tissue-derived cancer cells or established cell lines. Neurospheres were initially developed as a culture method to preserve the stemness of neural stem cells [49]. Cells grow in low-attachment conditions within a serum-free medium supplemented with Fibroblast Growth Factor 2 (FGF-2) and Epidermal growth factor (EGF). This culture method replicates the 3D cell-cell interactions and metabolite gradients present in GBM. However, neurospheres present a vast necrotic core, limiting the growth to a maximum diameter of around 300 µm [50]. Moreover, neurospheres cells lack their interaction with ECM components. Alteration of culture conditions (e.g., by addition of fetal bovine serum, FBS) also leads to drastic phenotypic

changes with consequences such as differentiation, loss of infiltration capacity and transition to a two-dimensional culture state [8].

### Multicellular tumor spheroids

Multicellular tumour spheroids have long been used as high-throughput models for GBM. They are tightly packed cellular structures that differ from simple cell aggregates by the presence of intermediate junctions between adjacent cells. The first models mainly exploited monocultures of differentiated cells. Nevertheless, there are several studies proposing coculture systems with CSCs [8]. Spheroids can be made from either tumour cell lines or cells derived directly from the patient via biopsy. This second option, although promising for personalized medicine, is less adopted due to poor reproducibility and complex sample extraction.
The spheroid structure is heterogeneous due to the presence of gradients in oxygen and nutrient concentrations, similar to what occurs *in vivo* in GBM [8]. Three cell layers with different proliferation rates can be identified (Figure 2a). In the centre, a necrotic core is formed due to poor oxygen supply. Although it mimics the histology of the regions of GBM farthest from the vessels, it represents the main obstacle to the formation of models larger than a few hundred micrometres. The proliferative rim is the outermost layer characterized by a high growth rate, responsible for invasion processes modelled by inserting spheroids into matrices, gels or scaffolds [51]. Between these two zones, there is a quiescent layer, inactive and inert.
Spheroids can be easily produced using a variety of techniques. In particular, some cell types form spheroids spontaneously, whereas other populations require specific culture conditions (typically in the absence of adhesion). The most commonly used spheroid formation methods include:

- *Hanging drop methods* (figure 2b): the cells are dispensed in a drop of culture medium and incubated to make them fall to the tip and aggregate. The technique is simple and has high performance, but spheroids manipulation is complex [52].

- *Dynamic methods*(figure 2c): shakers and bioreactors provide constant agitation to prevent cell adhesion and promote spontaneous aggregation. The technique has a high yield but requires specific devices and cannot produce individual spheroids [51].

- *Microfluidics* (figure 2d): Flows in microchannels induce aggregation into droplets by cell suspension/oil emulsion or by accumulation in U-shaped microstructures [53]. Spheroids form rapidly, but extraction is difficult.

- *Non-adherent surface methods*(figure 2e): Cells are seeded on anti-adhesive surfaces and tend to accumulate at the bottom of the well. Cheap custom-made agarose substrates or commercial plates with U-shaped bottoms (giving well reproducible results) can be used.[41]

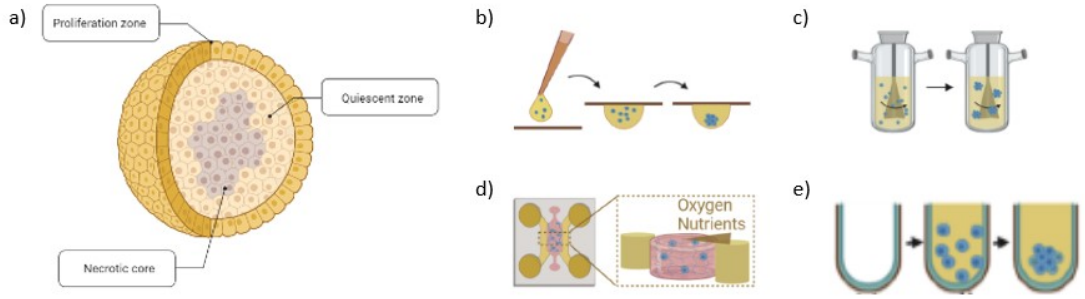


**Figure 2:** a) Characteristic layers of a spheroid. Created with Biorender.com. b)Hanging drop method. c) Dynamic method with a stirring biorector. d) Microfluidic devices for spheroid formation and culture. e) Non-adherent surface method. Adapted from Stanković et al. [41]

Spheroids are commonly employed for early drug screening tests, e.g, for the parallel assessment of different treatment concentrations. However, GBM MTS can be used in various other tests (including proliferation, invasion, and migration assays) [45] or as a component of organ-on-a-chip [46]. However, promising tumour spheroids with high similarity to GBM have also emerged in recent years. For instance, Tatla et al.[54] developed an MTS model to replicate both the histological complexity of GBM and the role of angiogenesis phenomena in tumour progression. The spheroids are composed of patient-derived primary GBM cells (including stem subpopulations). However, the model incorporates other prominent elements of the TME, such as vascular endothelial cells (human umbilical vein endothelial cells, HUVEC) and supporting stromal cells (human dermal fibroblasts, HDF). The model was used to study the phenomena of tumour angiogenesis and the role of hypoxia and growth factors (e.g., VEGF, bFGF). Figure 3a summarizes the main steps of spheroid development. Human GBM-derived cells (or NCH82 tumour line cells) and HUVECs were suspended in serum-free medium(SFM) and methylcellulose to form spheroids by the hanging drop method. The spheroids were then encapsulated in a fibrin gel (capable of supporting vascular sprouting) containing HDF. This tri-culture system promotes HUVEC angiogenesis: the newly formed capillaries sprout radially through the fibrin gel (Figure 3b). The co-culture with primary glioblastoma cells leads endothelial cells to produce vasculature of increased extension but lower interconnectivity. Moreover, vessel length increases

in hypoxia conditions. These phenomena replicate the behaviour of the tumour microvasculature observed in vivo, whereas lineage cells do not show these interactions with the capillary network. Immunohistochemical staining of vascularised spheroids shows the formation of CD31-positive primary GBM cells. This evidence suggests the presence of transdifferentiation phenomena also hypothesised *in vivo* [26]. The model presents unique biomimetic characteristics and represents an excellent tool to test antiangiogenic drugs. However, it has some limitations, such as the absence of perfusion in the capillaries and the non-physiological formation of sprouts. In fact, capillaries are formed from the tumour model outwards, whereas they usually start from the surrounding vessels and converge towards the tumour *in vivo*.

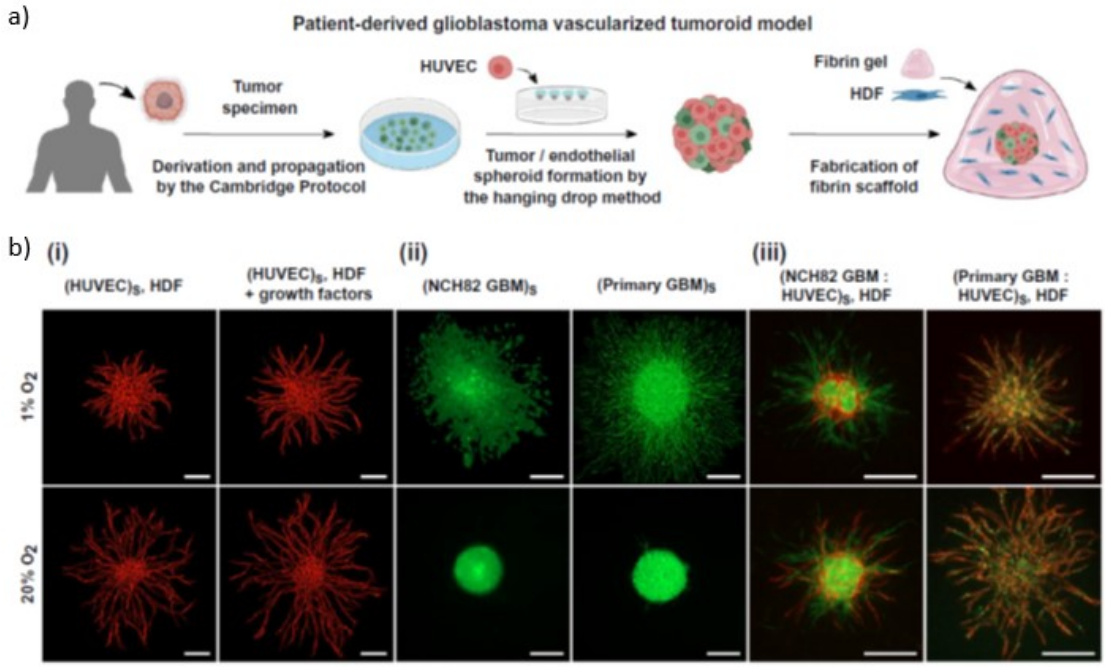


**Figure 3:** a) Illustration of the development of the vascularized spheroids. b) Fluorescence images confirming spheroid sprouting. (i) HUVEC (red) spheroid and HDF cells with or without growth factors; (ii) NCH82 or patient-derived GBM spheroids (green) and (iii) the full vascularized model with NCH82 or primary GBM, HUVEC and HDF cells. All the images were acquired 3 days after seeding in hypoxia (1% $O_2$) and normoxia (20% $O_2$) conditions. Scale bar 250 µm. [54]

### Organotypic multicellular spheroids

Organotypic multicellular spheroids (OMSs) are GBM fragments extracted ex vivo to entirely replicate TME complexity. Biopsy acquisition of non-dissociated samples

enables the collection of stromal and immune cells from the surrounding environment in addition to tumour populations [52]. Tissue pieces are then dissociated mechanically or enzymatically to obtain smaller constructs that will be cultured by the liquid overlay method until rounded spheroids are formed [8]. Although these models are highly biomimetic, their use is limited by the difficulty of resecting and harvesting large amounts of tissue from patients' GBM.

## Organoids

Another example of 3D self-organizing GBM model is represented by organoids.The structure of the organoids is formed entirely *in vitro* from single induced pluripotent stem cells (there are currently no successful studies using adult stem cells) [8]. Organoids have found application in various fields, such as the study of tumour angiogenesis, the analysis of interactions between GBM and non-tumour cells (in so-called 'mini brains') and the monitoring of progression and invasion phenomena under different treatment conditions. The definition of tumour organoids brings together a diverse set of GBM models capable of replicating the TME. Nevertheless, three main categories can be identified based on the development approach adopted.

### Genetically Engineered Brain Organoids

The first method of GBM organoid generation is the induction of localised gene modifications on healthy brain organoids to activate pathways associated with tumorigenesis. Most studies are based on organoids (also called mini-brains) made (according to protocoldefined by Lancaster et al. [55]) from single human pluripotent stem cells (hPSCs). Figure 4 schematizes all the steps required to prepare celebral organoids from hPSCS. Briefly, embryoid bodies (EBs) are generated from hPSCs in a 96-well U-bottom plate. EBs are then fed and monitored for about 6 days to induce germinal layer differentiation. Then, they are cultured with neural induction medium in 24-well plates. After 5 days, neuroectodermal tissues are dispensed to floating Matrigel droplets and grown for 4 days. At the end of this expansion phase, droplets are transferred in dynamic culture conditions (e.g., in a spinning bioreactor), with Cerebral organoid differentiation medium containing vitamin A to form mature organoids. The models replicate the physiological structure of the brain and the different subregions, including the cerebral cortex containing progenitor cells (which can differentiate in different populations).

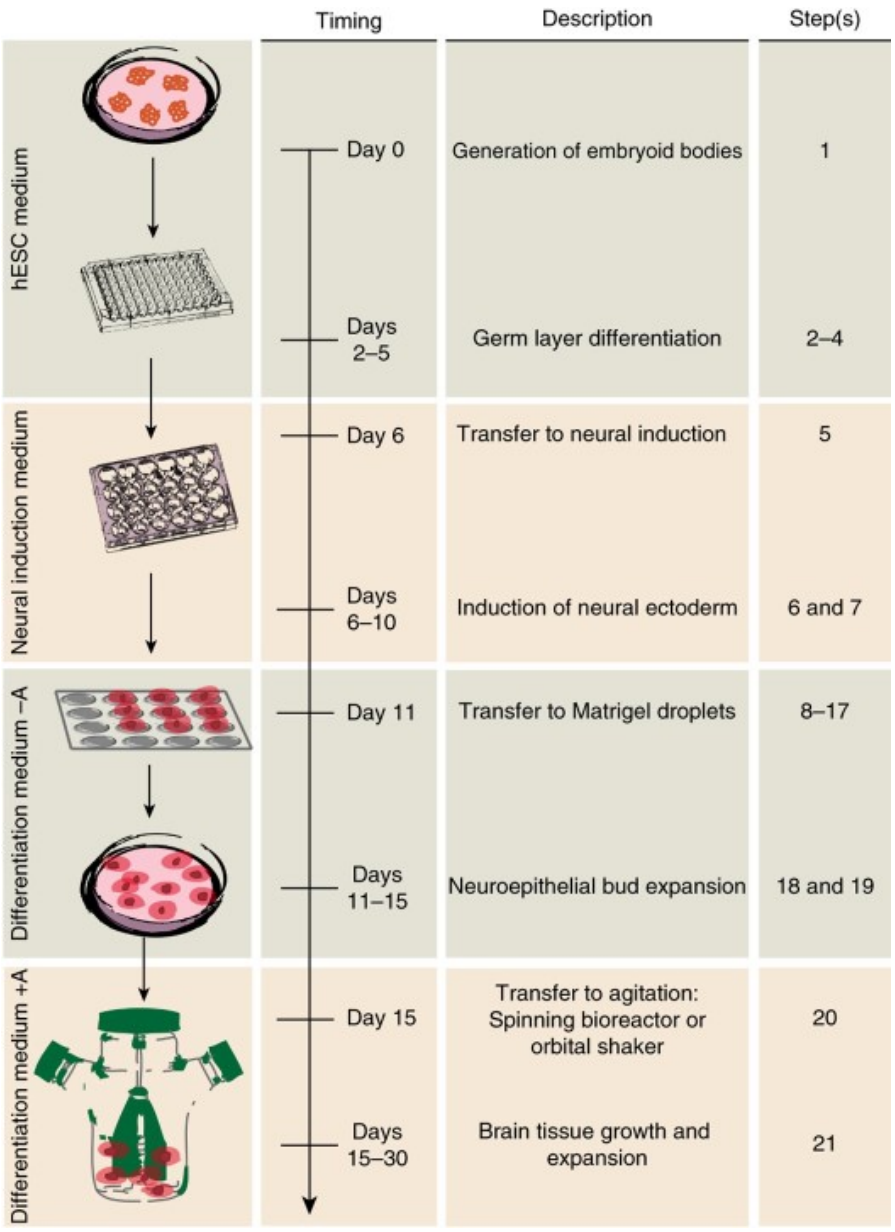


**Figure 4:** Lancaster protocol for cerebral organoid generation [55].

Subsequently, the same research group developed a three-dimensional tumour model called neoplastic cerebral organoid (neoCOR) from the gene modification of mini-brains formed with this technique [56]. The process of tumorigenesis was replicated by introducing plasmids coding:

1. Sleeping Beauty (SB) transposon-mediated to introduce inverted repeat sequences;

2. oncogenes flanked with inverted repeat sequences to induce oncogenic overexpression;

3. Green Fluorescent Protein (GFP)-coding sequences to track cells;

4. sequences expressing Cas9 enzyme and a guide RNA to decrease oncosuppressor genes expression through CRISPR–Cas9-based mutagenesis.

Figure 5a shows the key steps of cerebral organoid development and nucleofection. The plasmids were introduced exclusively into the neural stem and progenitor cells (NS/PCs), the main cellular sources of GBM. Correct transfection was verified by immunofluorescent staining of markers characteristic of different tumour and non-neoplastic populations, as shown in Figure 5b.

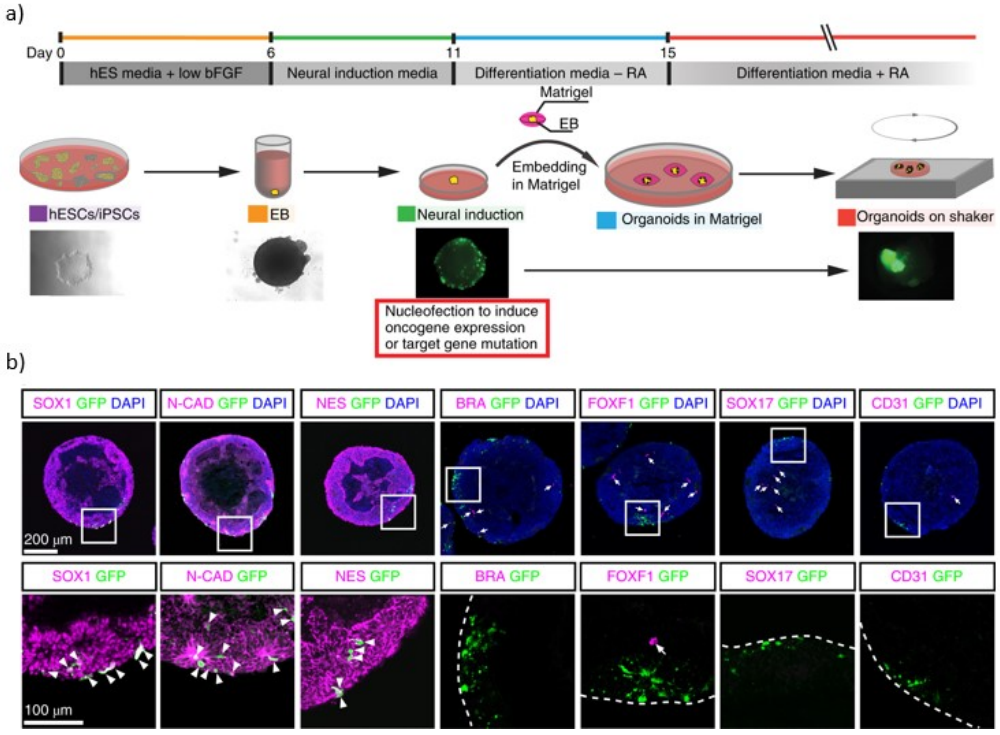


**Figure 5:** a) Illustration of the organoid culture process and the plasmid nucleofection method used. b)Immunostaining for the indicated markers 24 h after nucleofection [56].

The protocol successfully introduces 15 of the prevalent clinically relevant combinations of alterations observed in brain tumours. Analysis of the expression of oncogenes confirmed the presence of the expected mutations, while the study of the given cell transcriptome suggested the appearance of two different types of

tumours within the organoid depending on the aberrations produced: Primitive neuroectodermal tumours of the central nervous system (CNS-PNETs) or GBM. Since only a few cell clusters are involved within the cerebral organoid, the model is suitable for studying interactions between GBM cells and healthy tissue or analysing parenchyma invasion. Finally, neo-CORs were implanted in immunodeficient mice to verify the maintenance of self-renewal and immortality hallmarks. The immunohistochemical analysis confirmed that neo-CORs might expand in vivo while maintaining their subtype. All experimental evidence suggests the validity of the system as a drug screening tool, especially when modified to express firefly luciferase to enable tumour size monitoring. The same authors found satisfactory results in evaluating the efficacy of various EGFR inhibitors. The main limitation of this model, apart from the cost of developing and maintaining the organoids, is the absence of some key components of the TME, such as tumour microvasculature and immune cells. This complication could be overcome through coculture systems of organoids with endothelial cells and TAMs.

### Organoids derived from the primary tumour

Models based on genetically engineered healthy organoids represent well the interactions of GBM with non-neoplastic tissues but without fully replicating the elements present in the native TME. This problem can be solved by making organoids derived from the patient's tumour tissue (patient-derived organoids, PDOs) using techniques that preserve the cellular interactions between the different GBM populations (figure 6).
Hubert et al. [57] developed one of the first organoids produced entirely from human GBM with research applications. For the organoid formation, they replicated the method described by Lancaster et al.[55], but applied it to GBM fragments ground or brought into single-cell suspensions. At the end of the various culture steps, they obtained organoids several millimetres in size that replicated various elements of GBM, including the presence of a core of quiescent CSCs surrounded by a proliferative zone and the presence of pH, nutrient and oxygen gradients.

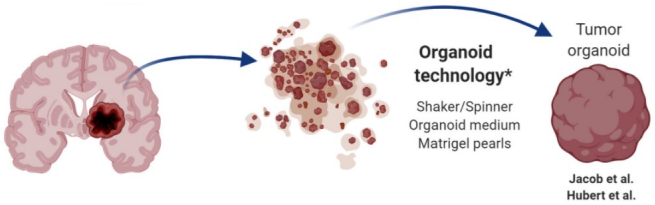


**Figure 6:** Developmental steps of PDOs from human GBM [8].
*The organoids techniques are normally optimizations of Lancaster's protocol.

More recently, Jacobs et al. [47] introduced a protocol for developing PDOs to preserve the structure and composition of human GBM (figure 7).
Samples were taken from the periphery of the GBM to obtain fragments of approximately 1 mm containing small portions of the necrotic core and components of healthy nerve tissue. No chemical or mechanical dissociation methods were used to preserve the cytoarchitecture of the tissue.
To prevent the formation of necrotic areas, the organoids were cut into smaller pieces after several weeks of culture. The culture was carried out in an orbital shaker to encourage the formation of rounded organoids and promote nutrient and oxygen diffusion. No growth factor was added to the medium to avoid the differentiation of CSCs present in the tissue.
Subsequent histological analysis of PDOs confirmed the same morphological and histological heterogeneity observed *in vivo.* PDOs extracted from different patients were collected in a bio-bank of the most commonly GBM mutations.
Gene sequencing showed that each sample had a unique gene set that was preserved in the corresponding PDOs. Gene expression also remained stable for 48 weeks. The organoids were also positive in some areas for the CD31 marker, confirming the maintenance of the native vasculature.
Orthotopic xenograft showed that PDOs could produce tumours with the original architecture and histology in immunocompromised mice. The presence of proliferative and progenitor cells was confirmed, both at the implantation site and in distal districts. The occurrence of satellite tumours, similar to those developed in the patient, was also assessed.
PDOs were used as an *in vitro* model to test the combined treatment of radiotherapy (10Gy) and weekly TMZ chemotherapy. Therapeutic efficacy was defined based on the expression of KI67, a factor correlated with improved prognosis. Given the high variability of the GBM studied, specific treatments were also analysed to confirm their efficacy in response to unique mutations.
Finally, the model was used to evaluate the efficacy of Chimeric antigen receptor (CAR)-T cell-based therapy on GBM. The results of the coculture of CAR-T cells and GBM organoids show that the treatment, despite the specificity, is not able to cause the complete elimination of the tumor.
Although PDOs replicate the structure of the TME well, it can be further improved by introducing cocultures with immune cells, which are currently not present in these models.

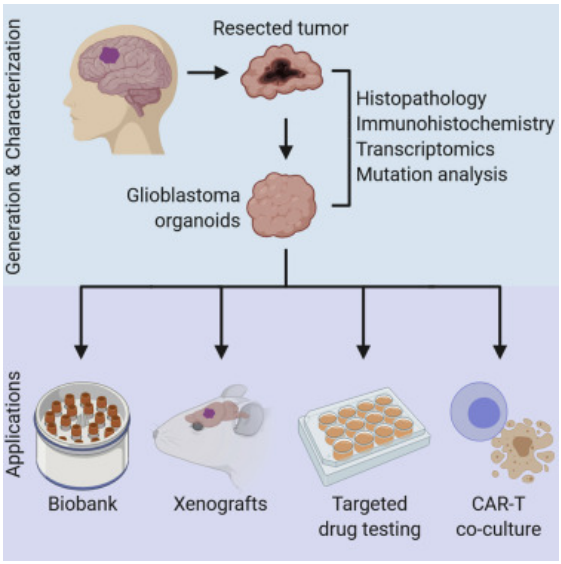


**Figure 7:** Production method and testing of GBM PDOs developed by Jacob et al. and possible application areas considered. [47]

### Healthy brain organoids coculture with GBM-derived cells

An alternative model aiming to replicate the interactions between healthy tissue and tumour cells and their role in the occurrence of GBM is the coculture of healthy brain organoids with GBM CSCs or tumorspheres. In this area, one of the most innovative studies has been the work of Linkous et al. [58] to develop the cerebral organoid model of glioma (GLICO). This model is also based on healthy brain organoids produced from PSCs using the protocol of Lancaster et al.[55]. The obtained organoids replicated several characteristic structures of the brain, similar to those observed in developing 20-week-old human fetal brains. Transmission electron microscopy confirmed the presence of glial cells and neurons with myelinated axons and dendrodendritic synapses.
Figure 8 summarizes the key steps in the development of the tumor model from healthy mini-brains. Mature brain organoids were cocultured for 24 h with GBM CSCs (harvested from patients and transfected with GFP) to induce tumour infiltration in miniaturised brains. As observed in human GBM *in vivo*, an infiltrative layer of CSCs forms and invades healthy tissue. Thus, tumour areas are present alongside healthy tissue infiltrated by stem cells. Histopathological analysis of the organoids showed the possibility of replicating key features of the tumour of origin, such as necrosis and aberrant proliferation.
GLICO models were then exploited to replicate the influence of TME on CSCs, thus replicating the resistance to chemotherapy and radiotherapy observed *in vivo* but not in 2D *in vitro* studies. Tests on GLICO models have shown that the

action of chemotherapeutic agents such as TMZ and bis-chloroethyl nitrosourea (BCNU) is considerably less promising than assumed by the decreases in viability observed in other *in vitro* studies. Furthermore, several non-ionising radiation treatments were applied on CSCs in organoids, confirming a tolerance to radiation therapy superior to that observed in two-dimensional culture. Further studies have confirmed that CSCs show increased survival when inserted into organoids, as they establish signalling interactions that support tumour growth as occurs with TME. The model described has great potential, especially for the possibility of developing patient-specific treatments or scaling up the method to high throughput studies. However, there are limitations in reproducibility and the model lacks characteristic elements of tumour tissue such as the vascular network.

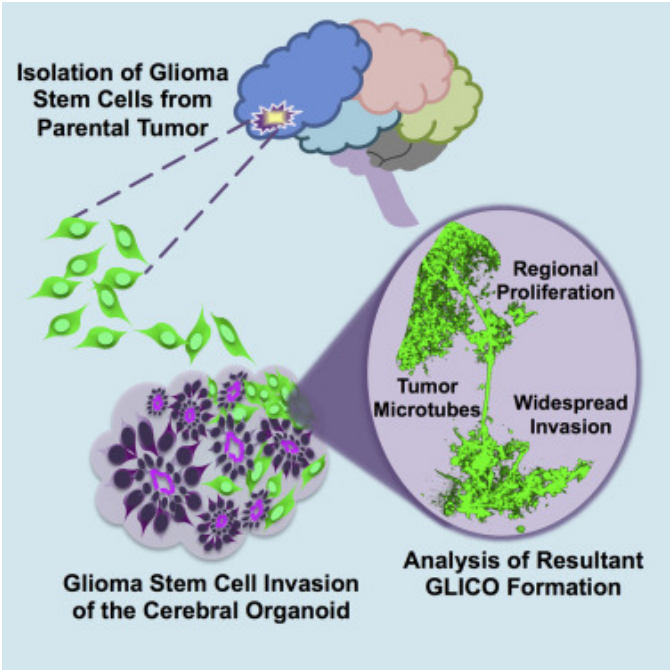


**Figure 8:** The illustration summarizes the principal steps to develop the GLICO model from patient-derived GBM cells and brain organoids.[58]

## GBM-on-a-chip

Organ-on-a-chips are in vitro models that use microfluidic systems, combined with cell cultures or engineered constructs, to replicate the functions and interactions between organs and tissues observed *in vivo*.[8]
Xiao et al.[48] developed a microvasculature-on-a-chip model to replicate the interactions between vessels and CSCs within the perivascular niche.
The device includes a central chamber separated by a set of micro-posts from two

lateral perfusion channels (figure 9a). GFP-labelled HUVECs are loaded in a fibrin gel precursor and dispensed in the central chamber. In a few days, primitive vessels were self-assembled and, then, sprouted in a microvessel network (figure 9b). The vessels were perfused with culture medium supplemented with VEGF, FGF and EGF to sustain vascular growth.
To replicate the interactions between GBM and vessels, patient-derived GS5 neurospheres were embedded in the HUVEC-containing gel. GSC5 are highly infiltrative, CSCS-enriched populations that are well suited to replicate GBM niches composition. The addition of these tumor cells also appears to enhance the development of the vascular network in terms of growth rate and number of branches (figure 9).
Biomimeticity and functionality of the microvasculature were confirmed by evaluation of characteristic protein expression. For example, the presence of VE-Cadherin, associated with endothelial adherent junctions, and collagen IV deposition was confirmed. Indeed, collagen IV is an index of mature vessel formation and an essential component of the microenvironment of the perivascular niche. Permeability assays showed that the absence of pericytes and stromal cells led to the formation of vascular walls that were less selective than those present *in vivo*.
Then, the authors studied the colocalization between microvasculature and stem (GS5) or differentiated (U87) tumour cells. The study confirms that stem cells are localized close to the vessels (like in perivascular niches) and promote network growth and branching. In contrast, differentiated cells compromise the stability of the forming network and arrange themselves in a disorganized way. The model also mimicked and monitored the migration mechanisms of CSCs through the vascular network using fluorescent tracers. The device allows to replicate different functionalities of the perivascular niche but should be optimized using cerebral vascular endothelium cells and including other components of the TME (e.g., immune cells, pericytes) to obtain more realistic drug screening assays.

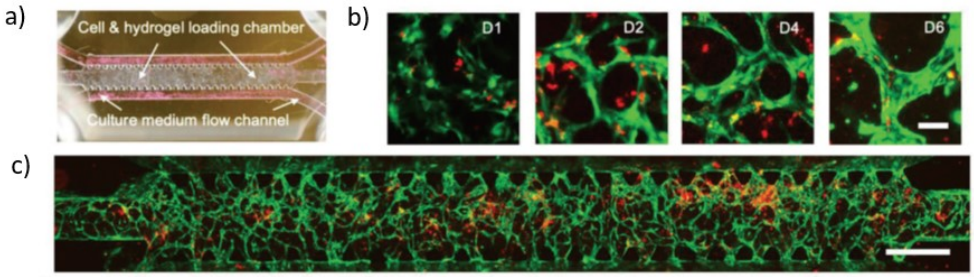


**Figure 9:** a) Microfluidic deviced designed by Xiao et al. b) Microvessel evolution in the first 6 days of development. GFP-HUVECs appear in green. Scale bar: 15 µm. c) Overview of the complete microvascular network formed by GFP-HUVECs (green) and GS5 (red) coculture. Scale bar: 1 mm. Adapted from [48].

Microfluidic chips can also be exploited to make simpler but usable models for high-throughput drug screening. Fan et al.[59] developed a multichannel microfluidic chip to produce and grow GBM spheroids for combined treatment assessment. Figure 10a schematize the manufacturing procedure. The device contains three channels and twenty-four culture chambers made of Poly(ethylene) glycol diacrylate (PEGDA) hydrogel obtained by UV soft lithography. The hydrogel, anti-adhesive but with mechanical properties similar to ECM, was fixed and cross-linked between two cover glasses, modified to accommodate three inlets (for medium and drug injection) and one outlet. The Christmas tree geometry generate a concentration gradients within the chambers by mixing differently the fluids inserted in the three inlets. The tests carried out by inserting two different dyes solutions in the lateral inlets (figure 10b) confirm that the outermost channels contain almost exclusively dyes coming from the closest inlet. Conversely, the central channels are filled by fluids with intermediate compositions. Therefore, by inserting two dye solutions in the lateral inlets and a viability indicator in the central one, it is possible to test different treatment ratios simultaneously to identify the most effective one.
The chip was then employed to evaluate the efficacy of combined treatment of Pitavastatin and Irinotecan on GBM spheroids. Spheroids were formed using the same chip due to the antiadhesive properties of PEGDA. U87 cells dispersed in the culture medium were injected into the central canal. Stagnant flow leads the cells to accumulate in the culture chambers, where they spontaneously aggregate due to the inability to attach to the walls. After seven days of culture, mature and viable spheroids were obtained. Then, the two drugs were simultaneously dispensed through the side inlets, while trypan blue dye was administered in the central one to monitor cell viability. The results confirmed that the most significant decrease in viability was observed in the central channel. In the lateral culture chambers, the viability changes were similar to those described for individual drugs in other studies. The device can therefore support large-scale parallel drug screening quickly and efficiently. However, the model cannot replicate any element of the TME (except for the tumour component itself). Consequently, the efficacy detected *in vitro* could be significantly different from the results achieved in patients.

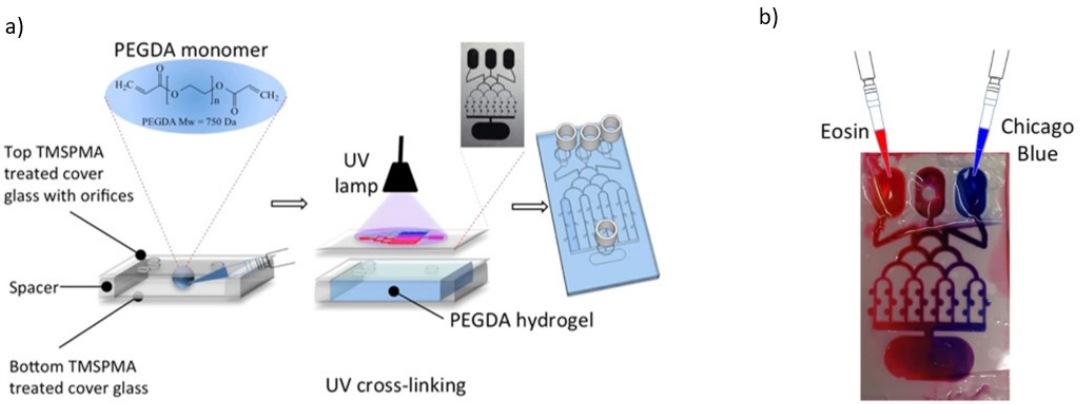


**Figure 10:** a) Fan's microfluidic chip manufacturing process. b) Qualitative analysis of mixing gradient in the channels. Adapted from Fan et al.[59]

## 3D Bioprinted Models

As described above, the structure of GBM is challenging to replicate as it includes both a highly heterogeneous three-dimensional structure and an intricate microvascular network. Microfluidic systems allow the vasculature to be easily mimicked and monitored, but they can not mimic the complex morphology and histology of the tumour. In contrast, *3D bioprinting* accurately recapitulates the GBM organization. 3D bioprinting is an additive manufacturing technique involving the layer-by-layer deposition of *bioinks* containing a cell suspension, possibly (but not necessarily) dispensed together with a supporting biomaterial. In the case of GBM, bioprinting solutions for acellularized scaffolds with subsequent *in vitro* seeding are not widespread in the literature due to poor reproducibility and difficult control over seeding [8]. The most commonly adopted technique is microextrusion bioprinting of scaffold-based bioinks. This biofabrication technology extrudes continuous filaments (direct write system) or droplets of cell-loaded hydrogels. The materials used are mainly alginate gels enriched with proteins characteristic of ECM, such as gelatin and fibrinogen [60] or collagen-I and hyaluronic acid [61]. Single cell populations can be used (typically U87-MG cells), or stem cell coculture systems can be developed (taking care not to induce differentiation due to the mechanical stresses introduced) [62]. However, realizing functional vessels and high-throughput systems is quite arduous.
Silvani et al. [46] merged these approaches to develop a 3D vascularized GBM on-chip model. The system combines an endothelialized microfluidic network (aimed at replicating the BBB) and a 3D printed GBM model. The custom microfluidic channels were manufactured through poly(dimethylsiloxane) replica moulding on a

photolithography-made SU-8 master. As shown in Figure 11i, the device consists of a central tissue chamber, a singular vascular channel, and two external perfusion channels. The compartments interact with each other through porous membranes by exchanging biochemical and mechanical signals.
The printing procedure takes place with a commercial device and follows a concentric pattern that recalls the geometry of the GBM. Moreover, two different hydrogels containing different cell populations were adopted to improve the biomimicry of the printed GBM-on-a-chip (figure 11iii). First, brain endothelial cells (hCMEC/D3) were encapsulated in a gelatin methacryloyl (GelMA)-fibroin bioink and printed in the intermediate region. The ring construct replicates endothelial tissue-specific functionality and tumour vasculogenesis. The core region is filled with GelMA-Alginate bioink loaded with GBM cells to mimic the characteristic TME. Furthermore, gel composition was optimized to match the properties of the tumour ECM without compromising printability and resolution. Although GBM cells are initially well confined and dispersed, they spontaneously aggregate into spheroids at the edges of the core in few days. This evidence confirms the similarity with tumorigenesis phenomena observed *in vivo*.
The lateral channels were functionalized with fibronectin to ensure the adhesion of an endothelial cell layer forming a BBB-like barrier. Both human umbilical vein endothelial cells (HUVECs) and human cerebral microvascular endothelial cell lines (hCMEC/D3) were employed. In both cases, vascular walls are formed with tight-junction protein zonula occludens-1 (ZO-1), characteristic of functional biological barriers. However, vascular permeability is significantly lower for hCMEC/D3, confirming that the use of such cells is better suited to replicate the BBB. Tight junctions were compromised in the following days, suggesting a biochemical interaction across the BBB and GBM-tumour boundary.
The authors also used the device to test the influence of gravity-driven mechanisms on GBM development. Recent experimental evidence has shown that variations in the gravity vector applied to the culture can modify the process of tumorigenesis and cellular activity. Data obtained with Random Position Machine confirm that the absence of gravity inhibits cell invasion.
Although the results obtained are similar to experimental observations collected *in vivo*, the model is currently incomplete. Integrating other cell populations (astrocytes and pericytes) would be necessary to develop a realistic BBB model. Moreover, no drug perfusion tests have yet been performed to assess the effective utility of this system. Finally, the dimensions of the vascular channel do not replicate those of the twisted tumour capillaries that surround GBM *in vivo*.

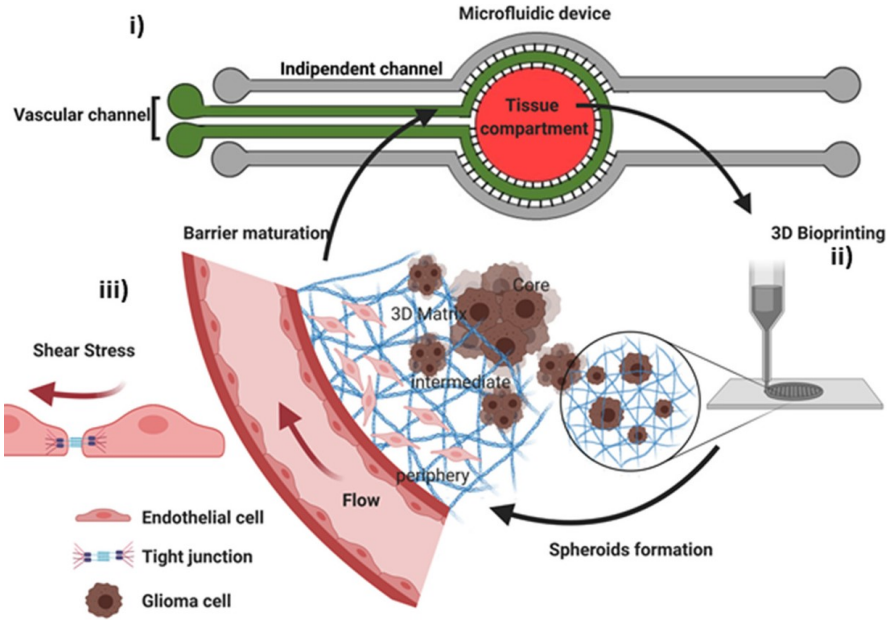


**Figure 11:** Sketch of the vascularized GBM-on-a-chip Silvani et al. i) The device structure includes a circular vascular channel (green) sourrounding the central tissue compartment (red) were the 3D tumour is housed.Two outer channels (grey) can be used for perfusion or drug delivery. ii) Representation of the 3D bioprinting procedure followed to achieve the concentric geometry characteristic of GBM. Structure of the interface between the endothelialized vascular channel (used to model the BBB and its tight junctions) and the central compartment. The latter contains a gel that mimics tumour ECM, promoting the formation of GBM spheroids (core), and an intermediate zone populated by endothelial cells. Image modified from [46].

# Aim of the work

This thesis project aims to develop a three-dimensional GBM model for the evaluation of nanocarrier- and cell-mediated drug delivery.
This study will asses GBM response to bortezomib (BTZ), a potent and selective proteasome inhibitor whose antitumoral activity has been widely demonstrated in clinical trials on myeloma patients. The ubiquitin-proteasome system controls cell growth and survival. In particular, the 26S proteasome avoids the accumulation of dysfunctional proteins produced in large quantities in tumour tissue [38]. BTZ inhibits this proteasome and reduces the degradation of polyubiquitinated proteins, whose presence limits cell proliferation and induces apoptosis.
The efficacy of the drug will be evaluated in a GBM model based on multicellular

spheroids obtained by growth under non-adherent conditions.Since high histological heterogeneity is one of GBM distinctive features, spheroids were made from differentiated human tumour cells (U87-MG) supported by human microglia cells (HMC-3) to replicate the interactions established in the TME between TAM and cancer cells. Glioblastoma-associated stem cells (GSCs) also play a pivotal role in tumour prognosis because they are responsible for GBM recurrence and radioresistance [21]. Since adding GSCs derived from human patients (GBM8) can enhance the complexity and realism of the three-dimensional model, multicellular spheroids will also be obtained with a mix of differentiated and GBM-tumour stem tumour cells. The considered tumour population will be composed of 10% GBM8 cells and the remainder of differentiated U87 cells. Tumour mix will also be integrated with microglial cells coculture in different percentages (30% and 50%). The drug will be tested on these different avascular tumour models to verify its efficacy and at the same time assess the role of the presence of other cell populations on treatment outcome.
Clinical studies have shown that BTZ fails to cross the healthy BBB and accumulates in amounts below the therapeutic threshold even in case of tumour-induced BBB impairment [63]. In addition, in the case of systemic administration, off-target accumulations with consequent side effects are frequent[29]. The use of nanocarriers for drug delivery may overcome these problems. However, it is necessary to evaluate how this mediated release affects the efficacy of the treatment [64].
In this work, NPs for drug delivery and encapsulation will be designed to posess a core-shell structure by the nanoprecipitation/self-assembly method. Nanoprecipitation is a simple synthesis method that allows the immediate formation of nanoparticles without applying intense mechanical efforts, yet scaling up is challenging. The main advantage is the ability to use non-toxic, water-miscible solvents. However, the need to combine miscibility in water with the ability to solubilize hydrophobic polymers limits solvent choices. Moreover, high concentrations of polymer and drug could hinder solvent displacement and promote aggregation phenomena. In addition, only hydrophobic drugs such as BTZ can be encapsulated in the polymeric core. Figure 12 shows the structure of the NPs produced, which include a bulk polyurethane structure for drug encapsulation and a lipid coating (to witch fluorescent markers can be added) to increase stability in suspension.

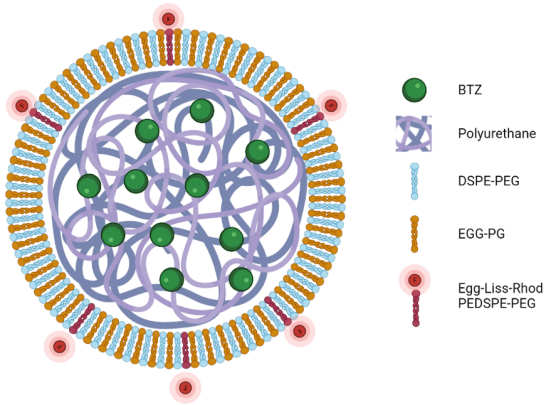


**Figure 12:** NPs structure and principal components. The polyurethane and BTZ (both soluble in acetonitrile but not in water) compose the nanoparticle core, while the lipids (DSPE-PEG and EGG-PG) form an external shell. Fluorophore-labelled Egg-Liss-Rhod PEDSPE-PEG is added in small quantities to track NPs. Created with Biorender.com.

Yield, encapsulation efficacy and drug release kinetics from NPs will be evaluated before testing the NPs on the GBM models to compare the efficacy of NPs-mediated treatment against free drug administration.
According to the literature, the nanoprecipitation technique produces monodisperse NPs with diameters below 200 nm[29], which may exploit the effect of Enhanced Permeability and Retention (EPR) in anticancer therapies. In fact, the fenestrated vasculature produced by tumour neoangiogenesis is particularly permeable to nanomaterials and therefore favours the accumulation of NPs in the tumour[64]. Furthermore, infiltrative GBM disrupts normal brain parenchyma and impairs the lymphatic system [21]. Therefore, the reduced lymphatic drainage promotes carrier retention within the tumour. However, the high selectivity of the BBB and the low permeability of brain capillaries limit the ability to extravasate to the tumour[65]. Since these NPs do not exhibit surface functionalization, they can only exploit passive targeting mechanisms by EPR effect.
The use of resident microglia as cellular transporters of NPs may solve these problems, as TAMs can transmigrate through the BBB and accumulate in the GBM following chemoattractants released from tumour cells[21]. Therefore, the ability of HMC3 cells to internalize NPs will be assessed to confirm the feasibility of this approach. The efficacy of cell-mediated BTZ release will be evaluated on the spheroid-based model. In addition, the cell penetration ability within the tumour will be analysed by inserting the spheroids into a biomimetic hydrogel, mimicking the tumour matrix.
As a key role in the progression and chemoresistance of GBM is played by the

cerebral microvasculature [46], the process of angiogenesis will be optimised using a commercial device. This device allows us to host model tissues, promotes the formation of a network of capillaries made up of human brain endothelial cells (HBEC-5i) and induces tissue perfusion. The structure and function of the obtained vessels will be studied, especially with regard to the presence of occluding junctions and by comparing the barrier effect with our previous *in vivo* observation.
In the end, we will optimize a vascularized GBM model to test the ability of cell-mediated transporters in improving systemic or local drug delivery to brain tumors.

# Chapter 1

# Materials and methods

## 1.1 Materials

For nanoparticles (NPs) preparation, a proprietary poly-caprolactone(PCL)-based polyurethane (NS-Hc2000) was used [66]. The polymer was synthesized using Poly($\epsilon$-caprolactone)-diol (2000 g/mol), n-BOC Serinol as chain extender, Dibutyl Dilaurate (DBTL) as catalyst, and 1,6 Hexamethylene diisocyanate (HDI), all purchased from Sigma Aldrich (Italy). The lipid shell of the NPs is composed of a mixture of L-$\alpha$- phosphatidylglycerol (Egg, Chicken) (sodium salt) (EGG-PG) and 1, 2-Distearoyl-sn-glycero-3-phosphoethanolamine-Poly (ethylene glycol) (DSPE-PEG), both purchased from Avanti® Polar Lipids. Fluorescent NPs were obtained by adding a fluorophore-labelled lipid, l-$\alpha$-phosphatidylethanolamine N-(lissamine-rhodamine B-sulfonyl) (Egg-Liss-Rhod PEDSPE-PEG, Avanti® Polar Lipids), to the shell.
Bortezomib (BTZ, Selleck Chemicals) was encapsulated within the polymeric core. All solvents were of analytical grade. All cells (except for Human glioblastoma cancer stem cells, CSCs) used in this work were grown in T75 flasks and split periodically (approximately every three days). Cells were incubated at 37 °C in a humidified atmosphere with a 5% $CO_2$ concentration. Trypsin (Gibco™) or Acutase (Gibco™) was used for cell detachment.
U87 MG (American Type Culture Collection, ATCC® HTB14™) or fluorescent U87 cells transfected with GFP (U87-GFP) were grown in Gibco™ minimal essential medium (MEM) supplemented with 10% fetal bovine serum (FBS, Gibco™), 1% penicillin/streptomycin.n (Gibco™).
Human microglia (HMC3, ATCC® CRL3304™) cell lines were grown in MEM supplemented with 10% FBS, 1% penicillin and 1% streptomycin.
CSCs, derived from Human Brain Cancer Tissue (GBM-8), were obtained by a collaborator (Houston Methodist Research Institute) and were cultured in Neurobasal

Media (Gibco™) supplemented with heparin (2 mg/ml), 0.2% B27, 0.5% N2, 20 ng/ml Fibroblast Growth Factor (FGF) and Epidermal growth factor (EGF) and 1.4% glutamine. All the supplements were purchased by Glibco™.
Human cerebral microvascular endothelial cells (HBEC5i, ATCC® CRL3245™, collected from the cerebral cortex) were cultured on T75 flasks coated with 0.1% Gelatin (ATCC® PCS-999-027™). 1.0 mL of gelatin was added to the flask, incubated at 37.0°C for about 45 minutes and then aspirated just before dispensing cells. The culture medium is PeproGrow™ MicroV Medium, consisting of Endothelial Cell Basal Medium with Growth Supplement-MicroV, both supplied by PeproTech®.
To allow for adequate vascularisation of the spheroid, MIMETAS OrganoPlate® Graft was used to obtain a vascularized GBM model. This commercial platform (shown in figure 1.1 presents 64 culture chips.

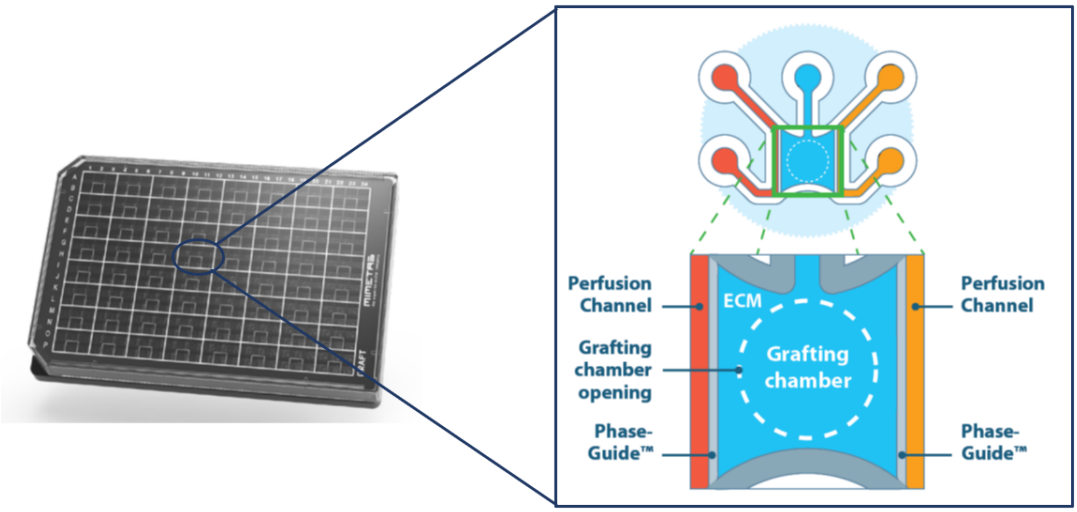


**Figure 1.1:** Layout of the MIMETAS OrganoPlate ® Graft Chip. Each unit has six wells: an inlet (upper) and outlet (lower) for each perfusion channel, a central open grafting chamber and an inlet for inserting the ECM gel. Inside the perfusion channels (in red and yellow) endothelial cells and eventual coating gels (e.g. gelatin, to facilitate adhesion) are inserted. The central chamber (blue) is filled with gel and can accommodate tissues or tumour models (e.g. spheroids).

Each chip includes an open graft chamber to house the tissue model, two perfusion channels mimicking the blood vessels, and a third channel to inject the ECM gel. The platform allows the development of a functional vascular network from endothelial cells seeded in the side channels, which can mimic the transport of nutrients and drugs occurring in tumours. Endothelial cells lining the channels migrate through the gel (which simulates ECM) to the spheroid and vascularize

it. The device does not contain membranes: the perfusion channels are formed by the same collagen-based ECM gel that constitutes the environment of the graft chamber, thanks to the use of a distinctive liquid handling technology based on meniscus pinning barriers (Phaseguides$^{TM}$). Perfusion does not require pumps, as the design ensures the flow of medium into channels and newly formed vessels by the simple action of a rocker shaker (OrganoFlow®).

## 1.2 Methods

### 1.2.1 Nanoparticles preparation

NS-Hc2000 was dissolved in acetonitrile (ACN) to produce a 10 mg/mL stock solution. The polymer was diluted to 1 mg/ml in 1 ml ACN and added dropwise to a solution of EGG-PG (200 µg) and DSPE-PEG (240 µg) in double-distilled water (dd$H_2O$ 2 mL) To obtain NPs, the lipid solution was maintained under stirring (250 rpm) at 60 °C to avoid the formation of micelles, followed by dropwise addition of the polymer solution in ACN to induce the spontaneous formation of nanoparticles. Finally, 1 mL of water was added dropwise to promote temperature reduction and solvent evaporation. The particle suspension was centrifuged using Amicon® Ultra centrifugal filter units (equipped with a 10 kDa cutoff-membrane) for 13 min at 3200 rpm and room temperature (RT). The particles were re-suspended in 1 mL of water or in culture medium for subsequent characterizations.
For drug loaded NPs, 50 µg of BTZ were added to the polymer solution in ACN. For fluorescent nanoparticles, 10 µg of Egg-Liss-Rhod PEDSPE-PEG were added to the lipid solution in water. Figure 1.2 schematically summarizes the steps of NPs synthesis. The yield of the process (%) was determined by freeze drying (LaboGene CoolSafe 4-15 L) the NPs suspension and by weighing the mass of the obtained NPs powder, according to the following equation (1.1):

$$Yield\,(\%) = \frac{weight\,of the\,formulation}{weight\,of the\,polymer + weight\,of\,the\,drug + weight\,of\,lipidic\,components} \cdot 100 \quad (1.1)$$

where:

- the weight of the formulation is the mass of NPs obtained at the end of a synthesis process (measured after freeze-drying);
- the weight of the polymer is the mass of NS-HC2000 initially placed in solution (1 mg);
- the weight of the drug of is the is the amount of BTZ added to the polymer solution (50 µg);
- the weight of the lipid components is defined by the sum of the weights of EGG-PG (200 µg) and DSPE-PEG (240 µg) present in the initial solution.

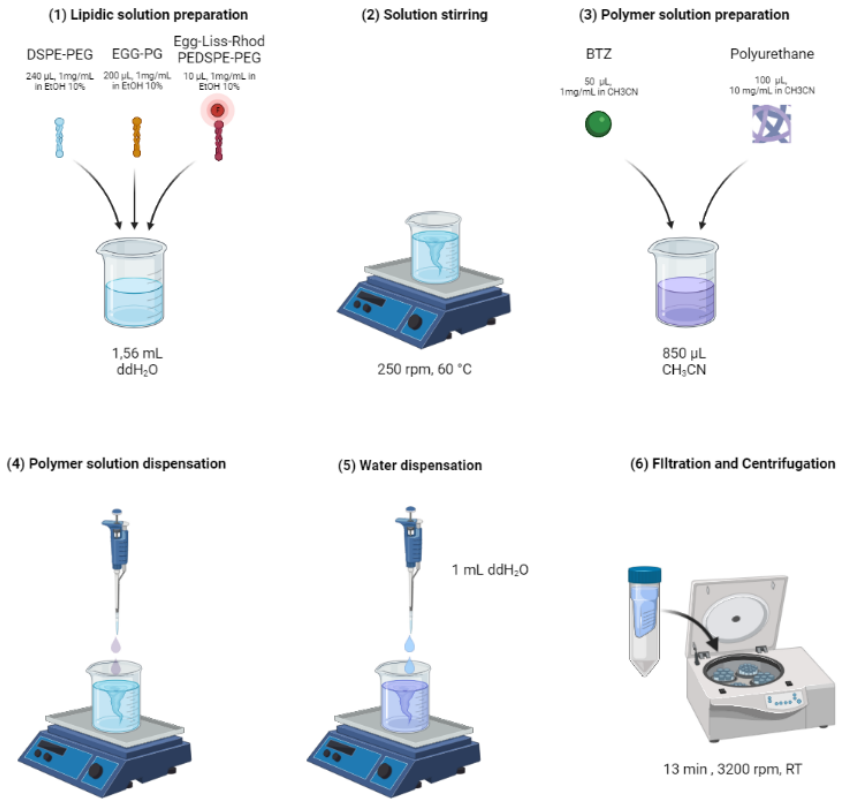


**Figure 1.2:** NPs synthesis protocol. Lipid solutions in 10% EtOH are dispersed in distilled water. The solution containing BTZ and the polymer in acetonitrile is added to the resulting solution drop by drop (at 60°C under stirring). The NPs are then collected in a filter by centrifugation at 3200 rpm (15 minutes). Illustration created with BioRender.com.

### Nanoparticles characterization

NPs were analyzed through Dynamic Light Scattering (DLS) to derive the hydrodynamic diameter and polydispersity. measurementSurface charge was also measured, using the dedicated Litesizer$^{TM}$ Omega cuvettes (polycarbonate case with gold electrode). These physical characterizations were performed using a Litesizer$^{TM}$ 500 (Anton Paar).
The evaluation of the *hydrodynamic diameter* is based on the empirical consideration that smaller particles move in suspension with a higher diffusion velocity.Over time, the instrument records the scattered light intensity after irradiating the NPs suspension with a He-Ne laser. The faster the particles move in solution, the greater the fluctuation of scatter intensities over time. The autocorrelation

function is used to define the NPs diffusion coefficient, which is related to the average hydrodynamic diameter through the Stokes-Einstein equation. However, the hydrodynamic diameter does not represent the actual NPs size since it corresponds to the diameter of a hypothetical sphere that diffuses in solution with the same velocity as the particle of interest. The solution characteristics, the core size, NPs shape and surface properties strongly influence this parameter.
DLS analysis returns a coefficient between 0 and 1 (called *polydispersity index*, PDI) that represents the uniformity of the diameter distribution. Hence, the smaller the PDI, the more the suspension is monodispersed.
As above-mentioned, the *zeta potential* is evaluated using specific omega cuvettes equipped with gold electrodes to apply a voltage difference to the suspension of NPs. The migration velocity of the particles between the electrodes is proportional to the zeta potential, i.e. the charge of the layer between particle and ions dispersed in the medium. The zeta potential is an index of the stability of the suspension. Therefore, the higher the absolute value (i.e. the net charge), the lower the risk of aggregation and the higher the suspension stability.

### Drug encapsulation and release

The *encapsulation efficiency* (%) was calculated for BTZ-NPs by using a by using a UV/VIS spectrophotometer (Lambda 365, Perkin Elmer®, Waltham, MA, USA) at 270 nm. Briefly, freeze-dried NPs were dissolved in 0.5 mL ACN to induce drug release and the amount of drug present in the NPs was assessed through an empiric calibration curve. The encapsulation efficiency (EE) was then determined from these data using the formula 1.2.

$$EE(\%) = \frac{Amount\ of drug\ in\ NPs}{Amount\ of\ drug\ supplied} \cdot 100 \tag{1.2}$$

where the amount of drug in NPs is the BTZ mass detected through UV/VIS spectroscopy, while the amount of drug supplied is the BTZ mass dissolved in the synthesis solution (50 µg for each NPs formulation). For drug release, BTZ-NPs were incubated at 37 °C in 1 mL dd$H_2O$. The amount of drug released was measured at different timepoints: 1 h, 3 h, followed by daily assessment up to 7 days. After each timepoint, the NPs suspension was centrifuged (Beckman Coulter Allegra X 30) at 10500 rpm for 15 min to isolate the NPs. The release solution was collected and freeze dried, while NPs were resuspended in 1 mL of fresh ddH2O. The released drug was measured by adding 0.5 mL of ACN to the freeze-dried release solution, followed by drug detection by UV-Vis.

### 1.2.2 Three-dimensional avascular model

#### 3D spheroid model development

Multicellular tumour spheroids (MTS) were obtained in ultra-low attachment U-bottom plates (Thermo Scientific™ Nunclon™ Sphera™ 96-Well, Nunclon Sphera-Treated, U-Shaped-Bottom Microplate) to provide an avascular three-dimensional GBM model. Different types of MTSs were prepared:

1. monoculture of primary tumour cells (U87);
2. coculture of tumour cells with different ratios of HMC3 (30% or 50%);
3. coculture of U87 and GBM8 (10%);
4. multi-culture of U87, HMC3 (30% or 50%) and 10% GBM8.

Figure 1.3 summarizes the main steps of the preparation protocol.

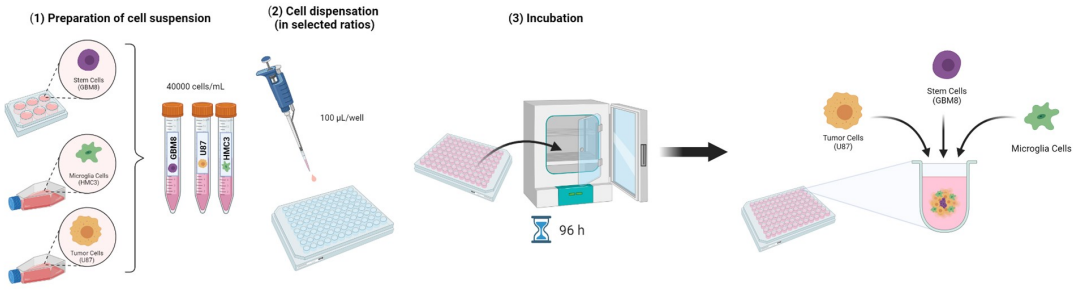


**Figure 1.3:** MTS preparation protocol. After preparing the cell suspensions at 40000 cells/ml, the various population mixes were plated, in the desired ratios, within a 96-well U-Shaped-Bottom plate and incubated for 4 days to complete the formation of MTS. Image crated with BioRender.com

Briefly, cells were plated at 4,000 cells/well and allowed to form spheroids for 4 days.

#### Pharmacological treatment

After the four-day incubation period, the spheroids were treated with free BTZ (2 nM, 10 nM, 20 nM, 50 nM). Controls (i.e., untreated MTS) were included in the experiment.
To evaluate the efficacy of NPs-mediated drug release, a formulation of NPs was dispersed in the culture medium to achieve a BTZ concentration of 20 nM and 50

nM. The same concentration of free BTZ was used for comparison.
Cell viability was assessed by the CellTiter-Glo® 3D Cell Viability Assay (Promega). This assay identifies the number of viable cells by quantifying the adenosine triphosphate (ATP) presence. The CellTiter-Glo® 3D Reagent contains a substrate (luciferin) and a lysis agent, which induce cell membrane rupture and ATP release. A thermostable luciferase (Ultra-Glo™ Recombinant Luciferase) acts on the substrate by consuming ATP and generates a luminescent signal, which is proportional to the amount of ATP released (indicator of cellular metabolic activity).
To determine viabilty, 100 µL of CellTiter-Glo® 3D Reagent were added to the wells containing cells (in 100 µL), The plate was allowed to equilibrate at room temperature, shaken (Biometra TSC ThermoShaker, Analytik Jena AG) protected away from light for 5 min at 460 rpm to induce cell lysis. The content of the wells was then transferred to a 96-well opaque white plate and briefly shaken until complete bubbles removal. Finally, the luminescence signal of each well was analysed by plate reader (Synergy™ HTX Multi-Mode Microplate Reader). Cell viability was expressed as a percentage of the luminescence value determined for untreated controls.
Since the ability to penetrate the tumour mass is another relevant element in assessing treatment efficacy, rhodamine-labelled fluorescent nanoparticles (Rhod-NPs) were administered to MTSs to track their distribution inside the spheroids. After 72 h of exposure to NPs, the spheroids were removed from the plate and washed twice in 250 µL of Phosphate Buffer Saline (PBS) for 5 min. Then, spheroids were immersed in 100 µL of 4% paraformaldehyde (PFA in PBS) fixative solution for 20 min. Subsequently, after fixative removal, spheroids were washed twice in PBS. The spheroids were embedded in Optimal Cutting Temperature (OCT) compound and frozen at -80 °C. Several spheroids of the same type were embedded in a single OCT cube of 1 cm side to facilitate the cutting procedure. The samples were cut using a Leica CM1860 UV cryostat (Leica Biosystems). Finally, the sections collected on glass slides were analysed with fluorescence microscopy (Nikon ECLIPSE Ti2).

### NPs internalization by microglia

The percentage of microglia that have successfully incorporated NPS, was determined by flow cytometry (FACS). Microglia were seeded in a 6-well plate at a density of 500·000 cells/well. Rhod-NPs were suspended in microglia culture medium to reach a concentration of 0.5 mg/mL. The NPs suspension was added to the wells containing cells and incubated for 2 h. Afterwards, the medium was removed and the cells were washed twice with PBS to remove uninternalized NPs. Cells were detached and collected, by centrifugation (5 min at 1500 rpm). The cell pellet was dispersed in 200 µL of PBS and analyzed in Guava® easyCyte™

Systemsflow Flow Cytometers (Luminex®) using the Yellow Fluorescence Protein Filter. Untreated cells were used as controls.
The percentage of nanoparticles that the cells have effectively encapsulated (cellular uptake) was quantified by plate reader. Microglia cells were seeded in 6-well plates at a density of 500·000 cells/well. Rhod-NPs formulation (0.5 mg/mL) were administered to the wells and incubated for 2 h. The medium containing the non internalized NPs was collected and the cells were rinsed in 500 µL of PBS (taking care to collect the supernatant with the washed-out NPs). Finally, cells were detached from the wells and dispersed in 1.2 mL of medium. Collected solutions (supernatant, PBS, and cell pellet) were transferred to a 96-well clear-bottom black plate (Thermo Scientific™). Synergy™ HTX Multi-Mode Microplate Reader was used to detect the fluorescence of each sample (using the characteristic excitation wavelength of 530 nm and emission wavelength at 590 nm of Rhodamine). The cellular uptake was calculated as the percentage fluorescence measured on the cell samples over the total fluorescence present in the well (PBS + supernatant + cell pellet).

### Evaluation of microglia-mediated NPs treatment efficacy

The efficacy of cell-mediated drug delivery was tested on monocultures of tumour spheroids. Spheroids of U87 cells (4000 cells/spheroid) were prepared in the Thermo Scientific™ Nunclon™ Sphera™ 96-Well, Nunclon Sphera-Treated, U-Shaped-Bottom Microplate, as described above. Microglia cells were seeded in 6-well plates at the density of 500·000 cells/well and treated with BTZ-NPs for 2 h (0.5 mg/mL) on day 4 after spheroid seeding. Microglia with internalized BTZ-NPs were rinsed, detached, counted, re-suspended in cell culture medium, and used to treat the U87 spheroids at different dilutions (500 cells/well, 1000 cells/well, 2000 cells/well, 3000 cells/well, and 4000 cells /well). Control wells were also included, by treating U87 spheroids with the same amount of microglia that had not internalized BTZ-NPs. The metabolic activity of the treated spheroids was evaluated by CellTiter-Glo® 3D Cell Viability Assay, according to the methods already described, for two time points (24 h, 48 h). To observe the distribution of microglia within tumour spheroids (i.e., the ability of the NPs to penetrate these tumor clusters), fluorescence microscopy coupled with microglia tracking was implemented. To this end, microglia were seeded in a 6-well plate at a density of 500·000 cells/well and incubated for 2 h with NPs (0.5 mg/mL). At the end of incubation, non-internalized NPs were rinsed away. Then, microglia cell membranes were labelled with lipophilic 1,1-Dioctadecyl-3,3,3-tetramethylindodicarbocyanine (DiD) dye. This tracer was selected because it has excitation frequency and emission that do not interfere with the fluorescence of GFP and rhodamine. A commercial tracer delivery solution (Invitrogen™ Vybrant™ DiD Cell-Labeling Solution) was adopted. The staining medium was prepared by

adding 5 µL of the DiD Cell-Labeling Solution solution to 1 mL of microglia growth medium. After removing the culture medium remaining in the well, 300 µL of this solution were added to each well, carefully shaking gently until the adherent cells were completely covered. Cells were incubated at 37 °C for 20 min until sufficiently homogeneous labelling was obtained. The staining solution was removed and the well was rinsed three times with culture medium for 10 min. Once the tracer was inserted the cells were detached and added to the spheroids in 100 µL of medium at different concentrations (1000, 2000 0 3000 cells/well). After 24 h, imaging was performed with NikonECLIPSE Ti2 inverted microscope.
To assess the ability of the microglia cell to penetrate the rigid tumour matrix and infiltrate within the GBM, spheroids of U87 cells have been embedded inside a commercial hydrogel, mimicking ECM (the VitroGel® Hydrogel System, TheWell Bioscience Inc.). The VitroGel 3D hydrogel solution was mixed with the VitroGel Dilution Solution (Type 1) at 1:5 volume ratios. The solution was then dispensed into the wells of a 96-well plate (100 µL/well), at 4 °C to avoid gel cross-linking. U87 spheroids were harvested from the U-bottom plate in approximately 25 µL of medium and inserted within the hydrogel in the sol phase. The hydrogel was then stabilized at 37 °C for 60 min, in a 5% $CO_2$ atmosphere. Meanwhile, microglia were seeded in 6-well plates at the density of 500·000 cells/well, treated with Rhod-NPs for 2 h (0.5 mg/mL) and stained with Invitrogen™ Vybrant™ DiD Cell-Labeling Solution. Microglia cells were added to each well (1000 cells/well and 20000 cells/well). Spheroids were observed through fluorescence microscopy to verify .their ability to infiltrate the ECM gel and reach the spheroid for the following 72 h.

### 1.2.3 Three-dimensional vascular model

#### Microvascular network development

MIMETAS OrganoPlate ® Graft Chip contains a tissue-housing well, side by blood vessel-like channels, from which angiogenesis can be induced towards the tissue graft. The ECM gel was prepared by mixing 1 M N-2-hydroxyethylpiperazine-N-2-ethane sulfonic acid (HEPES, Sigma) at pH 7.2-7.5 and sodium bicarbonate ($NaHCO_3$, Sigma) dissolved in sterile MilliQ water (37 g/L, pH 9.5) with Collagen-I (AMSbio Cultrex® 3D collagen I rat tail, 5 mg/mL) in a 1:1:8 ratio. For each chip, 4 µL of ECM gel were dispensed through the gel inlet until the graft chamber is completely filled. The plate was then placed in an incubator at 37 °C in a humidified atmosphere with a 5% $CO_2$ for 20 min to induce gel polymerization. Afterwards, 50 µL of Hanks' Balanced Salt Solution (HBSS, Sigma) were added to the gel inlet to keep the gel hydrated before cell seeding.
For cell seeding, HBEC5i suspended in medium and supplemented with 0.1% gelatin

in PBS (50:50 ratio, 10000 cells/µL) were added to each perfusion channel inlet (2 µL, 20000 cells/inlet). Additionally, 50 µL of medium were dispensed to the perfusion medium inlet. The plate was placed in static culture in an incubator (37 °C, 5% $CO_2$) for 24 h to permit cells attachment. Once the cells adhered, 50 µL of endothelial cell culture medium were added to the medium outlet and to the graft chamber.
The plate was then rocked on the OrganoFlow® (with a 14° inclination reversed every 8 min) in the incubator to promote homogeneous coverage of the channel with endothelial cells. Every two days, the medium was aspired from channel inlets and outlets and replaced. After approximately five days, when the cells were evenly distributed in the channels, angiogenic growth factors (listed in table 1.1) were administered from the graft chamber (50 µL per chip) to induce the formation of sprouts in the chamber. The growth factor cocktail was obtained by diluting the stocks in PeproGrow™ Endothelial Cell Basal Medium to the concentrations shown in table 1.1. Capillaries growth in the ECM gel was monitored at the microscope until a branched microvascular network was formed (after about 96 h).

| **Compound** | **Supplier** | **Stock** | **Concentration** |
|---|---|---|---|
| rhVEGF-165 | Peprotech | 100 µg/mL in 0.1% BSA[1] in PBS | 37.5 ng/mL |
| S1P | Sigma-Aldrich | 1 mM in 95% DMSO[2] 5% HCl 1M | 250 nM |
| PMA | Sigma-Aldrich | 10 g/mL 0.1% DMSO in MiliQ | 37.5 ng/mL |
| rhFGFb | Peprotech | 50 g/mL in 0.1% BSA in PBS | 37.5 ng/mL |
| rhMCP-1 | ImmunoTools | 100 g/mL in 0.1% BSA in PBS | 37.5 ng/mL |
| rhHGF | ImmunoTools | 100 g/mL in 0.1% BSA in PBS | 37.5 ng/mL |

**Table 1.1:** Growth factors needed to prepare the angiogenic cocktail. The concentrations in the last column refer to the final composition of the cocktail, obtained by diluting the various stocks in PeproGrow™ Endothelial Cell Basal Medium.

[1]Bovine serum albumin

[2]Dimethyl sulfoxide

### Immunostaining

The immunostaining protocol was optimized from the procedure suggested by MIMETAS. All incubation steps were performed under dynamic conditions using the OrganoFlow® with an inclination angle of 5° and a switching interval of 2 min. After having removed the medium from all chips, 50 µL of fixative solution (4% PFA in PBS, Alfa Aesar) were added to the graft chamber, inlets and outlets. The chip was washed for 5 min three times with 50 µL of PBS in the graft chamber, inlets and outlets. Cells were permeabilized for 10 min with 0.3% TritonX-100 in PBS (50 µL to each well). After another washing step, 50 µL of Thermo Scientific™ SuperBlock™ (PBS) Blocking Buffer were added to the graft chamber, inlets and outlets and incubated for 45 min. Primary antibodies were diluted at a ratio of 1:500 in the blocking buffer. Two Rabbit monoclonal antibodies were employed for this study, i.e. Recombinant Anti-ZO1 tight junction protein antibody (Abcam ab221547) and Recombinant Anti-CD31 antibody (Abcam ab76533). Once the blocking solution was removed, 20 µL of antibody solution were injected into each inlet/outlet and the graft chamber and incubated overnight at 4 °C. At the end of the incubation, the primary antibody was removed and the chip was rinsed three times with PBS. Subsequently, the secondary antibody Goat Anti-Rabbit IgG H&L (Alexa Fluor® 555) (Abcam ab150078) was prepared in blocking solution (1:200), dispensed to the chip (20 µL per well) and incubated for 2 h at room temperature in the dark. After three further washing steps (PBS), cells were stained with 4',6-Diamidino-2-Phenylindole (DAPI) by adding 50 µL to each well and incubating for 15 min. Finally, imaging was performed with Nikon ECLIPSE Ti2 inverted microscope. The images were processed using ImageJ software [67].

### Nanoparticles perfusion assay

Once the formation of the vessels with the correct morphology had been verified, the integrity of the capillaries was assessed by testing vessel permeability to rhodamine-labelled NPs (Rhod-NPs) and by comparing the results with those previously obtained in mice.
To achieve this, Rhod-NPs were centrifuged and redispersed in 1 mL of endothelial culture medium followed by the addition of µL of the suspension to the channel inlet. The plate was placed on OrganoFlow ® to induce perfusion in the vessels. The distribution of Rhod-NPs was observed by fluorescence microscopy using the Nikon ECLIPSE Ti2 inverted microscope.

### Spheroid placement

U87 tumour spheroids were placed inside the graft chamber once the microvascular network was formed. Spheroids were prepared following the protocol described in

Section 1.2.2. Before insertion, the medium was removed and replaced with fresh medium. PeproGrow$^{TM}$ MicroV Medium was dispensed into the lateral channels to maintain endothelial cells (50 µL in each channel inlet/outlet) while 50 µL of U87 culture medium was placed in the graft chamber. The spheroid was transferred using wide bore p200 pipette tips, trying to dispense only the spheroid with the least amount of medium possible. The plate was maintained in the OrganoFlow® (14° inclination, 8 min interval) in humidified atmosphere. The chip was monitored using Bio-Rad ZOE$^{TM}$ Fluorescent Cell Imager.
To enhance the integrity of the tumour spheroid, spheroids were ambedded in the VitroGel® Hydrogel System (TheWell Bioscience Inc.). The hydrogel was prepared according to the manufacturer's instructions, by first diluting the VitroGel 3D hydrogel solution with the provided Dilution Solution (Type 1) at 1:5 volume ratio, followed by mixing with the medium containing the spheroid (4:1 volume ratio). The gel-embedded spheroid was dispensed into the graft chamber, incubated statically for 60 min to allow complete gelation and placed back on the rocking plate.

### 1.2.4 Statistical analysis

Results are reported as mean±standard deviation. The size of the sample population (n) is specified in the corresponding section of the results. Statistical analysis was performed with GraphPad Prism software (GraphPad, San Diego, CA). T-Test analysis with a 95% confidence interval was used for comparisons.

# Chapter 2

# Results and Discussion

## 2.1 Nanoparticles characterization

With the nanoprecipitation method, NPs of small size and high yield were obtained for both empty NPs (yield 71±20%) and BTZ-loaded NPs (yield 74±19%) with no statistically significant differences. DLS analysis is shown in Figure 2.1a. As expected, BTZ encapsulation resulted in a slight increase in hydrodynamic diameter of the nanocarrier, which changed form 126±2 nm to 156±11 nm (p=0.0205). This size increase was also observed in other studies and is considered an indicator of successful encapsulation [68]. Both empty and drug loaded NPs possess the size range required for passive cancer targeting through the EPR effect (100–200 nm), as indicated by previous studies [64] [29]. However, this size range is not necessarily suitable to bypass the BBB, as studies have shown that NPs between 120 and 150 nm have very low rates of accumulation in the brain (often less than 1%) [65]. Other *in vitro* studies have shown that NPs with a diameter greater than 110 nm are less likely to leak from brain capillaries [69]. This is also in agreement with previous *in vivo* observations by our group, which demonstrated little or no extravasation of NPs through the brain capillaries after intravenous (IV) injection in live mice imaged by intravital microscopy (collaboration with the Houston Methodist Research Institute, unpublished data).
All NPs have low PDI which confirms that the obtained suspensions are monodisperse, with a slight increase (not significant) for the drug-loaded NPs, indicative of successful encapsulation as suggested by other authors [68] [70].
The zeta potential (figure 2.1b) ranged from -46±1 mV to -37±2 mV, which confirms NPs stability in suspension [71]. This represents another advantage since cells tend to internalize more easily negatively charged NPs by endocytosis[72]. The addition of BTZ resulted in a slightly higher zeta potential, which increased of about 10 mV (p=0.0041). This may be attributed to the presence of residual

drug in the outermost layers of the NPs. Although this variation is not commonly observed in other literature studies [68] [70], the zeta potential decrease may induce positive effects, as particles with a neutral or weakly negative charge have a longer half-life [64].

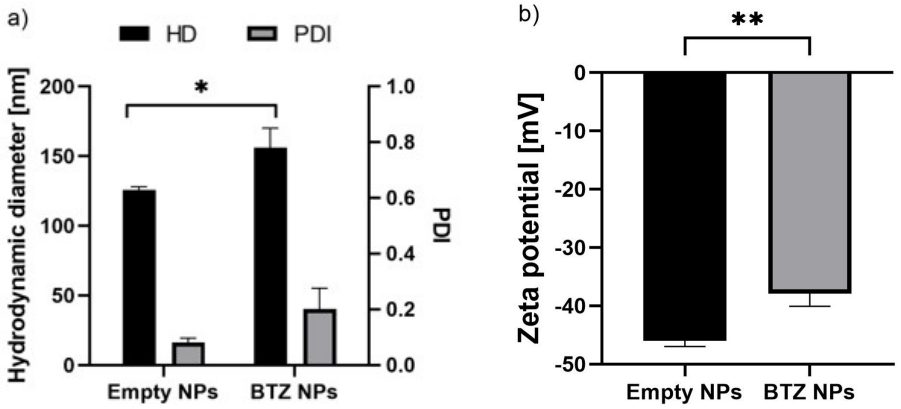


**Figure 2.1:** a) Hydrodynamic diameter (HD, left axis) and polydispersity index (PDI, right axis) of empty and BTZ-loaded nanoparticles (n=3). b) Zeta potential of empty and BTZ-loaded nanoparticles (n=3). * $p<0.05$, ** $p<0.01$

The encapsulation efficiency (EE) confirmed successful entrapment of BTZ, with an efficacy of 11±1.9%. The result is compatible with other studied which employed nanoprecipitation[70], but significantly lower than the EE achieved with other nanoparticles preparation techniques, such as polyelectrolyte complexation [68]. Drug release profile (figure 2.2) shows an initial burst release in the first 24 h, where more than 50% of the encapsulated drug was delivered, followed by a sustained release in the following days. At the 7-days timepoint about 80% of the encapsulated dose was released. The burst release seems to confirm that part of the drug is located near the surface of the NPs, thus causing an increase in the surface charge discussed above.

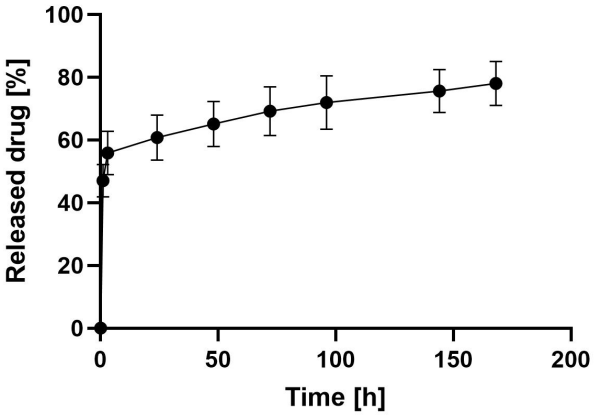


**Figure 2.2:** BTZ release from free NPs in water (n=3).

These results were obtained considering the release in water at physiological temperature. Hence, they do not perfectly replicate the physiological situation, where biological agents can degrade NPs and accelerate release [73]. Other studies of BTZ release from polymeric NPs produced by nanoprecipitation show much larger burst releases in the first 24 h (up to 80%) with a complete release in 5 days [70] [74]. Our results show that the hybrid polymer/lipid structure has a slower release rate of the drug with a more controlled burst effect, which may result in a prolonged release and reduced adverse effects[64].

## 2.2 Three-dimensional avascular model

### 2.2.1 Morphology of tumor spheroids

Monocellular spheroids, consisting entirely of human glioblastoma cells, and multicellular spheroids, containing microglia (HMC3) were successfully obtained as shown in figure 2.3. Since previous studies showed that about one-third of the cells present in the GBM are TAMs [21], we opted for two "biomimetic" spheroid compositions, where 50-70% of the cell population is composed by U87 and the remaining are microglia, even though microglia cells represent only a fraction of the TAMs present in the tumour microenvironment. Indeed, in addition to recruiting tissue-resident macrophages (i.e. microglia cells and peripheral brain macrophages), GBM also involves circulating immune cells such as monocytes [75]. As shown in figure 2.3b, microglia alone form small spheroids, while in combination with U87 (2.3c and d) the spheroids formed appear to have similar dimensions to those observed for monocultures of U87 cells (2.3a), regardless of the chosen ratio.

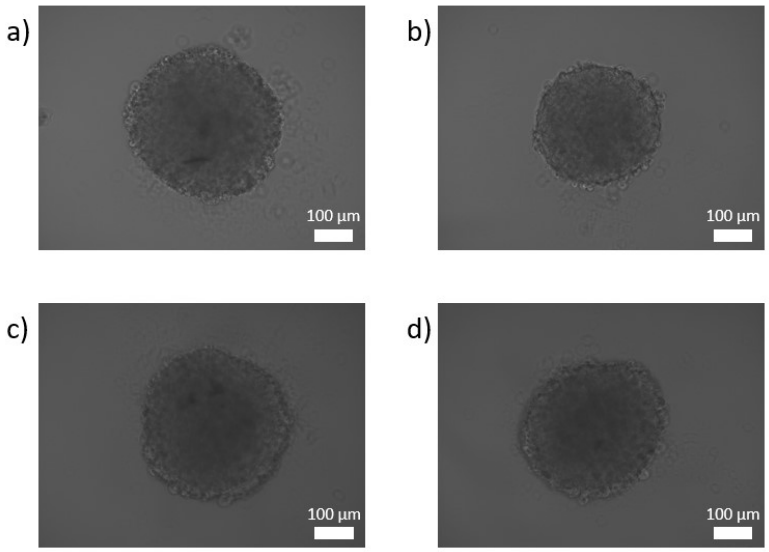


**Figure 2.3:** The images show the morphology of succesfully-formed spheroids. Single culture of tumour cells (U87, a) or microglial cells (HMC3 b) and coculture with 70:30 (c) or 50:50 (d) U87:HMC3 ratios were analyzed.

Subsequently, CSCs (GBM-8) were also included in the model in coculture with differentiated tumour cells alone or with the addition of microglia in a ratio of 30:70 or 50:50 to the whole tumor cell population (stem and differentiated) tumour cells. Figure 2.4 shows that the spheroids present darker areas characterized by high cell density located in the inner core. These areas correspond to clusters of stem cells that mimic tumour niches, as confirmed by fluorescence microscopy of GFP+ GBM8 (Fig. 2.5).

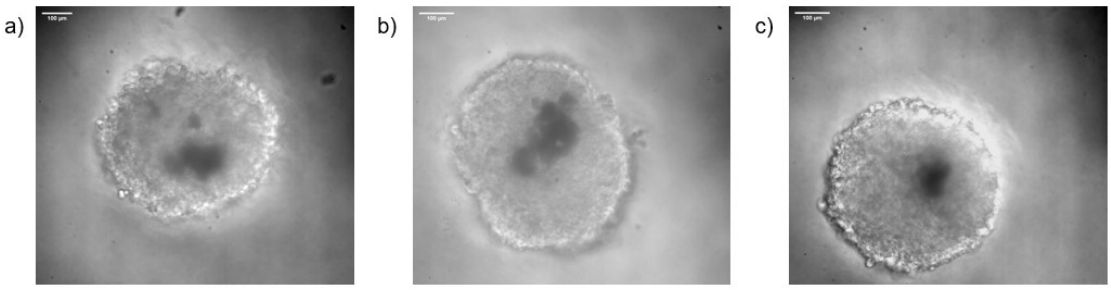


**Figure 2.4:** The three images show the morphology of spheroids at the end of the formation process. Co-culture conditions of tumor stem and differentiated cells alone (a) or with the addition of microglia cells in 70:30 (b) or 50:50 (c) ratios were analyzed. Scale bar: 100 µm.

Figure 2.5 shows that, regardless of the ratio of tumour cells to TAM, CSCs spontaneously position themselves in the central district of the coculture. This behaviour is similar to that observed *in vivo* [21]. When the microvasculature does not provide enough oxygen and nutrients (or it is not present, as in the model), GSCs reside primarily in niches near the necrotic core of the lesion [26].

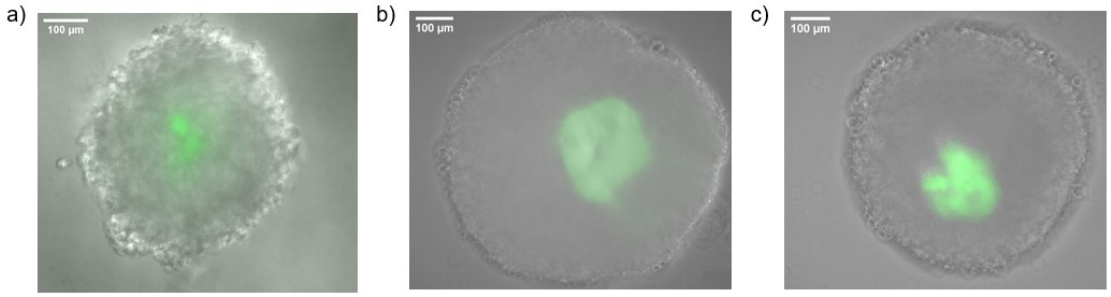


**Figure 2.5:** The three images show the distribution of GFP+ GBM8 cells (marked in green) within multicellular spheroids. Co-culture conditions include tumor stem and differentiated cells alone (a) or with the addition of microglia cells in 70:30 (b) or 50:50 (c) ratios. Scale bars: 100 µm.

### 2.2.2 Response of spheroids to pharmacological treatment with free BTZ

The antitumor efficacy of free BTZ was analyzed on monocellular spheroids, consisting entirely of differentiated cancer cells (U87), and multicellular spheroids, in which TAMs (HMC3) were also present in a 70:30 or 50:50 ratio (figure 2.6).
Previous studies have shown that microglia cells are sensitive to the action of BTZ [76]. In particular, *in vivo* tests to verify the activation of astrocytes and microglia by the drug have shown an increase in the activity of the former and a modest but significant decrease in that of the latter (assessed according to the expression of characteristic markers in the tissue) [77].

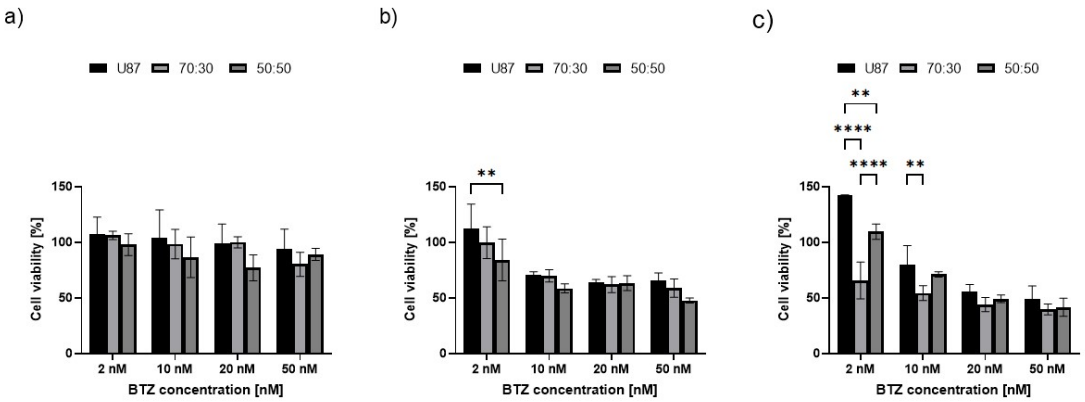


**Figure 2.6:** Viability assays performed after treatment with free BTZ, tested on monocellular tumour spheroids or multicellular spheroids containing 30% or 50% of microglia. Data were collected at three different time points: a) 24 h, b) 48 h, c) 72 h (n=3). Multiple comparisons were performed using two-way ANOVA. *p<0.05, **p<0.01, ***p<0.001, ****p<0.0001.

There were no significant differences between the viability detected in monoculture and coculture models for the higher concentrations of BTZ (20 nM and 50 nM). Figure 2.6 shows that the addition of microglia to the spheroid only affected cell viability at the lower dose (2 nM, and partly and 10 nM) and at the longest time point (72 h). For example, after 48 h the viability of the spheroids containing 50% microglia treated with 2 nM BTZ was around 85%, while for the other cases a higher viability than controls was observed (p=0.0081).
For spheroids composed only of U87, the viability does not vary significantly after 24 h, regardless of BTZ concentration. However, for higher concentrations, there is a relevant decrease in viability at 48 h and 72 h, suggesting an increasing drug action over time. On the other hand, subtherapeutic concentrations (2 nM) induce a progressive increase in cell activity.The same trend is observed in multicellular spheroid. For instance, for spheroids consisting of 50% microglia cells, at 72 h, the administration of BTZ 10 nm reduces the viability to 70% while, for treatments at a concentration 20 nM and 50 nM, the decrease reaches up to 49% and 41% respectively.
Previous viability data in 2D cultures showed a significant decrease in cell viability in co-cultures as compared to U87 alone[76]. It is presumable that tumour cells cultured in a 3D multi-cellular spheroid establish interactions with microglia that may exert a protective action. This crosstalk has been observed *in vivo*, where tumour cells release pro-inflammatory factors that change the polarization and signaling pathways of TAMs [21]. Figure 2.7 shows the morphology of the spheroids during the treatment period. For all spheroids, higher treatment duration and drug

doses seem to result in a less densely-packed structure.

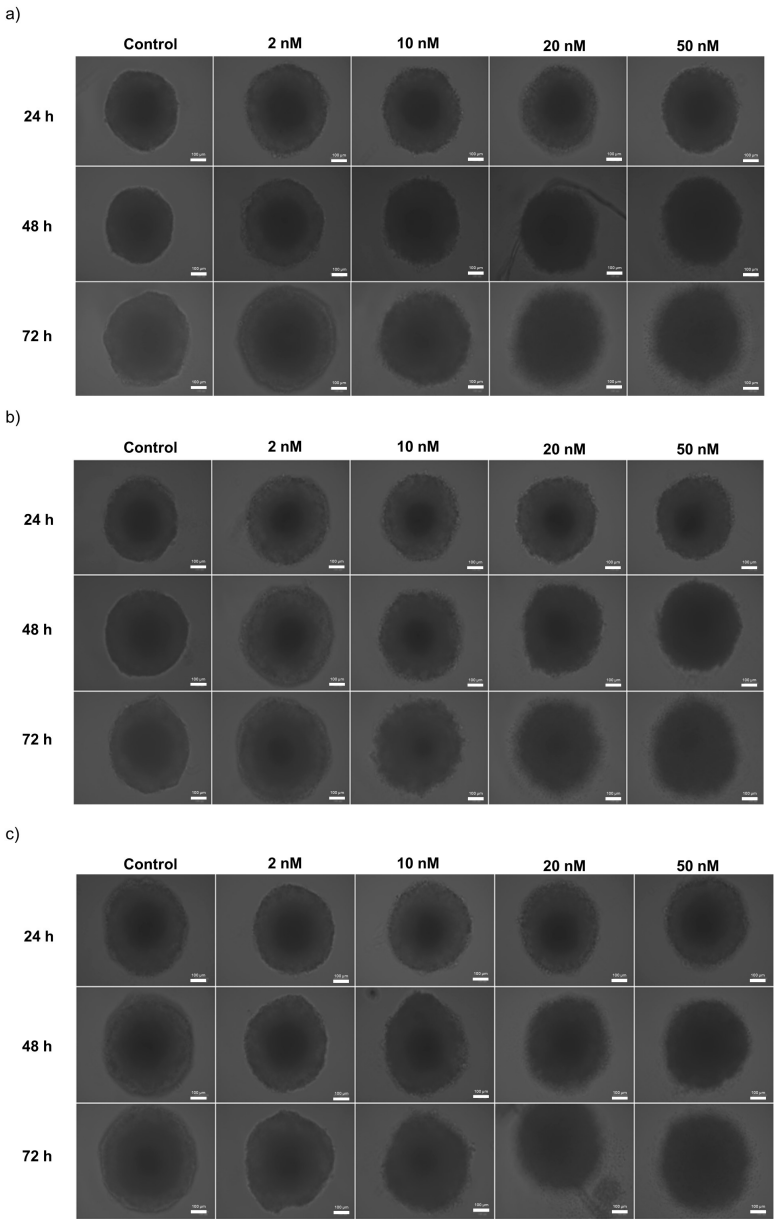


**Figure 2.7:** Images acquired in bright field microscopy for multicellular spheroids constituted differentiated tumor (U87) alone (a) or with the addition of microglia cells in 70:30 (b) or 50:50 (c) ratio. Scale bars: 100 µm.

### 2.2.3 Role of glioblastoma-associated stem cells

Figure 2.8a shows that the GSCs monoculture is extremely sensitive to the drug action already at 10 nM concentration after only 48 h. Moreover, higher concentrations (50 nM) lead to an almost complete absence of metabolic activity at 72 h. However, it is known that CSCs require supportive cells to survive and maintain their genotype *in vivo* [26].

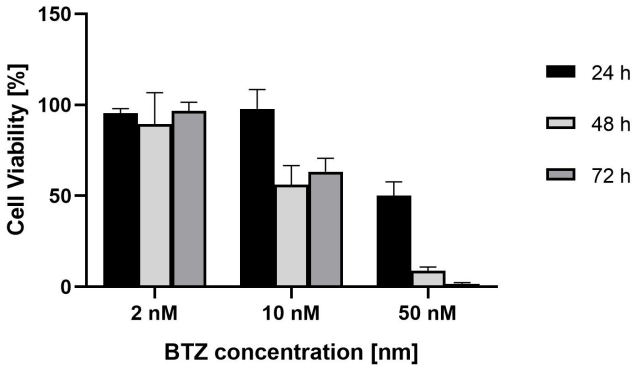


**Figure 2.8:** Viability assays at different time points after treatment with various concentrations of free BTZ on monocellular spheroids composed of GMB8 cells (n=3).

Our *in vitro* analysis confirms that GSCs chemoresistance depends on their interaction with the other cells in TME. Viability assays results (figure 2.9) on MTS containing stem and differentiated cells confirm that subtherapeutic concentrations (2 nM) are not effective against GBM but cause an increase in cellular activity. In the case of BTZ 10 nM, a significant decrease in viability was measured for MTS in the first 24 h (64%), followed by a constant or even higher viability in the 72h timepoint (up to 86%). In contrast, treatments with higher BTZ concentrations (20 nM and 50 nM) appear more promising in inhibiting cell proliferation in MTS.

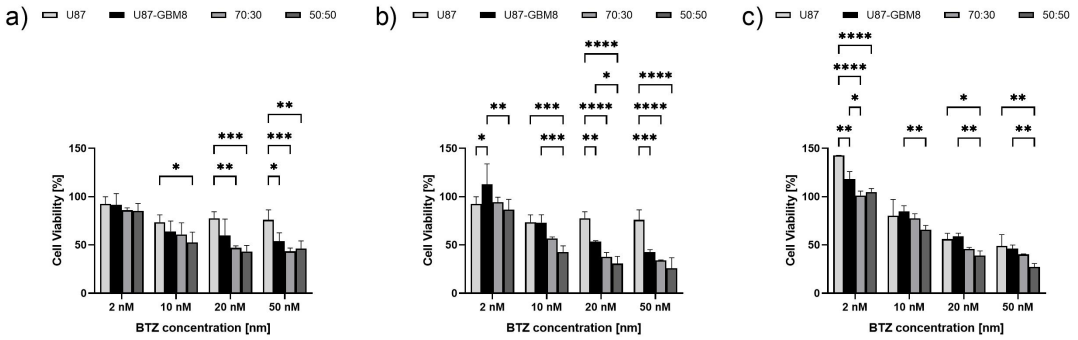


**Figure 2.9:** The graphs collect the viability assay results on monocultures of differentiated tumor cells (U87) and multicellular spheroids containing GSCs without (U87-GBM8) or with the addition of 30% (70:30 mix) or 50% (50:50 mix) microglia cells. Results were obtained on for different BTZ concentrations on three time points: a) 24 h, b) 48 h, c) 72 h. Multiple comparisons were performed using two-way ANOVA. *p<0.05, **p<0.01, ***p<0.001, ****p<0.0001.

In general, the presence of CSCs does not influence drug resistance, but seems to increase BTZ effect. One possible explanation is that GSCs promote chemoresistance and relapse on longer time scales than those considered in the study[78]. The *in vitro* model only partially replicates TME complexity and cell-cell interactions present in the GBM. The addition of growth[79] or pro-inflammatory factors[80] that induce *in vivo* gene activation of GSCs could improve the reliability in replicating GBM chemoresistance.
Figure 2.10 shows images acquired by brightfield microscopy for the three spheroid populations at each time point. Regardless of the treatment considered, there are no significant morphological alterations. In particular, the central zone of high cell density in which GBM8 reside preserve its geometry and localization. This evidence further confirms that interactions between stem and differentiated cells within the three-dimensional structure may have a protective effect on the former.

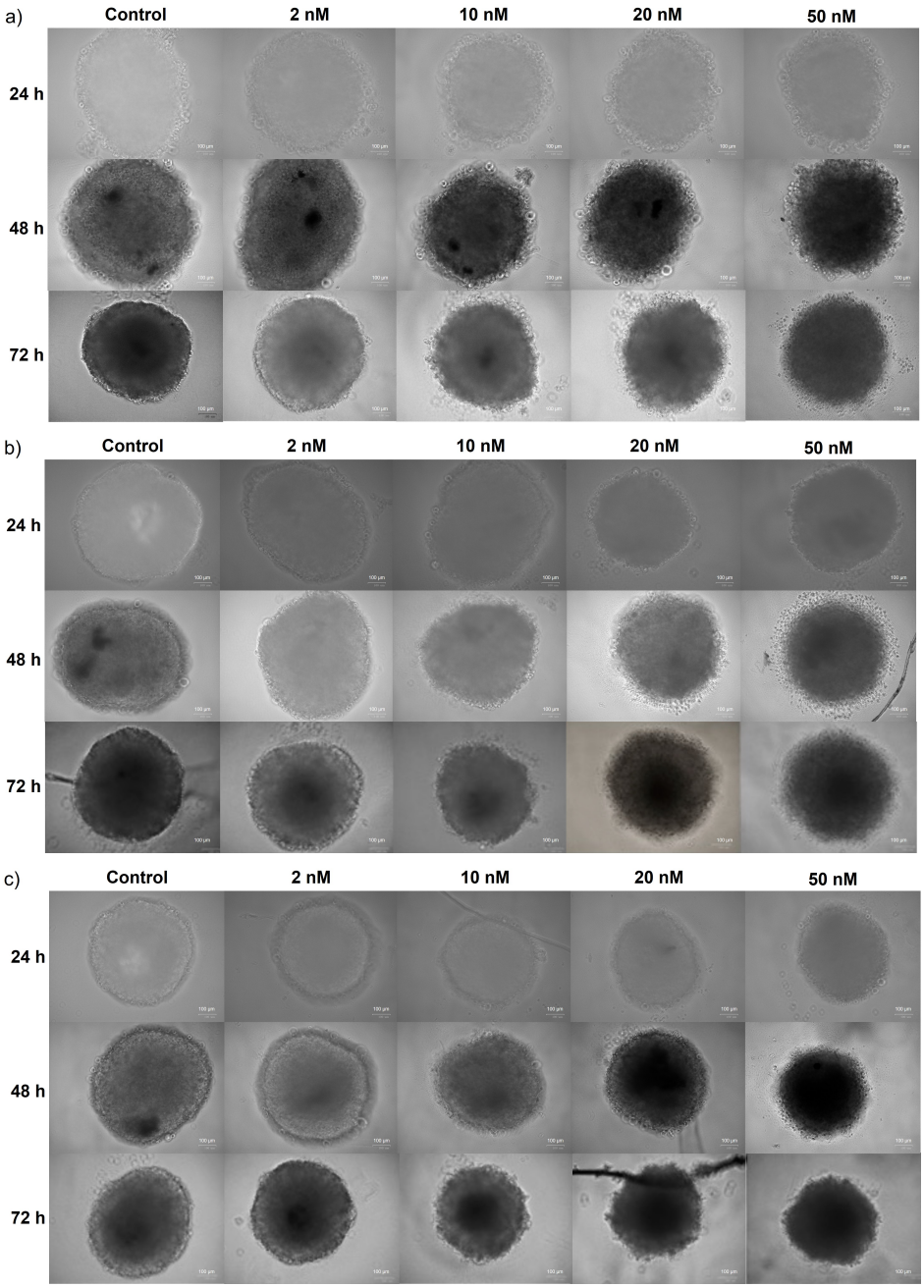


**Figure 2.10:** Images acquired in bright field microscopy for multicellular spheroids constituted by coculture of differentiated tumor (U87, 90%) and stem cells (GBM4, 10%). Spheroids were treated with different concentrations of BTZ (2 nM, 10 nM, 20 nM, and 50 nM) and observed at three different time points (24 h, 48, and 72 h). The tumor coculture was assessed alone (a) or with the addition of microglia cells in 70:30 (b) or 50:50 (c) ratio.

### 2.2.4 Nanoparticle-mediated drug delivery

Since efficacy of BTZ treatment is higher at 20 nM and 50 nM concentrations, BTZ-NPs containing this dose of BTZ were administered to spheroids obtained by tumour cells monoculture or coculture with microglia cells in 70:30 and 50:50 ratios. The concentration of BTZ within each suspension of NPs was estimated based on the encapsulation efficiency determined in section 2.1.

The viability results for treatment with BTZ-NPs were compared to those obtained by delivering equivalent free drug concentrations. Figure 2.11 shows that, for both concentrations and both time points, the decrease in viability is more pronounced for free drug treatments. The effect of BTZ-NPs seems delayed compared to that of the drug alone. This result is compatible with the fact that the release of the drug from the polymeric matrix occurs gradually (as confirmed by the release curve).

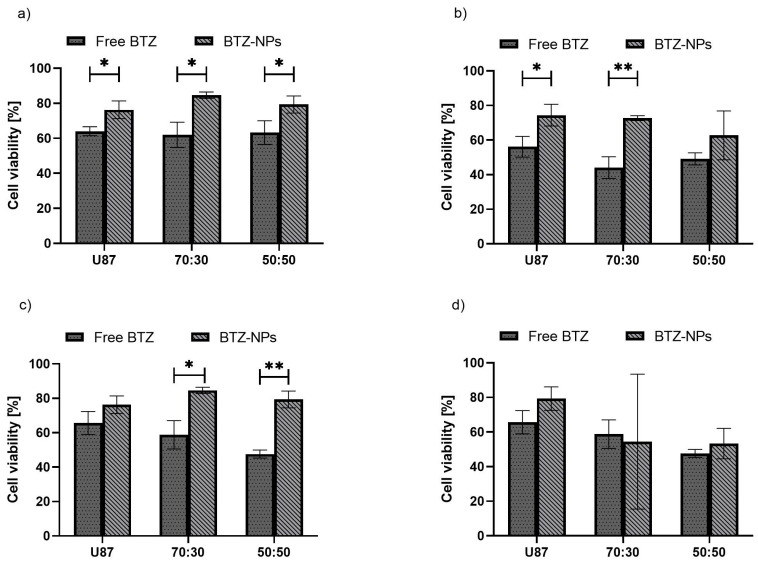


**Figure 2.11:** Viability assay results after the administration of free BTZ or BTZ-NPs. The tests involved monocultures of tumor cells (U87) and multicellular spheroids containing 30% (70:30 mix) or 50% (50:50 mix) of microglia cells. Results were obtained 48 h (a, c) or 72 h (b ,d) after the treatment with (free or encapsulated) BTZ concentrations of 20 nM (a, b) and 50 nM (c, d). Multiple comparisons were performed using two-way ANOVA. *$p<0.05$, **$p<0.01$.

If longer time points were considered, the effect of BTZ-NPs would continue to

grow and (presumably) persist longer than observed for the free drug. This controlled release over time could indicate a prolonged drug action and could allow the drug to cover larger areas of the tumour (as long as concentrations are maintained in the therapeutic efficacy range of the agent) [29]. It also avoids exceeding the threshold for systemic toxicity in the first moments after drug administration [81]. Figure 2.11 a,c show that after 48 h treatment with BTZ-NPs there is no significant difference in cell viability among the tested spheroids, regardless of their composition.
After 72 h, a concentration of BTZ-NPs equivalent to 50 nM results in higher cytotoxicity when microglia cells are present in the spheroid (although ANOVA analysis did not reveal statistically significant differences due to the high variability of some data). As shown in figure 2.11 d, the viability of spheroids consisting of 50% HMC3 is around 50%, compared to values higher than 70% measured for monoculture of U87. Probably, microglia cells (as macrophages) phagocyte NPs more easily, and are subsequently more exposed to the action of the drug. However, this difference does not emerge for the lower concentration of NPs. Moreover, in the case of monoculture of U87 cells, the action of the treatments is similar regardless of the concentration or time point considered.
Some results are highly affected by statistical variability. This problem stems from the fact that, beyond the estimates made, accurately determining the amount of drug effectively administered via NPs is challenging. In the case of free drug, the treatment medium is a homogeneous solution, and BTZ can be assumed uniformly distributed. Therefore, each well is subjected to (approximately) the same dose. In contrast, the drug in the suspension of NPs turns out to be *"quantized"*. Each nanocarrier contains a certain amount of BTZ (difficult to estimate), as shown by Figure 2.12. Hence, the "discretized" drug dose delivered cannot be adjusted with the same precision. The medium containing BTZ-NPs is also a suspension. Therefore, the assumption that the concentration is uniform at every point is less reliable. As a result, the volume of treatment suspension dispensed to the spheroids may not contain exactly the desired BTZ concentration, producing some variability in the results.

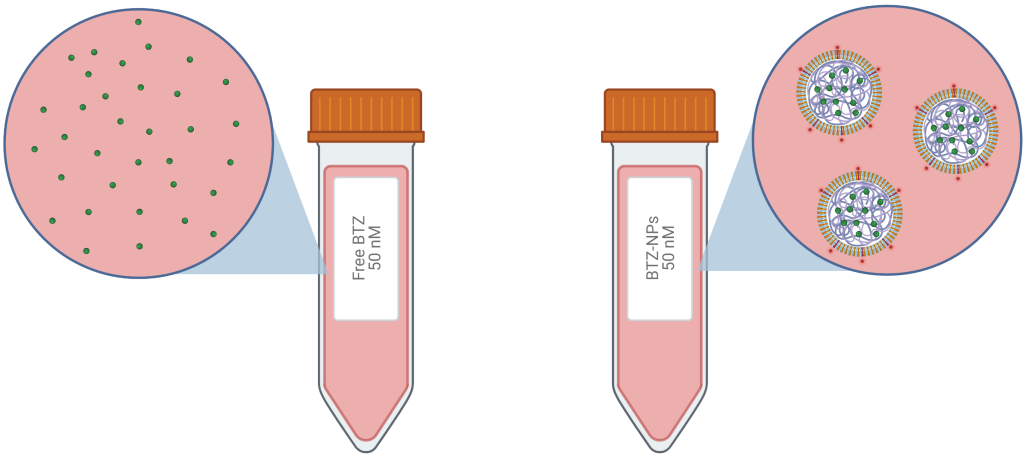


**Figure 2.12:** Different distribution of free and encapsulated drug in particles in the treatment medium. For the same BTZ concentration, the free drug is uniformly dispersed throughout the solution, whereas in the suspension of BTZ-NPs the agent is distributed in quantized clusters within the NPs. Created with Biorender.com.

To analyze how NPs localize within GBM spheroids, Rod-NPs were used to verify the ability of penetration within the spheroid and internalization by tumour cells. As shown in Figure 2.13a, fluorescence imaging confirms that the NPs (marked in red) located in the center of the U87 tumor spheroid and seem to be partly co-localized within U87 cells (nuclei marked in blue).
To confirm the co-localization of NPs within U87, spheroids containing GFP+ U87 (alone or in combination with microglia) were prepared, treated with Rod-NPs at a concentration similar to that used to achieve treatment with 50 nM BTZ and crysectioned. As shown in Figure 2.13b, after 72 h, the NPs penetrated the U87 spheroid to its innermost districts, confirming that NPs are valid drug transporters. Figure 2.13 c shows that NPs are less detectable in the multicellular spheroid, although they can be visualized in specific spheroid areas. It is possible that the phagocyte action of such microglia may reduce the ability of NPs to travel inside the spheroid, thus exerting a protective action on U87 cells, although further analysis og co-localization between NPs and microglia is needed to support this statement. Even in this instance, NPs have penetrated within the tumour spheroid (albeit unevenly).

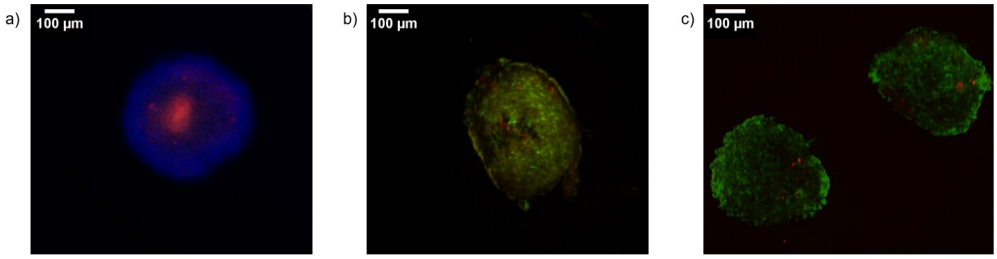


**Figure 2.13:** Images acquired in fluorescence microscopy for tumoral spheroids treated with Rod-NPs (in red) at a concentration equivalent to the one adopted for 50 nM BTZ after 72 h. a) Monocellular U87 spheroids with DAPI-labeled nuclei (blue). b) Section of U87-GFP cell spheroids (slice of 15 µm) c) Section of multicellular spheroids composed of 50% GFP-U87 cells and 50% HMC3 cells (slice of 15 µm). Scale bars:100 µm.

### 2.2.5 NPs internalization by microglia

Before using microglia as NPs transporters, we assessed the efficacy of NPs internalization by these cells. Since we aimed at transporting drug-loaded NPs which have shown a cytotoxic effect against this cell line, we opted for short incubation time (2h). Flow cytometry analysis (figure 2.14 a) showed a 3.1% internalization efficiency of Rhod-NPs, a results confirmed also by fluorescence, using DiD-labelled microglia cells (Figure 2.14b). This tracker can be directly introduced during adhesion culture to mark cell membranes (with stable fluorescence for more than 72 h).

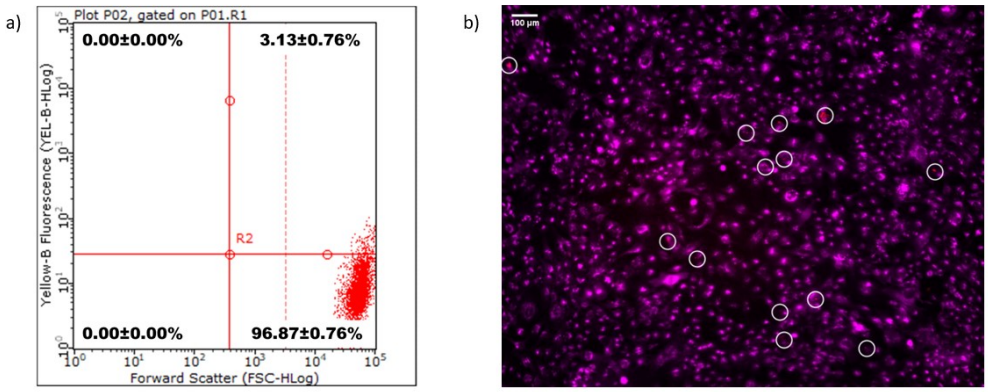


**Figure 2.14:** a) Quantification of cell internalization by flow cytometry. b) Internalization of Rhod-NPs by HMC3 microglia cells. Rhod-NPs appear in red, while cell membranes are stained with Vybrant$^{TM}$ DiD Cell-Labeling Solution (magenta). White circles highlight areas where Rhod-NPs internalized by microglial cells are visible. Scale bars: 100 µm

The low percentage of internalization is probably due to the choice of a short incubation time. However, the rate of internalization is not particularly different from that observed in the literature by incubating NPs and murine microglia cells for the same time [82]. This time point was selected based on BTZ toxicity tests performed on two-dimensional cultures of microglial cells. As suggested by the data collected in figure 2.15, even low drug concentrations induce significant declines in viability after only 24 h.

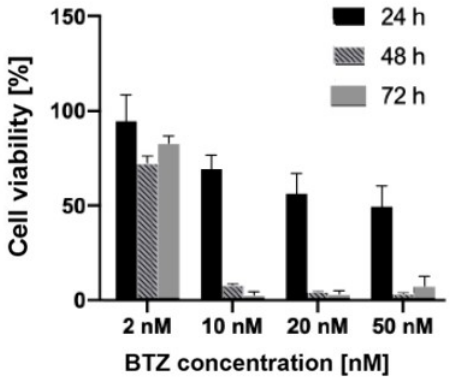


**Figure 2.15:** Results of viability assays performed at different time points after treatment with various concentrations of free BTZ on 2D cultures of HMC3 microglia cells (n=3). The data were collected in a previous study by the research team [76].

However, the internalization process could be optimized by identifying an intermediate treatment interval between 2 and 24 h that provides the best trade-off between uptake and viability. Alternatively, smaller amounts of NPs could be administered repeatedly over 24 h to increase the number of cells that internalize NPs without experiencing toxic effects. BTZ is an agent with a rapid action on cellular metabolism. However, other anticancer drugs, unable to cross the BBB, exert their effect (e.g., paclitaxel [83]). These drugs could then be encapsulated in NPs and internalized over longer periods, promoting better uptake by microglia without compromising their viability.

### 2.2.6 Evaluation of microglia-mediated NPs treatment efficacy

The therapeutic efficacy of cell-mediated delivery of chemotherapeutic agents depends on the ability of these transporters to internalize drug-loaded particles and infiltrate within the tumoral tissue [64]. Given the low percentage of internalized NPs, one might consider increasing the drug dose by administering higher concentrations of microglia cells. However, some preliminary tests with HMC3 that had internalized Rhod-NPs showed that adding a disproportionate number of microglia could lead to the formation of a "shell" around the spheroid. As illustrated in Figure 2.16a, this structure is separated from the spheroid itself and can easily disintegrate under even modest stresses. Moreover, Rhod-NPs remain mostly confined within this microglia cluster without reaching the tumour cells (Figure 2.16b). For this reason, in subsequent tests, the amount of HMC3 cells was never higher than the number of cells already present within the spheroid to favour the phenomena of invasion over those of aggregation between microglial cells around the spheroid.

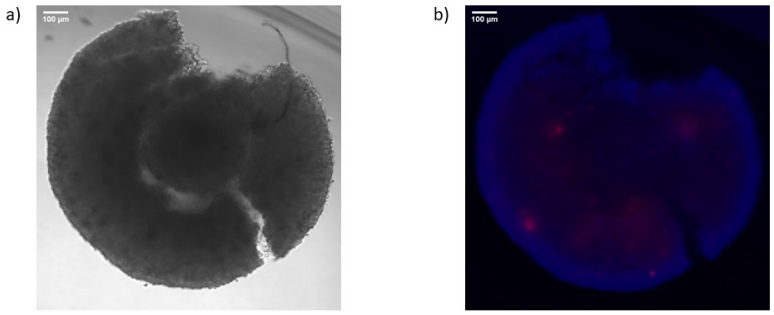


**Figure 2.16:** The two images show the effect of cell-mediated NPs-delivery on tumor spheroids performed by an oversized number of HMC3 cells (10,000 cells/spheroid). a) Spheroid morphology observed with bright-field microscopy. b) NPs distribution in the spheroid. Rhod-NPs appear in red, cell nuclei were stained with DAPI (blue). Scale bars: 100 µm.

The therapeutic efficacy of cell-mediated drug delivery was assessed by 24- and 48-h viability assays on U87 spheroids to which different amounts of BTZ-NPs-loaded HMC3 cells (figure 2.17)were added. For both time points, cell viability was calculated as the percentage ratio between the luminescence intensity measured on the treated sample (n=3) and the average luminescence detected on the sample, obtained by adding the same amount of microglia that had not internalized NPs (n=3). As shown in figure 2.17, no statistically significant differences were observed between the different treatments: in all cases, viability drops to around 90% after 24 h and to 70% after 48 h. Given how the controls in this experiment were defined, it is not possible to determine whether the drop in viability is attributable solely to microglia cells or involves tumour cells. However, at 48 h, the intensity of luminescence (an index of the amount of ATP in suspension) measured on spheroids containing only U87 is higher than that measured on all treated cell populations. Therefore, it is reasonable to assume that the decline in metabolic activity involves at least in part the tumour cells.

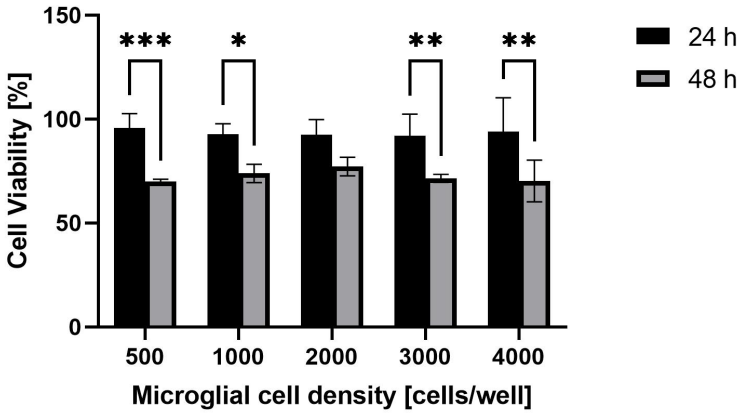


**Figure 2.17:** Viability assay results after the cell-mediated administration of BTZ-NPs. The tests involved monocellular spheroids of differentiated tumor cells (U87) treated with different quantities of microglial cells which have internalized BTZ-NPs for 2 h (n=4). Multiple comparisons were performed using two-way ANOVA. *$p<0.05$, **$p<0.01$,*** $p<0.001$.

Observation of the spheroids with bright field microscopy revealed that the treatment compromises the integrity of the structure. Figure 2.18 shows that, after 24 h, spheroid integrity decreases as the number of added HMC3 cells increases.

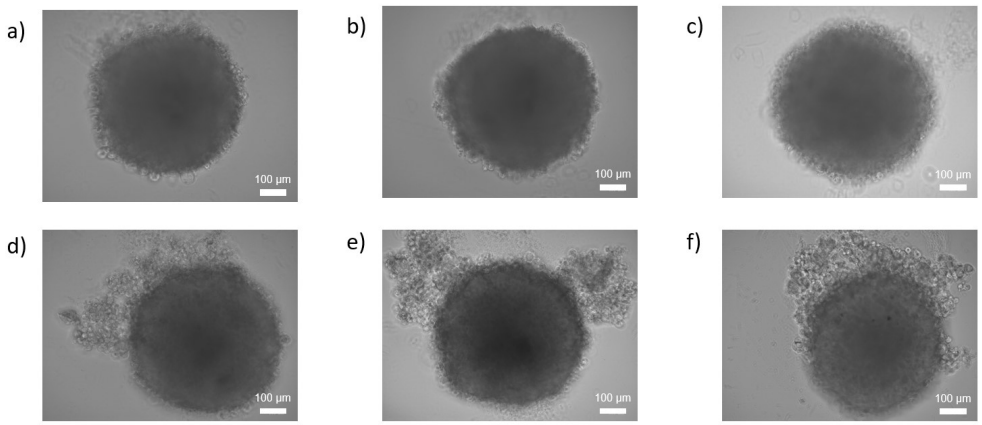


**Figure 2.18:** The bright-field images show U87 spheroids 24 h after different cell-mediated treatment with BTZ-NPs. a) Untreated U87 spheroid. b-f) U87 spheroid treated by adding 500 (b), 1000 (c), 2000 (d), 3000 (e) or 4000 (f) HMC3 cells. Scale bars: 100 µm

The effective penetration ability of microglial cells within the spheroid was monitored by marking the membrane of the microglia with Vybrant$^{TM}$ DiD Cell-Labeling Solution. Figure 2.19 shows that microglia cells appear to form clusters in the peripheral districts of the spheroid. However, a portion of the cells successfully migrates within the structure. The comparison between the images acquired for the spheroids to which 20000 cells/well (figure 2.19a) and 3000 cells/well were added (figure 2.19b) confirms that the number of infiltrating HMC3 increases whit higher seeding density.

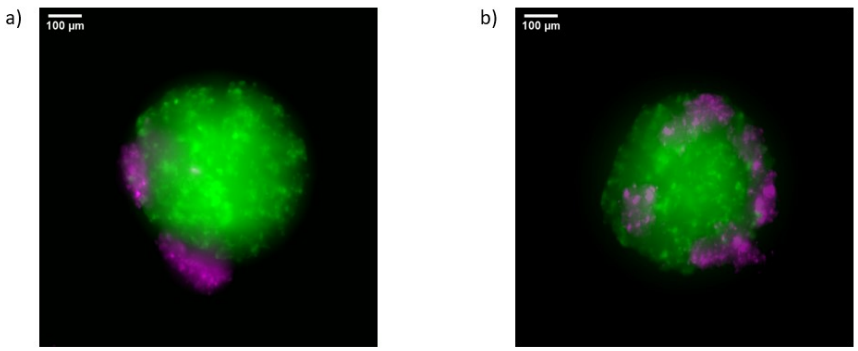


**Figure 2.19:** Infiltration of HMC3 microglial cells within U87- GFP spheroids after 24 h. HMCR3 membrane are stained with Vybrant$^{TM}$ DiD Cell-Labeling Solution and appear in magenta, while U87-GFP are labelled in green. 2000 (a) and 3000 (b) labeled cells were administered for each spheroid. Scale bars: 100 µm.

The infiltration pattern of microglial cells is not physiological, as it is influenced by the presence of nonadhesive surfaces. Furthermore, human GBMs are embedded in a rigid tumour matrix that hinders cell migration within the tissue. The adopted model does not replicate accurately enough the invasion mechanisms present *in vivo*. Consequently, the experiment was repeated by encapsulating the tumour spheroids in a commercial hydrogel. The VitroGel® Hydrogel System was selected due to its mechanical properties, similar to GBM ECM stiffness (0.1-10 kPa [8]). Moreover, experimental data suggest that hydrogel encapsulation may decrease the risk of spheroid disaggregation [84].
Tumour spheroids were embedded in the hydrogel, treated with DiD-labeled HMC3 cells, and monitored for 72 h to assess microglia migration within the gel. As is shown in Figure 2.20, at the same time point, the number of HMC3 cells located near the spheroid is greater when their seeding density is higher. Moreover, as time passes, microglia tend to migrate toward the tumour spheroid. This effect is particularly evident for spheroids to which 2000 cells were added. From 24 h to 72 h, there is a significant increase in HMC3 cells that emit a signal colocalized to the fluorescence of the U87-GFP spheroid.

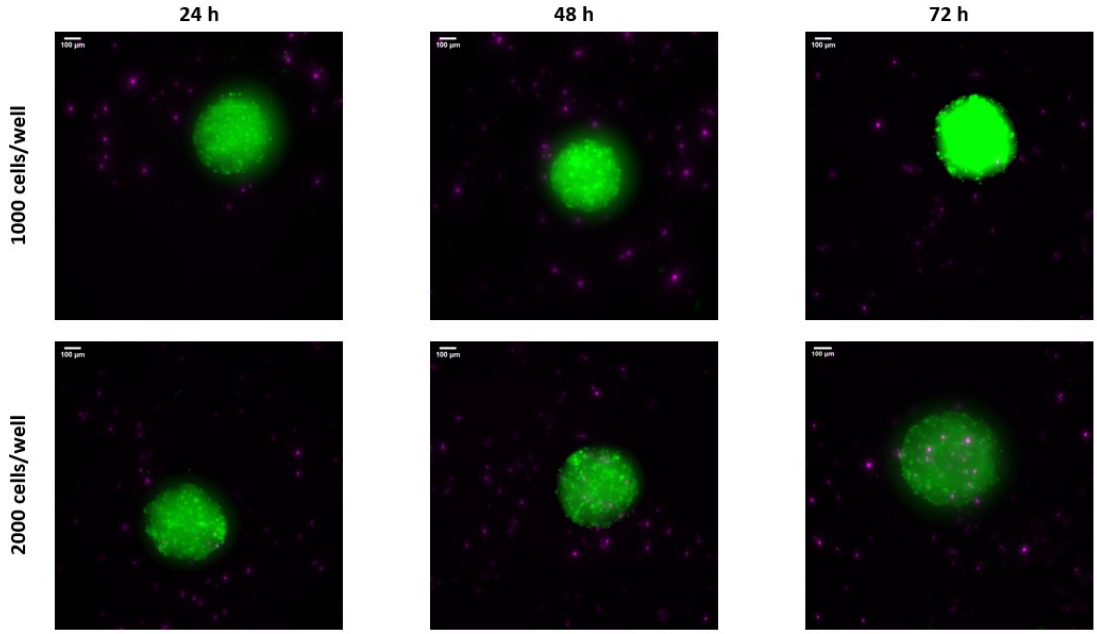


**Figure 2.20:** HMC3 microglial cells infiltration of within the VitroGel® Hydrogel. The gel houses U87-GFP spheroids, which are displayed in green. DiD-labelled HMCR3 membrane appear in magenta. The invasion process was monitored at three different time points (24 h, 48 h, 72 h) by administering cells in two concentrations (1000 cells/well and 2000 cells/well). Scale bars: 100 µm

To verify the effective penetration of the HMC3 cells within the spheroid, the Z-stacking functionality of the NIS-Elements Viewer software was used to reconstruct the structure projections at the points where co-localization of the fluorescence signals associated with the two populations was observed. As shown in Figure 2.21, when seeding 2000 cells/well, some microglia effectively infiltrate the spheroid. The number of infiltrated cells increases over time. In contrast, no infiltration was detected when seeding at a lower cell density (1000 cells/well).

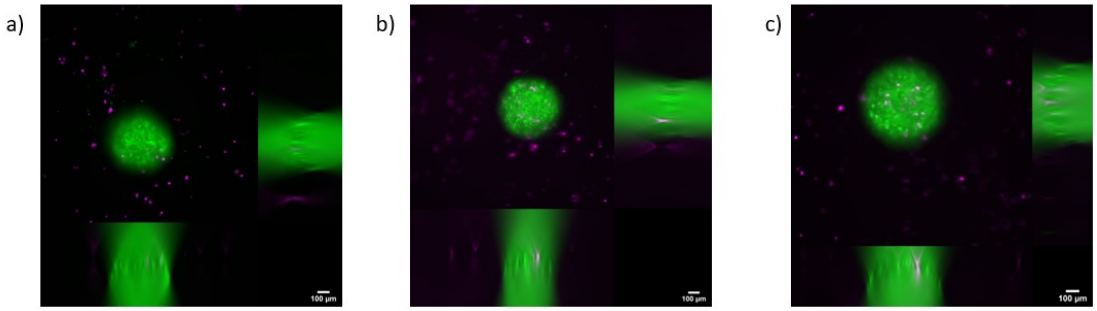


**Figure 2.21:** Reconstruction of lateral and frontal projections of the gel-embedded spheroids. U87-GFP spheroids are displayed in green. Infiltrating DiD-labelled HMC3 (2000 cells/well) appear in magenta. The invasion process was monitored at three different time points: a) 24 h, b) 48 h, c) 72 h) by administering cells in two concentrations

This experimental evidence confirms that microglia cells can migrate through the ECM-like gel and spontaneously accumulate in the vicinity of tumor cells, confirming the evidence observed in the literature on murine models [82]. HMC3s also appear to be able to infiltrate within the spheroid, confirming their potential utility as carriers to facilitate the accumulation of NPs within the GBM.
The results also confirm that the gel used maintains the stability of the tumour spheroids for at least 72 h.

## 2.3 Three-dimensional vascular model

A reliable GBM model must consider the presence of the tumour microvasculature and its interactions with cancer cells. Indeed, the presence of a capillary network makes it possible to evaluate *in vitro* the role of systemic administration on drug transport and to replicate the mechanisms of vascular tumour growth. Therefore, the model described so far can be improved by inducing vascularization of the spheroid using appropriate microfluidic devices [52].
Although most studies in the literature exploit Human Umbilical Vein Endothelial

Cells (HUVECs) because of their stability and high diffusion, vessels formed by these cells exhibit higher permeability than that of cerebral capillaries because of the absence of characteristic tight junctions [46]. Therefore, in this study, cells derived from the human cerebral microvascular endothelium were seeded inside the MIMETAS OrganoPlate ® Graft.
This microfluidic system may support high-throughput experiments, enabling parallel analyses on diverse conditions at a low cost. The commercial platform used contains numerous chips consisting of a central compartment, in which are located the perfusion channels and the graft chamber, three inlets, one for each channel and one for the graft chamber, and two perfusion outlets. A gel is inserted into the central compartment to house the tissue and confine endothelial cells seeding within the lateral channels while allowing the formation of angiogenic sprouts. Endothelial cells are seeded into the perfusion inlets to line the channels and mimic the native vessels of the tissue, from which the sprouts that will vascularize the model will form. The protocol provided by the manufacturers suggests starting the administration of the cocktail of pro-angiogenic factors four days after seeding on the ECM-like (to allow the complete formation of uniform walls sooner). The spheroid should be inserted into the graft chamber at the end of the capillary network development process to promote vascularization. However, standard protocols were defined using HUVEC cells. Consequently, preparation, seeding and culture procedures were iteratively optimized to achieve the formation of a functional vascular system.

### 2.3.1 Perfusion channel formation and coating

The ECM gel forms the walls of the lateral channel and should confine and support the adhesion of the endothelial cells. As shown in Figure 2.22a, in the absence of ECM-like gel, the cells invade the central chamber after seeding, as there is no barrier limiting their migration. Similar effects occur when gel filling is incomplete. Inserting a volume of 4 µL of collagen allows complete filling and physical separation between the vessel channels and the graft chamber. Hence, endothelial cells remain confined to the channels, as confirmed by figure 2.22b.

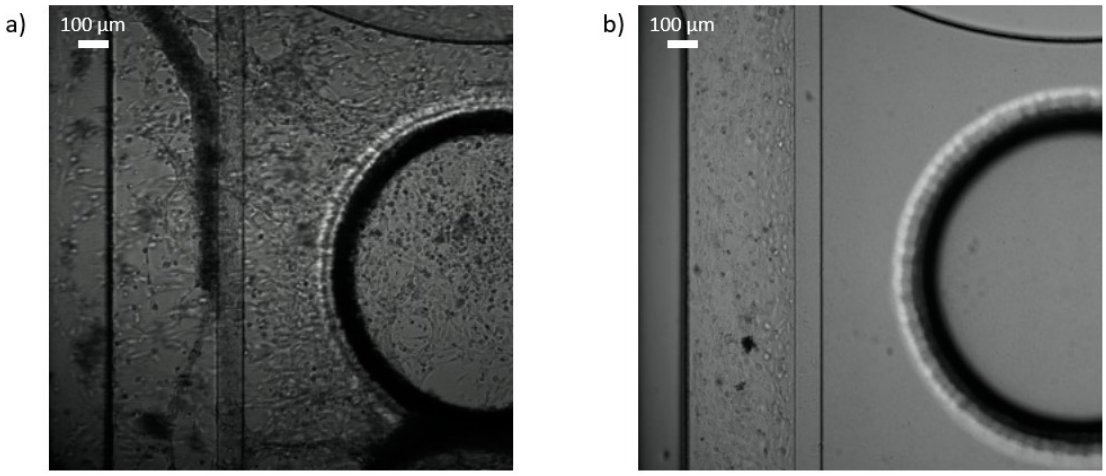


**Figure 2.22:** The bright-field images show the behavior of brain endothelial cells 24 h after seeding in the perfusion channels. a) Invasion of the graft chamber in the absence of collagen gel. b) Cell distribution in the presence of collagen gel.

The ECM gel not only forms the walls of the lateral channel and hinders cell migration, but it should also support cellular adhesion and proliferation. However, early tests showed that HBEC5i hardly adhere to the channels. Figure 2.23a shows that cell distribution is highly uneven: since cells can not adhere and spread on the walls, the cells aggregate in some districts. These channels, in addition to being inhomogeneous, are also unstable. Furthermore, the addition of growth factors into the graft chambers leads to detachment of endothelial cells from the channel walls and to their disordered migration of cells through the matrix without forming new vessels, as confirmed by figure 2.23b.
Since the lack of uniform adhesion is caused by the non-biomimetic composition of the adopted gel, it was decided to coat the channels with ECM-derived proteins. Specifically, 1% gelatin in PBS was used, the same coating adopted for two-dimensional flask cultures. MIMETAS suggests adding 40 µL of coating solution to each channel inlet before cell seeding. Nevertheless, our trials have shown that this protocol can easily lead to channel occlusion when using smaller volumes (2 µL, figure 2.24a).

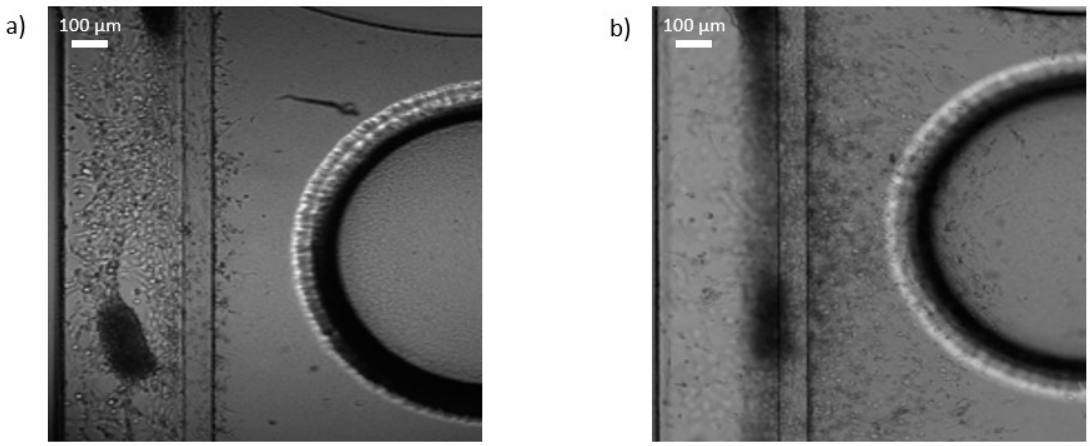


**Figure 2.23:** The bright-field images show consequences of direct seeding of HBEC5i cells onto collagen gel. a) Formation of cell aggregates and areas without cell adhesion at 4 days after seeding. b) Detachment of endothelium and invasion of the graft chamber following addition of growth factors (day 7).

The solution adopted to avoid this issue is simultaneously dispensing the coating solution and the cell suspension medium in a 50:50 volume ratio. Suspension and solution must be carefully mixed to disperse the cells and limit aggregation (figure 2.24b). The controlled working temperature ensures that the gelatin does not cross-link before seeding (after which there will be gel stabilization at 37 ° C).

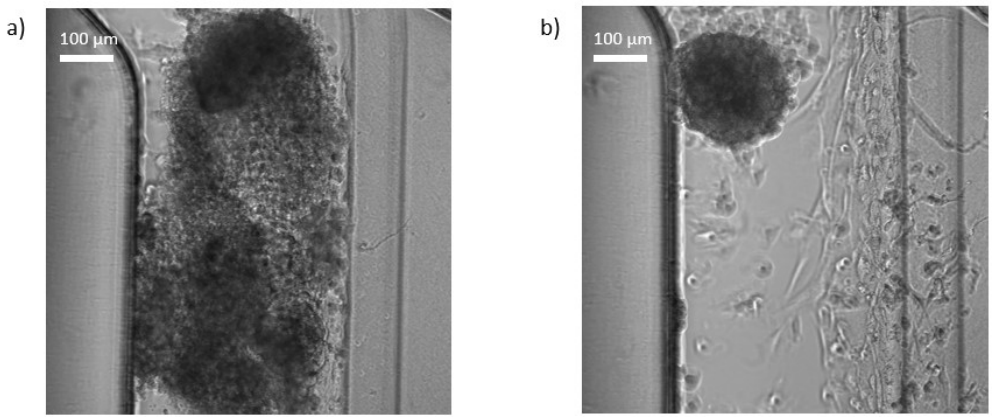


**Figure 2.24:** The bright-field images show defects detected during seeding of HBEC5i cells in case of incorrect channel coating. a) Occlusion of perfusion channels due to direct coating with gelatin. b) Formation of cell aggregates due to inadequate dispersion of cells in the gelatin and medium (50:50) solution.

This seeding method lead to the formation of a uniform endothelial cell coating within the canal. The endothelium appears complete about 4 days after cell seeding, as suggested by images acquired after 3 (figure 2.25a) and 5 days (figure 2.25b) of dynamic culture. In both cases, the vessel appears to be intact, and only a very small number of cells appear to have spontaneously begun migration to the graft chamber.

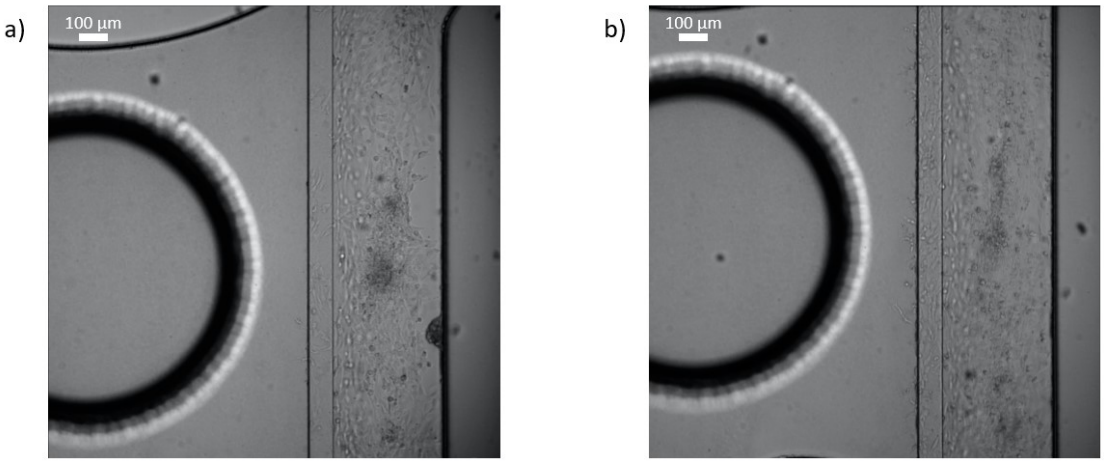


**Figure 2.25:** a) Bright field image of the perfusion channel 3 days after HBEC5i seeding. b) Bright field image of the perfusion channel 5 days after HBEC5i seeding.

Once the correct formation of the channel has been confirmed, it is essential to verify that the endothelial cells preserve the same structure and functionality manifested within the cerebral capillaries. Figure 2.26a shows an enlargement of the perfusion wall: endothelial cells preserve their morphology and are densely and homogeneously spread over the surface. Maintenance of cellular structures responsible for the barrier effect of vascular capillaries was verified by immunostaining for *cluster of differentiation 31* (CD31), a characteristic adhesion protein for platelets and endothelial cells [85]. As illustrated by Figure 2.26b, the CD31 protein staining confirms the formation of a vascular structure consisting of viable endothelial cells that have retained their native phenotype.
Immunostaining for *tight junction protein-1* ( or *zonula occludens-1 protein*, ZO-1) [86] (figure 2.26c) confirms the presence of tight junctions and the subsequent formation of a compact vascular structure that should be able to replicate the selective permeability of BBB capillaries and limit the extravasation of drugs and substances from the vessel.

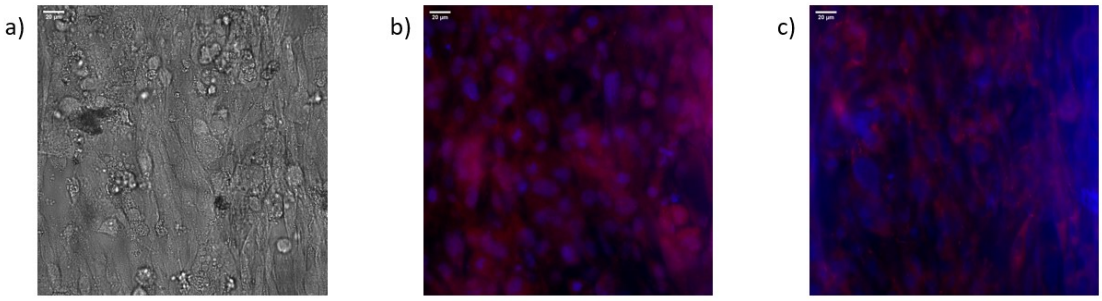


**Figure 2.26:** The figure shows images (60x magnification) of the endothelial cell channel seeded in the perfusion channel. a) Bright-field image of endothelial cells morphology and distribution. b) Confocal microcopy image. Endothelial cells have been labelled with Anti-CD31 antibody ( in red), while nuclei are stained with DAPI (in blue). c) Confocal microcopy image. The tight junctions of endothelial cells were stained with Anti-ZO1 antibody (in red), while the nuclei are labelled with DAPI (in blue).

### 2.3.2 Angiogenic sprouting

After endothelial cells seeding, maturation of perfusion channels requires approximately four days of dynamic culture. At the end of this phase, the proangiogenic growth factors required to form the microvascular network are introduced into the graft chamber.
The development of sprouts from the perfusion channel through the ECM gel was monitored at different time points. Figure 2.27 shows images acquired in bright field before factor administration and then 1 and 5 days later.The image acquired at day 0 shows that some cells migrate through the channel walls before administering growth factors. However, the phenomenon involves only few cells. The addition of the proangiogenic mix leads to the formation of new sprouts with a noticeable infiltration into the matrix after only 24 h. Five days after administration, the network of microchannels is significantly more widespread and reaches the tissue chamber.

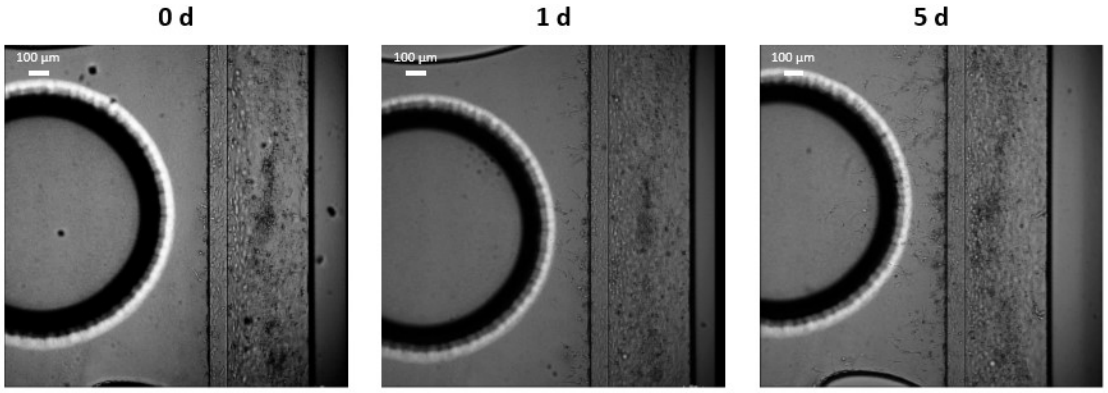


**Figure 2.27:** Development of the microvascular network following growth factor administration. Bright-field images represent capillaries before administration of growth factors (0 d), the day after addition of proangiogenic cocktail (1 d), and after five days of culture (5 d).

The gelatin coating does not seem to hinder the formation of new vessels. As demonstrated in Figure 2.28a, the microvascular network departs from the central perfusion channel and diffusely penetrates the gel. It is also possible to observe branching phenomena of the capillaries as one moves away from the vessel of origin, as occurs in the processes of angiogenesis *in vivo* (Figure 2.28b). The magnification in Figure 2.28c shows detail with the morphology of endothelial cells in sprouts. The gelatin coating contributes to preserving the integrity of the main vessel even in the presence of proangiogenic factors.
The magnification of the vessel wall shown in Figure 2.28d confirms that, even after administration, the cells in the wall remain homogeneously adhered even a week after exposure to the factors, despite the initiation of sprouting processes.

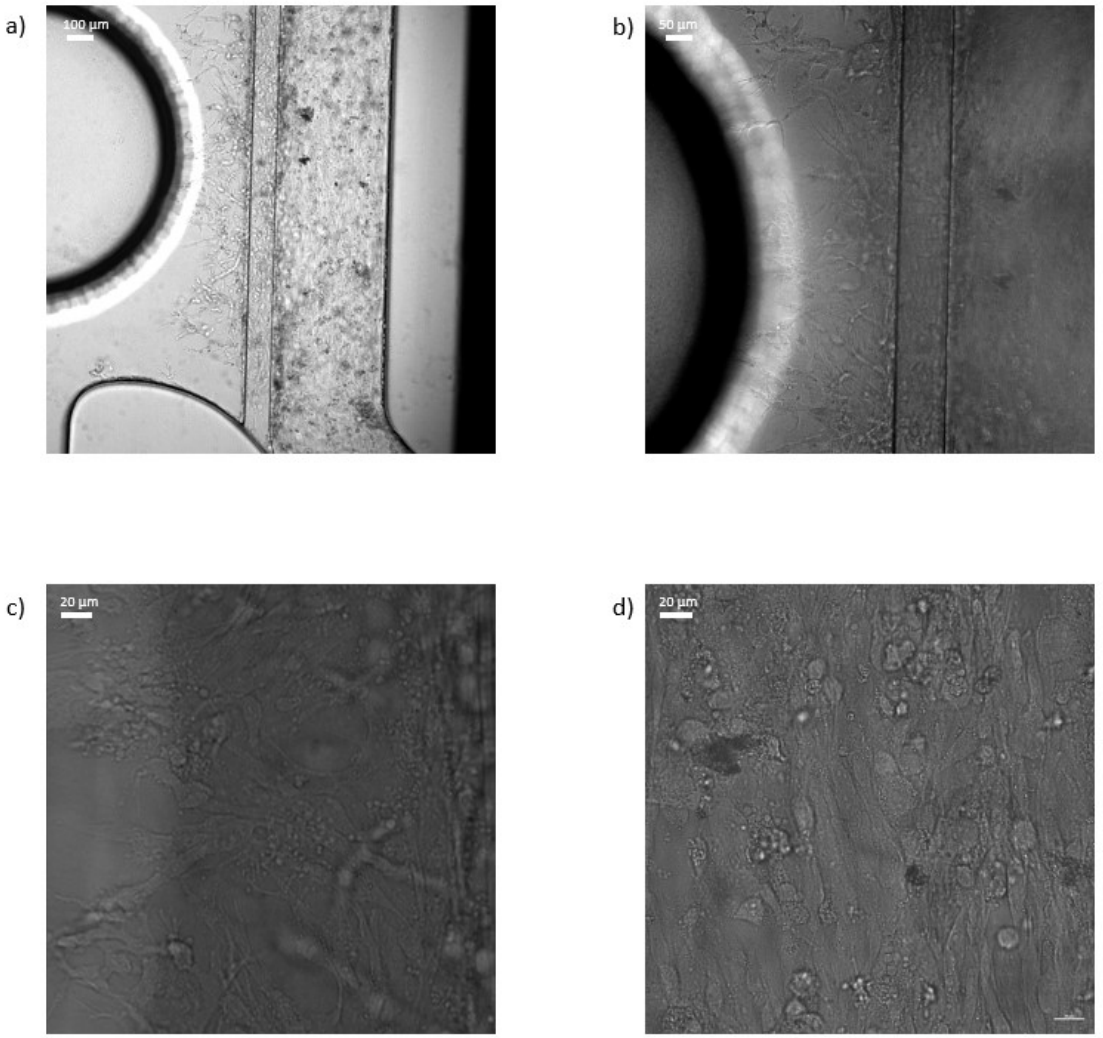


**Figure 2.28:** The bright-field images show the development of vessels 7 days after the administration of growth factors. a) Overall view of the channel and angiogenic sprouts. b) 20x magnification of the newly formed vascular network. c) 60x magnification of the newly formed vascular network. d) 60x magnification of the perfusion channel.

Immunostaining assessed the expression of CD31 and ZO-1 proteins in the newly formed vessels to better visualize morphology and verify the formation of tight junctions, characteristic of brain microvasculature. Staining with anti-CD31 antibody confirm that, 7 days after administration of the factor mix, cells maintain the endothelial phenotype and form a complex, branched network (2.29 a). Figure 2.29b shows that occluding junctions are also present within the newly formed capillaries, which consequently should be able to replicate the barrier effect of

human cellular endothelium[46]. Performing perfusion tests with probe molecules (e.g., Fluorescein Isothiocyanate-Dextran [87]) will be needed to verify this aspect. The assay should validate the vessel wall functionality and compare the permeability of the model with the data observed *in vivo*.

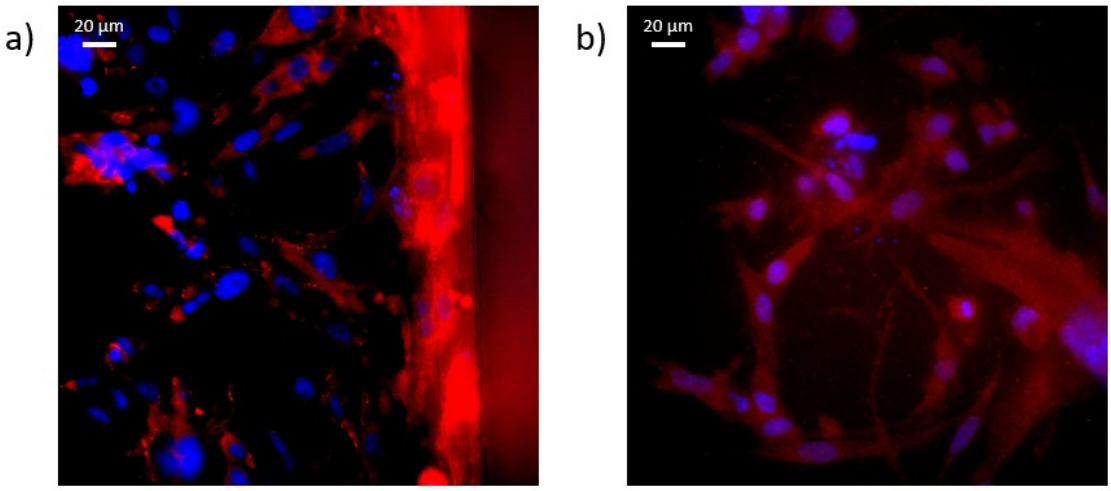


**Figure 2.29:** The confocal microcopy images (60x magnification) show the newly formed capillaries 7 days after the administration of the proangiogenic growth factors. a) Endothelial cells have been labelled with Anti-CD31 antibody (in red), while nuclei are stained with DAPI (in blue). b) The tight junctions of endothelial cells were stained with Anti-ZO1 antibody (in red), while the nuclei are labelled with DAPI (in blue).

### 2.3.3 Nanoparticles perfusion assay

Initial verification of the permeability of the obtained vessels was performed using Rhod-NPs injected into the vascular network model through the inlets of the cellular perfusion channels. Previous tests by the Houston Methodist Research Institute demonstrated the inability of IV-injected NPs pass through the brain endothelial barrier. Mice cerebral vessels were visualized in real-time with intravital microscopy to study NPs diffusion after intravenous injection. The results showed that NPs persist in cerebral microcirculation without accumulating at the level of the vascular endothelium and no signs of accumulation in the brain parenchyma. The perfusion assays on the model (figure 2.30) illustrate that Rhod-NPs remain confined within the channel without diffusing through capillaries (coherent with *in vivo* studies)[65]. The wall of the perfusion channel is intact, and the microvascular network is composed of vessels with compact structure and no fenestrations.

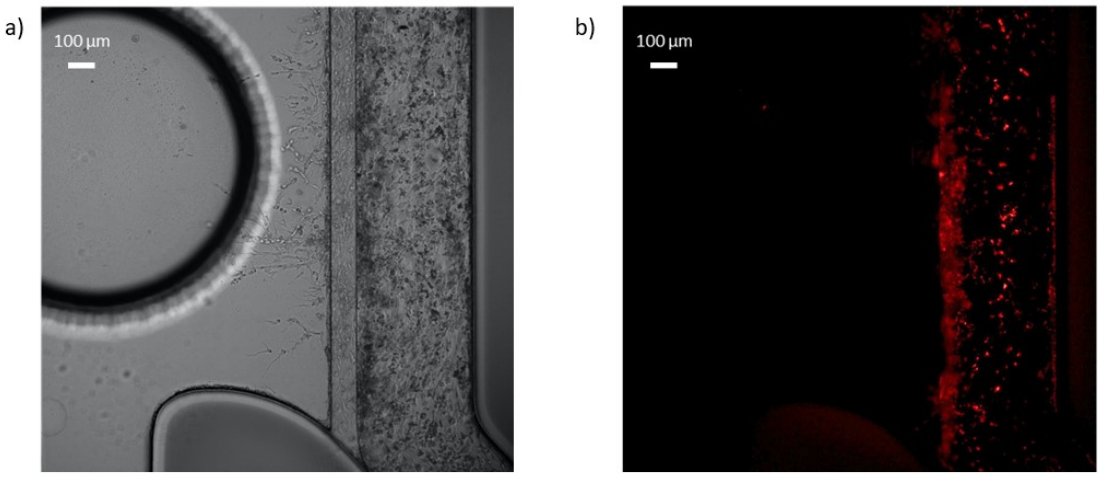


**Figure 2.30:** The figure collect the images acquired on the chip during the perfusion assay with Rhod-NPs. a) Bright-field image of the perfusion channel at 7 days after growth factor administration. b) Fluorescence image of the perfusion channel after Rhod-NPs administration (displayed in red).

These results confirm that the developed vasculature model replicates the low permeability of brain capillaries[69] and can be used to validate new alternative drug delivery methods aimed at overcoming this barrier, such as the cell-mediated transport described previously.

### 2.3.4 Spheroid integration in the vascular model

The successful formation and characterization of vessels within the MIMETAS OrganoPlate ® Graft demonstrates the potential of this tool for *in vitro* vascularization of human tissues.
Complete development of the microvascular network within the graft chamber requires at least 5 days of culture after growth factor administration. At the end of this period, spheroids that model GBM tumour tissue can be introduced inside the chamber. This study employed MTSs consisting of cocultures of differentiated GBM cells and GSCs in a 90:10 ratio. In the first trials, the spheroid was inserted directly into the chamber, following the protocol provided by the manufacturer. Figure 2.31 shows an overview of the entire chip 1 h after spheroid introduction. The insertion procedure adopted does not seem to alter the morphology of the spheroid and ensures precise positioning within the graft chamber.

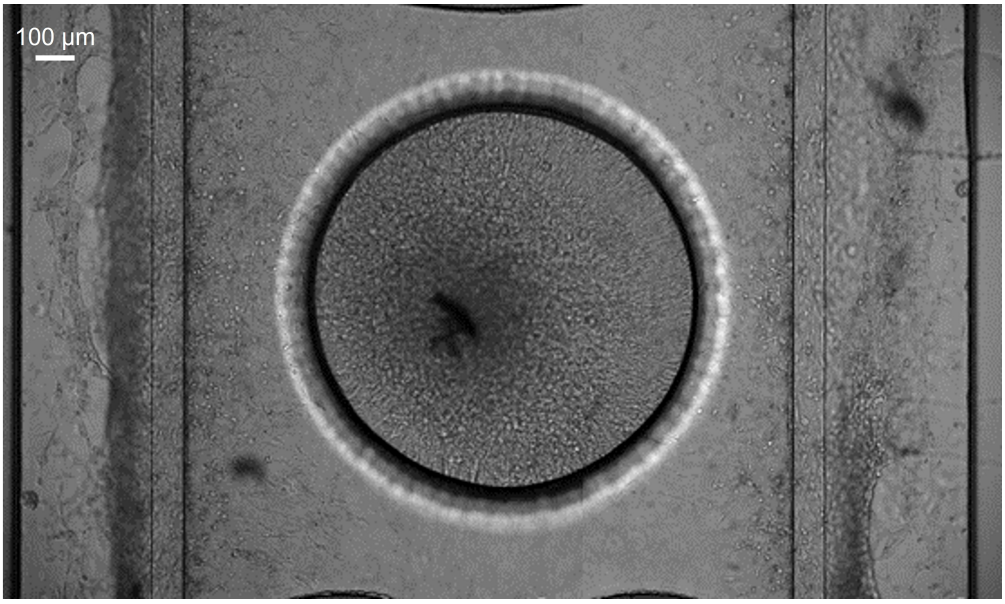


**Figure 2.31:** Overall bright-field view of the chip 1 h after spheroid insertion.

However, the collagen gel used to form the chamber and channels does not seem to guarantee the structural stability of the spheroid over time. As shown in Figure 2.32, only 24 hours after the placement of the spheroid in the chip, there is a total loss of the characteristic three-dimensional structure.

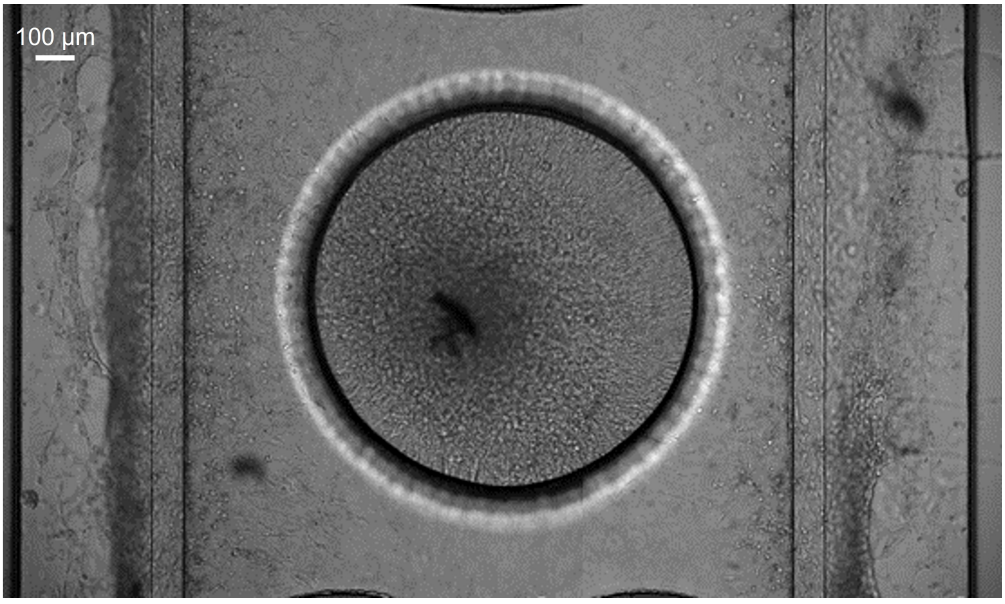


**Figure 2.32:** Overall bright-field view of the chip 24 h after spheroid insertion.

Spheroid disintegration is caused by the migration of differentiated tumour cells, which infiltrate the gel trying to adhere to it. In contrast, the aggregate of CSCs is preserved, confirming the predisposition of stem cells to remain confined in niche-like areas rather than spreading on the substrate[26].
To preserve the integrity of the three-dimensional structure, the spheroid was then encapsulated in the VitroGel® Hydrogel System during the placement phase. As shown by the data in section 2.2.6, this hydrogel prevents the disintegration of the spheroid for at least 72 h.
After one hour of incubation to stabilize the gel, the correct positioning of the spheroid can be verified (Figure 2.33a). Figure 2.33b also confirms that the new insertion protocol did not damage the pre-existing vascular network.

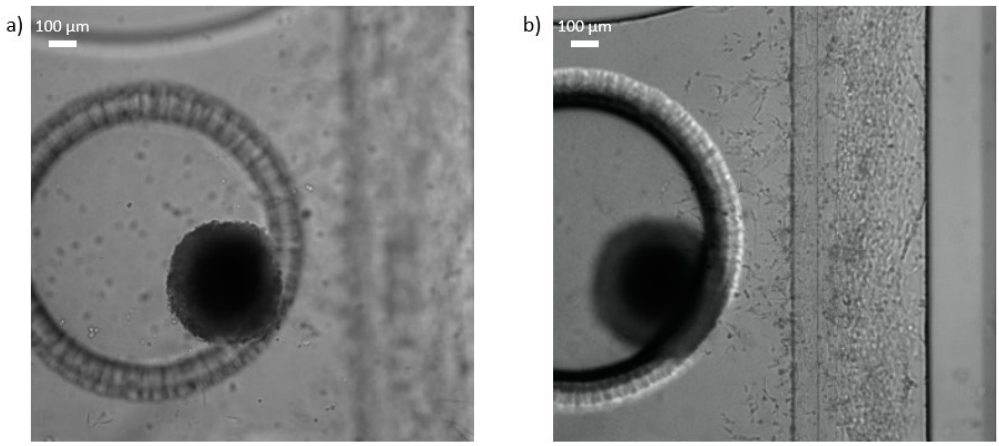


**Figure 2.33:** The bright-field images show the view of the chip 1 h after spheroid insertion within the VitroGel® Hydrogel System. a) Spheroid in the graft chamber. b) Microvascular network and perfusion channel.

Thanks to the support of the hydrogel, the spheroid retains its three-dimensional structure 24 hours after insertion into the chamber. However, Figure 2.34a shows that moderate invasion phenomena in the collagen gel remain due to the highly infiltrative nature of the tumour cells.
This infiltration could be avoided by adjusting the dilution ratios used to increase the stiffness of the gel. However, these changes could hinder the development of the vascular network through the spheroid. On the contrary, the presence of the VitroGel® Hydrogel formed with the current protocol does not limit the vascular progression towards the spheroid after 24 h (figure 2.34b). Furthermore, GBM cells also invade surrounding tissues (albeit on longer time scales) *in vivo* [3]. Hence, this behaviour could be useful for testing the influence of drugs on infiltration processes.

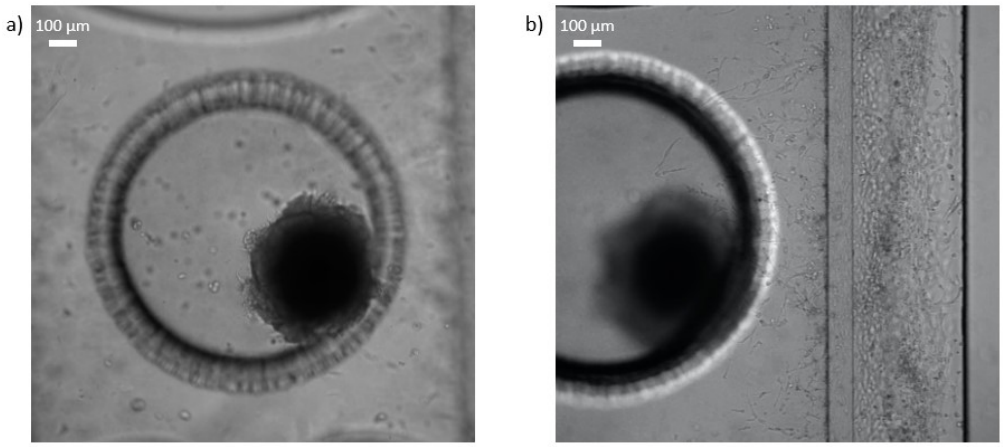


**Figure 2.34:** The bright-field images show the view of the chip 24 h after spheroid insertion within the VitroGel® Hydrogel System. a) Spheroid in the graft chamber. b) Microvascular network and perfusion channel.

# Chapter 3

# Conclusions

The results of this study show the potential of three-dimensional models as an evaluation tool to identify new treatment strategies against glioblastoma, particularly for nanoparticle- and cell-mediated drug delivery.
Spheroid-based models were developed to replicate the morphology and histology of this tumour using different populations (differentiated tumour cells, stem cells and immune cells) present in the GBM microenvironment. These models can be favourably employed in preliminary drug screening while also considering the effect of interactions between these components. Nevertheless, most of the chemotherapeutic agents validated by *in vitro* studies are not effective *in vivo* due to the presence of the blood-brain barrier. Therefore, lipid-coated polymeric carriers were produced by nanoprecipitation to encapsulate significant drug doses and ensure a sustained release. Viability assays on multicellular spheroids treated with bortezomib-NPs confirmed slightly lower treatment efficacy than the free drug (due to delayed-release).
However, as even nanostructures cannot pass through brain capillaries without appropriate surface modifications, microglial cells were investigated as bortezomib-loaded nanoparticles transporter. Our results show that, despite low nanoparticles uptake, cell-mediated treatment is effective on multicellular spheroid models. Furthermore, in vitro tests verified that microglia cells can spontaneously migrate through gels mimicking the extracellular matrix to infiltrate tumour spheroids. The evidence thus demonstrates how this delivery method, which is currently under-researched, is promising for overcoming the accumulation problems observed *in vivo*.
To further confirm the usefulness of microglia-mediated transport, the ability to extravasate through brain capillaries must be verified. Therefore, the spheroid-based model was combined with a commercial microfluidic device to form a biomimetic microvascular network. The use of native human brain capillary cells and optimised seeding and angiogenesis protocols allowed the artificial creation of vessels

that replicate the selective permeability observed in vivo. The successful spheroid vascularization and perfusion confirm that the device can be used as a more reliable GBM model This tool will be essential to study microglia cells extravasation and infiltration, as well as to verify the efficacy of cell-mediated drug transport and release.
The objective of these *in vitro* studies will be to systematically evaluate different hypotheses of cellular transporter-mediated treatment to overcome current limitations to drug accumulation in GBM. If the results of systemic drug delivery with microglia cells do not show promising results in the model, different treatment hypotheses, such as the use of circulating macrophages, may be evaluated. Alternatively, current results suggest that the same cells could be used in local delivery systems. Hence, nanoparticle-loaded microglia cells can be inserted at the resection margins during surgery or injected into the GBM mass to enhance drug accumulation and retention. However, all these hypotheses will have to be studied on the vascularized model, possibly enriched with additional components of the blood-brain barrier and brain tissue.

# Bibliography


[1] Hyuna Sung, Jacques Ferlay, Rebecca L Siegel, Mathieu Laversanne, Isabelle Soerjomataram, Ahmedin Jemal, and Freddie Bray. «Global cancer statistics 2020: GLOBOCAN estimates of incidence and mortality worldwide for 36 cancers in 185 countries». In: *CA: a cancer journal for clinicians* 71.3 (2021), pp. 209–249.

[2] Cintia Carla da Hora, Markus W Schweiger, Thomas Wurdinger, and Bakhos A Tannous. «Patient-derived glioma models: from patients to dish to animals». In: *Cells* 8.10 (2019), p. 1177.

[3] Antonio Omuro and Lisa M DeAngelis. «Glioblastoma and other malignant gliomas: a clinical review». In: *Jama* 310.17 (2013), pp. 1842–1850.

[4] Mitsutoshi Nakada, Daisuke Kita, Takuya Watanabe, Yutaka Hayashi, Lei Teng, Ilya V Pyko, and Jun-Ichiro Hamada. «Aberrant signaling pathways in glioma». In: *Cancers* 3.3 (2011), pp. 3242–3278.

[5] James L Fisher, Judith A Schwartzbaum, Margaret Wrensch, and Joseph L Wiemels. «Epidemiology of brain tumors». In: *Neurologic clinics* 25.4 (2007), pp. 867–890.

[6] Patrick Y Wen and Santosh Kesari. «Malignant gliomas in adults». In: *New England Journal of Medicine* 359.5 (2008), pp. 492–507.

[7] Ahmad Faleh Tamimi and Malik Juweid. «Epidemiology and outcome of glioblastoma». In: *Exon Publications* (2017), pp. 143–153.

[8] Henry Ruiz-Garcia, Keila Alvarado-Estrada, Paula Schiapparelli, Alfredo Quinones-Hinojosa, and Daniel M Trifiletti. «Engineering three-dimensional tumor models to study glioma cancer stem cells and tumor microenvironment». In: *Frontiers in Cellular Neuroscience* 14 (2020), p. 298.

[9] Carolina Parra-Cantu, Wanlu Li, Alfredo Quiñones-Hinojosa, and Yu Shrike Zhang. «3D bioprinting of glioblastoma models». In: *Journal of 3D printing in medicine* 4.2 (2020), pp. 113–125.

[10] Michail-Dimitrios Papaioannou, Kevin Sangster, Rifat Shahriar Sajid, Ugljesa Djuric, and Phedias Diamandis. «Cerebral organoids: emerging ex vivo humanoid models of glioblastoma». In: *Acta Neuropathologica Communications* 8.1 (2020), pp. 1–9.

[11] HJ Scherer. «Cerebral astrocytomas and their derivatives». In: *The American Journal of Cancer* 40.2 (1940), pp. 159–198.

[12] David N Louis et al. «The 2016 World Health Organization classification of tumors of the central nervous system: a summary». In: *Acta neuropathologica* 131.6 (2016), pp. 803–820.

[13] Hiroko Ohgaki and Paul Kleihues. «The definition of primary and secondary glioblastoma». In: *Clinical cancer research* 19.4 (2013), pp. 764–772.

[14] Kimmo J Hatanpaa, Sandeep Burma, Dawen Zhao, and Amyn A Habib. «Epidermal growth factor receptor in glioma: signal transduction, neuropathology, imaging, and radioresistance». In: *Neoplasia* 12.9 (2010), pp. 675–684.

[15] Dorota Jesionek-Kupnicka et al. «TP53 promoter methylation in primary glioblastoma: relationship with TP53 mRNA and protein expression and mutation status». In: *DNA and cell biology* 33.4 (2014), pp. 217–226.

[16] Roel GW Verhaak et al. «Integrated genomic analysis identifies clinically relevant subtypes of glioblastoma characterized by abnormalities in PDGFRA, IDH1, EGFR, and NF1». In: *Cancer cell* 17.1 (2010), pp. 98–110.

[17] M Adelita Vizcaíno, Smit Shah, Charles G Eberhart, and Fausto J Rodriguez. «Clinicopathologic implications of NF1 gene alterations in diffuse gliomas». In: *Human pathology* 46.9 (2015), pp. 1323–1330.

[18] Catarina Fernandes, Andreia Costa, Lígia Osório, Rita Costa Lago, Paulo Linhares, Bruno Carvalho, and Cláudia Caeiro. «Current standards of care in glioblastoma therapy». In: *Exon Publications* (2017), pp. 197–241.

[19] Kun-Wei Liu, Bo Hu, and Shi-Yuan Cheng. «Platelet-derived growth factor receptor alpha in glioma: a bad seed». In: *Chinese journal of cancer* 30.9 (2011), p. 590.

[20] Qianghu Wang et al. «Tumor evolution of glioma-intrinsic gene expression subtypes associates with immunological changes in the microenvironment». In: *Cancer cell* 32.1 (2017), pp. 42–56.

[21] Giuseppe Nicolò Fanelli, Dario Grassini, Valerio Ortenzi, Francesco Pasqualetti, Nicola Montemurro, Paolo Perrini, Antonio Giuseppe Naccarato, and Cristian Scatena. «Decipher the Glioblastoma Microenvironment: The First Milestone for New Groundbreaking Therapeutic Strategies». In: *Genes* 12.3 (2021), p. 445.

[22] Samer Nicolas, Sandra Abdellatef, Maria Al Haddad, Isabelle Fakhoury, and Mirvat El-Sibai. «Hypoxia and EGF stimulation regulate VEGF expression in human glioblastoma multiforme (GBM) cells by differential regulation of the PI3K/Rho-GTPase and MAPK pathways». In: *Cells* 8.11 (2019), p. 1397.

[23] Simone Frandsen, Helle Broholm, Vibeke Andrée Larsen, Kirsten Grunnet, Søren Møller, Hans Skovgaard Poulsen, and Signe Regner Michaelsen. «Clinical characteristics of gliosarcoma and outcomes from standardized treatment relative to conventional glioblastoma». In: *Frontiers in oncology* 9 (2019), p. 1425.

[24] Kaoru Ogawa, Akira Kurose, Akihisa Kamataki, Kenichiro Asano, Kosuke Katayama, and Hidekachi Kurotaki. «Giant cell glioblastoma is a distinctive subtype of glioma characterized by vulnerability to DNA damage». In: *Brain tumor pathology* 37.1 (2020), pp. 5–13.

[25] Suxia Wang, Qiaowei He, Qianqian Zhang, Bingxin Guan, and Xiuzhi Zhou. «Clinicopathologic features and prognosis of epithelioid glioblastoma». In: *International Journal of Clinical and Experimental Pathology* 13.7 (2020), p. 1529.

[26] Dolores Hambardzumyan and Gabriele Bergers. «Glioblastoma: defining tumor niches». In: *Trends in cancer* 1.4 (2015), pp. 252–265.

[27] Sheng Tu et al. «Crosstalk Between Tumor-Associated Microglia/Macrophages and CD8-Positive T Cells Plays a Key Role in Glioblastoma». In: *Frontiers in Immunology* (2021), p. 2670.

[28] Marie Blanchette and Richard Daneman. «Formation and maintenance of the BBB». In: *Mechanisms of development* 138 (2015), pp. 8–16.

[29] Basant Salah Mahmoud, Ali Hamod AlAmri, and Christopher McConville. «Polymeric nanoparticles for the treatment of malignant gliomas». In: *Cancers* 12.1 (2020), p. 175.

[30] Claudia Scaringi, Linda Agolli, and Giuseppe Minniti. «Technical advances in radiation therapy for brain tumors». In: *Anticancer research* 38.11 (2018), pp. 6041–6045.

[31] Roger Stupp et al. «Radiotherapy plus concomitant and adjuvant temozolomide for glioblastoma». In: *New England journal of medicine* 352.10 (2005), pp. 987–996.

[32] Michael G Hart, Ruth Garside, Gabriel Rogers, Ken Stein, and Robin Grant. «Temozolomide for high grade glioma». In: *Cochrane Database of Systematic Reviews* 4 (2013).

[33] Jeremy N Rich et al. «Phase II trial of gefitinib in recurrent glioblastoma». In: *Journal of Clinical Oncology* 22.1 (2004), pp. 133–142.

[34] Tracy T Batchelor et al. «Phase III randomized trial comparing the efficacy of cediranib as monotherapy, and in combination with lomustine, versus lomustine alone in patients with recurrent glioblastoma». In: *Journal of Clinical Oncology* 31.26 (2013), p. 3212.

[35] Patrick Y Wen et al. «Phase I/II study of imatinib mesylate for recurrent malignant gliomas: North American Brain Tumor Consortium Study 99-08». In: *Clinical Cancer Research* 12.16 (2006), pp. 4899–4907.

[36] Wei Yu, Lili Zhang, Qichun Wei, and Anwen Shao. «O6-methylguanine-DNA methyltransferase (MGMT): challenges and new opportunities in glioma chemotherapy». In: *Frontiers in oncology* 9 (2020), p. 1547.

[37] Patrick Roth, Warren P Mason, Paul G Richardson, and Michael Weller. «Proteasome inhibition for the treatment of glioblastoma». In: *Expert Opinion on Investigational Drugs* 29.10 (2020), pp. 1133–1141.

[38] Jun-Hai Tang et al. «Bortezomib inhibits growth and sensitizes glioma to temozolomide (TMZ) via down-regulating the FOXM1–Survivin axis». In: *Cancer Communications* 39.1 (2019), pp. 1–16.

[39] Sonali K Doke and Shashikant C Dhawale. «Alternatives to animal testing: A review». In: *Saudi Pharmaceutical Journal* 23.3 (2015), pp. 223–229.

[40] Michaela Kroeger. «How omics technologies can contribute to the '3R'principles by introducing new strategies in animal testing». In: *TRENDS in Biotechnology* 24.8 (2006), pp. 343–346.

[41] Tijana Stanković, Teodora Ranđelović, Miodrag Dragoj, Sonja Stojković Burić, Luis Fernández, Ignacio Ochoa, Victor M Pérez-García, and Milica Pešić. «In vitro biomimetic models for glioblastoma-a promising tool for drug response studies». In: *Drug Resistance Updates* 55 (2021), p. 100753.

[42] Sigrid A Langhans. «Three-dimensional in vitro cell culture models in drug discovery and drug repositioning». In: *Frontiers in pharmacology* 9 (2018), p. 6.

[43] Thomas Hartung. «Thoughts on limitations of animal models». In: *Parkinsonism & related disorders* 14 (2008), S81–S83.

[44] Noriyuki Kijima and Yonehiro Kanemura. «Mouse models of glioblastoma». In: *Exon Publications* (2017), pp. 131–139.

[45] Joris Guyon, Laëtitia Andrique, Nadège Pujol, Gro Vatne Røsland, Gaëlle Recher, Andreas Bikfalvi, and Thomas Daubon. «A 3D spheroid model for glioblastoma». In: *Journal of visualized experiments: JoVE* 158 (2020).

[46] Giulia Silvani, Carin Basirun, Hanjie Wu, Christine Mehner, Kate Poole, Peta Bradbury, and Joshua Chou. «A 3D-Bioprinted Vascularized Glioblastoma-on-a-Chip for Studying the Impact of Simulated Microgravity as a Novel Pre-Clinical Approach in Brain Tumor Therapy». In: *Advanced Therapeutics* (2021), p. 2100106.

[47] Fadi Jacob et al. «A patient-derived glioblastoma organoid model and biobank recapitulates inter-and intra-tumoral heterogeneity». In: *Cell* 180.1 (2020), pp. 188–204.

[48] Yang Xiao et al. «Ex vivo dynamics of human glioblastoma cells in a microvasculature-on-a-chip system correlates with tumor heterogeneity and subtypes». In: *Advanced Science* 6.8 (2019), p. 1801531.

[49] Brent A Reynolds and Samuel Weiss. «Generation of neurons and astrocytes from isolated cells of the adult mammalian central nervous system». In: *science* 255.5052 (1992), pp. 1707–1710.

[50] Roberta Azzarelli. «Organoid models of glioblastoma to study brain tumor stem cells». In: *Frontiers in cell and developmental biology* 8 (2020), p. 220.

[51] X Cui, Y Hartanto, and H Zhang. «Advances in multicellular spheroids formation». In: *Journal of the Royal Society Interface* 14.127 (2017), p. 20160877.

[52] Zarema Gilazieva, Aleksei Ponomarev, Catrin Rutland, Albert Rizvanov, and Valeriya Solovyeva. «Promising applications of tumor spheroids and organoids for personalized medicine». In: *Cancers* 12.10 (2020), p. 2727.

[53] Khashayar Moshksayan, Navid Kashaninejad, Majid Ebrahimi Warkiani, John G Lock, Hajar Moghadas, Bahar Firoozabadi, Mohammad Said Saidi, and Nam-Trung Nguyen. «Spheroids-on-a-chip: Recent advances and design considerations in microfluidic platforms for spheroid formation and culture». In: *Sensors and Actuators B: Chemical* 263 (2018), pp. 151–176.

[54] Agavi Stavropoulou Tatla, Alexander W Justin Colin Watts Athina, E Markaki, A Stavropoulou Tatla, AW Justin, AE Markaki, and C Watts. «A Vascularized Tumoroid Model for Human Glioblastoma Angiogenesis». In: *Scientific Reports* 11 (2021), p. 19550.

[55] Madeline A Lancaster and Juergen A Knoblich. «Generation of cerebral organoids from human pluripotent stem cells». In: *Nature protocols* 9.10 (2014), pp. 2329–2340.

[56] Shan Bian, Marko Repic, Zhenming Guo, Anoop Kavirayani, Thomas Burkard, Joshua A Bagley, Christian Krauditsch, and Jürgen A Knoblich. «Genetically engineered cerebral organoids model brain tumor formation». In: *Nature methods* 15 (2018), pp. 631–639.

[57] Christopher G Hubert et al. «A three-dimensional organoid culture system derived from human glioblastomas recapitulates the hypoxic gradients and cancer stem cell heterogeneity of tumors found in vivo». In: *Cancer research* 76.8 (2016), pp. 2465–2477.

[58] Amanda Linkous et al. «Modeling patient-derived glioblastoma with cerebral organoids». In: *Cell reports* 26.12 (2019), pp. 3203–3211.

[59] Yantao Fan, Duong Thanh Nguyen, Yasemin Akay, Feng Xu, and Metin Akay. «Engineering a brain cancer chip for high-throughput drug screening». In: *Scientific reports* 6.1 (2016), pp. 1–12.

[60] Xingliang Dai, Cheng Ma, Qing Lan, and Tao Xu. «3D bioprinted glioma stem cells for brain tumor model and applications of drug susceptibility». In: *Biofabrication* 8.4 (2016), p. 045005.

[61] Miguel A Hermida et al. «Three dimensional in vitro models of cancer: Bioprinting multilineage glioblastoma models». In: *Advances in biological regulation* 75 (2020), p. 100658.

[62] Marcel Alexander Heinrich, Ruchi Bansal, Twan Lammers, Yu Shrike Zhang, Raymond Michel Schiffelers, and Jai Prakash. «3D-bioprinted mini-brain: a glioblastoma model to study cellular interactions and therapeutics». In: *Advanced materials* 31.14 (2019), p. 1806590.

[63] Petra Huehnchen et al. «Bortezomib at therapeutic doses poorly passes the blood–brain barrier and does not impair cognition». In: *Brain communications* 2.1 (2020), fcaa021.

[64] Elvin Blanco, Haifa Shen, and Mauro Ferrari. «Principles of nanoparticle design for overcoming biological barriers to drug delivery». In: *Nature biotechnology* 33.9 (2015), pp. 941–951.

[65] Jingyan Li and Cristina Sabliov. «PLA/PLGA nanoparticles for delivery of drugs across the blood-brain barrier». In: *Nanotechnology Reviews* 2.3 (2013), pp. 241–257.

[66] Clara Mattu et al. «Alternating block copolymer-based nanoparticles as tools to modulate the loading of multiple chemotherapeutics and imaging probes». In: *Acta biomaterialia* 80 (2018), pp. 341–351.

[67] Wayne S Rasband. «ImageJ, U. S. National Institutes of Health, Bethesda, Maryland, USA». In: *http://imagej. nih. gov/ij/* (2018).

[68] Zar Chi Soe et al. «Folate-targeted nanostructured chitosan/chondroitin sulfate complex carriers for enhanced delivery of bortezomib to colorectal cancer cells». In: *Asian journal of pharmaceutical sciences* 14.1 (2019), pp. 40–51.

[69] Malka Shilo, Anat Sharon, Koby Baranes, Menachem Motiei, Jean-Paul M Lellouche, and Rachela Popovtzer. «The effect of nanoparticle size on the probability to cross the blood-brain barrier: an in-vitro endothelial cell model». In: *Journal of nanobiotechnology* 13.1 (2015), pp. 1–7.

[70] Junpeng Nie et al. «Co-delivery of docetaxel and bortezomib based on a targeting nanoplatform for enhancing cancer chemotherapy effects». In: *Drug delivery* 24.1 (2017), pp. 1124–1138.

[71] Isabelle Pochard, Jean-Philippe Boisvert, Jacques Persello, and Alain Foissy. «Surface charge, effective charge and dispersion/aggregation properties of nanoparticles». In: *Polymer international* 52.4 (2003), pp. 619–624.

[72] Shahed Behzadi et al. «Cellular uptake of nanoparticles: journey inside the cell». In: *Chemical Society Reviews* 46.14 (2017), pp. 4218–4244.

[73] J Zuidema, B Van Minnen, MM Span, CE Hissink, TG Van Kooten, and RRM Bos. «In vitro degradation of a biodegradable polyurethane foam, based on 1, 4-butanediisocyanate: A three-year study at physiological and elevated temperature». In: *Journal of Biomedical Materials Research Part A: An Official Journal of The Society for Biomaterials, The Japanese Society for Biomaterials, and The Australian Society for Biomaterials and the Korean Society for Biomaterials* 90.3 (2009), pp. 920–930.

[74] Yang Zhou et al. «Development of Bortezomib-Loaded Nanoparticles for Locoregional Treatment of Hepatocellular Carcinoma». PhD thesis. Johns Hopkins University, 2020.

[75] Zhihong Chen et al. «Cellular and molecular identity of tumor-associated macrophages in glioblastoma». In: *Cancer research* 77.9 (2017), pp. 2266–2278.

[76] Carlotta Mattioda. *Three-dimensional glioblastoma multiforme model for in vitro nanomedicine testing*. Master Thesis, Politecnico di Torino. 2021.

[77] Caleb R Robinson, Hongmei Zhang, and Patrick M Dougherty. «Astrocytes, but not microglia, are activated in oxaliplatin and bortezomib-induced peripheral neuropathy in the rat». In: *Neuroscience* 274 (2014), pp. 308–317.

[78] Lisa Oliver, Lisenn Lalier, Céline Salaud, Dominique Heymann, Pierre François Cartron, and François Vallette. «Drug resistance in glioblastoma: are persisters the key to therapy?» In: *Cancer Drug Resistance* 3 (2020), Online–ahead.

[79] Zhiyun Wei, Shubham Kale, Rachid El Fatimy, Rosalia Rabinovsky, and Anna M Krichevsky. «Co-cultures of glioma stem cells and primary neurons, astrocytes, microglia, and endothelial cells for investigation of intercellular communication in the brain». In: *Frontiers in neuroscience* 13 (2019), p. 361.

[80] Hailong Liu et al. «Pro-inflammatory and proliferative microglia drive progression of glioblastoma». In: *Cell Reports* 36.11 (2021), p. 109718.

[81] Jason V Gregory, Padma Kadiyala, Robert Doherty, Melissa Cadena, Samer Habeel, Erkki Ruoslahti, Pedro R Lowenstein, Maria G Castro, and Joerg Lahann. «Systemic brain tumor delivery of synthetic protein nanoparticles for glioblastoma therapy». In: *Nature communications* 11.1 (2020), pp. 1–15.

[82] Yitian Du, Zhenzhen Yang, Qi Sun, Meng Lin, Rudong Wang, Yiwei Peng, Xinyi Chen, and Xianrong Qi. «Engineered Microglia Potentiate the Action of Drugs against Glioma Through Extracellular Vesicles and Tunneling Nanotubes». In: *Advanced Healthcare Materials* 10.9 (2021), p. 2002200.

[83] Hongliang Xin, Xianyi Sha, Xinyi Jiang, Wei Zhang, Liangcen Chen, and Xiaoling Fang. «Anti-glioblastoma efficacy and safety of paclitaxel-loading Angiopep-conjugated dual targeting PEG-PCL nanoparticles». In: *Biomaterials* 33.32 (2012), pp. 8167–8176.

[84] Nana-Fatima Haruna, Bhavya Shah, and John Huang. «Long Term 3D Tumor Spheroid Culture in VitroGel Hydrogel Matrix». In: ().

[85] Li Liu and Guo-Ping Shi. «CD31: beyond a marker for endothelial cells». In: *Cardiovasc Res.* 94.1 (2012), pp. 3–5.

[86] Hans-Christian Bauer, Andreas Traweger, and Hannelore Bauer. «Proteins of the tight junction in the blood-brain barrier». In: *Blood-spinal cord and brain barriers in health and disease*. Elsevier, 2004, pp. 1–10.

[87] Reka Natarajan, Nicole Northrop, and Bryan Yamamoto. «Fluorescein Isothiocyanate (FITC)-Dextran Extravasation as a Measure of Blood-Brain Barrier Permeability». In: *Current protocols in neuroscience* 79.1 (2017), pp. 9–58.